Modeling the longevity and secretory capacity of engineered human plasma cells

Rene Yu-Hong Cheng

A dissertation

submitted in partial fulfillment of the

requirements for the degree of

Doctor of Philosophy

University of Washington

2022

Reading Committee:

Richard G. James, Chair

David J. Rawlings

Hao-Yuan Kueh

Shaun W. Jackson

Program Authorized to Offer Degree:

Molecular Engineering & Sciences Institute

University of Washington

Abstract

Modeling the longevity and secretory capacity of engineered human plasma cells

Rene Yu-Hong Cheng

Chair of the Supervisory Committee:

Richard G. James

Molecular Engineering & Sciences Institute

Due to their unique longevity and capacity to secrete high levels of protein, plasma cells have the potential to be used as a cell therapy for protein replacement. Through CITE-seq and bulk RNA-seq experiments, I showed *ex vivo* engineered human plasma cells exhibited transcriptional features akin to natural long-lived plasma cells. These engineered cells exhibited altered protein secretion and long-term *in vivo* engraftment in a humanized IL-6 mouse model. To further study the protein secretion capacity of our engineered plasma cells, we developed a method to associate protein secretion with cell information in a single-cell basis. We were able to analyze thousands of plasma cells directly linking IgG secretion with transcript profile (SEC-seq) and surface markers. Our work has added to our understanding of *ex vivo* engineered plasma cells and the technology we developed enables exploration of links between genome and secretory function, laying the foundation for numerous discoveries in immunology, stem cell biology, and beyond.

TABLE OF CONTENTS

List of Figures

LIST OF TABLES

ACKNOWLEDGEMENTS

In summer of 2018, it was the first time I stepped into Seattle Children Research Institute. The building is downtown and so much fancier than the labs I've been to, I felt like a hillbilly, just wow at everything. And this is where I started my B cell engineering journey in James' lab.

First, I would like to thank my boss, Dr. Richard James. He's not a conventional advisor but maybe I am not a conventional graduate student either, so his mentorship worked great for me. Starting with zero immunology background, he guided me in designing experiments and discussing the data in detail with me. I deeply appreciated that most of my science training was taught hands on by Rich. I am grateful Rich was always available to talk about science any time I stopped by his office. We had countless conversations brainstorming and talking about random ideas. Those chats always kept me motivated. Failed experiments are the most challenging thing in a Ph.D.. Dealing with that frustration is not easy. I appreciate that Rich was always understanding: "This is not the end of the world.", "We still learned something from this." He would sit down with me to troubleshoot and find someone experienced to help me. I gained a lot of analytical skills and confidence and Rich played the main role in this "positive feedback" loop. Without his encouragement and sometimes throw griefs to each other ("shitquilibrium", his made up word), I wouldn't know my gifts or shortcomings to make me who I am today. I am very lucky to be his first graduate student, he was my advisor but also a friend that supports me and puts up with me.

I would like to thank Dr. David Rawlings. He was at the top of my list when I was looking for a lab. I feel so fortunate to have had David's mentorship in the past four years. There are two idioms in Chinese, "words like gems (zì zì zhū jī)" and "like spring breeze (rú mù chūn

fēng)", which describe how I feel when David talks and his scholarly vibe. David always asked me the key questions. These helped me think about what's behind the data. He would know the important pieces of data for the question we were asking, and what I was still missing. He just knows everything! I am grateful and feel luxurious to have him as my mentor.

I would also like to thank my thesis advisory committee members Dr. Hao Yuan Kueh, Dr. Shaun Jackson. Thank you for giving all the advice for my thesis work, it is important to have different perspectives. Also, thank you for pointing out the areas that I need to work on more. I truly appreciate all the help.

Thank you to Dr. Dino Di Carlo and Dr. Joe de Rutte. I am always amazed how passionate and involved they are about our corporate project. I really appreciate that we had the opportunity to work together.

Thank you to Dr. Hong Qian and Dr. Ying-Jen Yang. I've learned so much and been inspired by Hong Qian's and Ying-Jen's lectures.

James' lab is like my second home, it's a place where I go joyously every day. So many of the people there were instrumental to my success.

First, I want to specifically thank Emma Suchland. She was my lab teacher when I first joined the lab. She's so competent at what she does and taught me all the lab techniques and tricks. Emma and Iana Meitlis were like angels and goddesses to me. They made me feel welcome when I first joined the lab knowing nothing and being insecure. I still remember vividly they took me to get a free Slurpee at 7-11 in the first month I rotated in the lab. Emma was also our lab manager, she made everything neat and in order, so I could do my research without worrying about all the other logistics. I can't imagine my lab life without her.

Second, I want to thank Andee Ott. She was my life teacher as well as my English teacher. She taught me American culture, idioms, and filters. When we worked together, she was like a Xanax pill, always a calming influence. Thanks to her for making AAV and helping in most of my mouse experiments.

More thanks to the amazing scientists, Tingting Zhang, Nikita Trivedi, Kelsey Roe and Yuchi Honaker. They were my go-to people when I wanted to discuss science and sometimes life. They are super intelligent, always feeling inspired and ecstasy talking to them. I'm so honored to have them as my mentors.

Thanks to Nathan Camp. He's like a lab dad, yelling at us, disciplining us graduate students. Lab had so much more joy and laughter when he was around.

More thanks to Cade Ito, Ragan Pitner, and Tyler Hill. They are brilliant scientists and my lab buddies, often unreserved giving me suggestions and supporting each other. Especially thanks to Cade, he has the cutest dog (Cooper) ever. Cooper offers the sweetest pet therapy. Also thanks to Dr. Alice Chau who offered me an air-conditioned bed to sleep in when the heat wave hit Seattle.

I would also like to thank all other James' lab members for being part of my graduate school life. Seriously, I have had the happiest time here in my whole life.

Family is so important to me, but I realized how important it is until I study abroad far from home. Thanks to the great greatest woman, my mom, as a single mom she raised me and my brother up by herself, and never surrendered no matter how hard life was on her. Everytime I felt frustrated, I thought about the 100 times she conquered something far more, and I felt brave again.

Thanks to my families here, Huiyun (Sunsun), Gloria, Hao, and Jimmy. They are such genuine people, and they have different wisdom that I admire. Especially thanks to Sunsun who offered me lots of academic support. Lastly, thanks for my loving partner, Tyler. He's the man who accompanies me through all the ups and downs. He always gives me the warmest hugs and smiles to send me off to the lab, so I get enough oxytocin every morning. Feel Seattle has become my second home and become the most beautiful city because of them. I am deeply grateful.

Chapter 1.

INTRODUCTION AND BACKGROUND

1.1. *EX VIVO* GENERATED PLASMA CELLS AND PLASMA CELL THERAPY

Biologic protein drugs are in use for treatment of most classes of human disease including cancer, autoimmunity and protein deficiencies [1]. A major challenge in the development of non-antibody biologics is poor pharmacokinetics and short half-life. Conjugation of biologics with carrier devices such as PEG [2], Fc domains [3], albumin [4] or nanoparticles [5] can increase half-life, but these drugs still require recurrent delivery. An alternative method to conjugation is to express and deliver protein drugs using a long-lived cell source. One possible source is human long-lived plasma cells (PCs), a terminally differentiated B cell population that resides in the bone marrow (BM) for decades [6,7], and stably produces high concentrations of antibodies [8]. There are efforts pursuing several strategies to re-purpose B cells or PCs as a drug-secreting cell therapy for the treatment of disease [9–16]. The Voss [16] and Barzel [14] laboratories delivered engineered memory-like antigen specific B cells to mice and used immunization to direct *in vivo* differentiation to PCs [16]. After 3 rounds of immunization, antigen-specific PCs were quantifiable in BM using sequencing up to 250 days following B cell delivery. Alternatively, the Taylor lab [15] showed that *in vitro* differentiated engineered antigen-specific PCs were detectable *in vivo* up to 87 days following cell transfer.

1.2. PLASMA CELL WITH CURRENT SINGLE CELL PROTEIN SECRETION ASSAY AND LIMITATION

Therapeutic protein once being edited in plasma cells and transferred in vivo, the dynamic of protein is crucial to cure the disease, and the methods to improve the protein secretion per cell also not well developed. The dynamic of protein is based on cell number dynamic, protein

secretion rate and degradation rate. For our current knowledge, plasma cells are a heterogeneous population (Fig. 1.3.1). Here, we assume there're *i* kind of plasma cells with different secretion ability to describe the cell number dynamics and protein number dynamics.

$$\frac{dN_i}{dt} = \beta_i N_i \tag{1.1}$$

$$\frac{dP_i}{dt} = \gamma_i N_i(t) - \lambda P_i = N_{0i} e^{-\beta_i t} - \lambda P_i \tag{1.2}$$

$$\frac{dN}{dt} = \sum_i \beta_i N_i = \sum_i \frac{dN_i}{dt} \tag{1.3}$$

The solution of eq.1.3, the cell number at a given time (*t*) is

$$N(t) = \sum_i N_i(t) = \sum_i N_{0i}\, e^{-\beta_i t} \tag{1.4}$$

$$\frac{dP}{dt} = \sum_i \gamma_i N_i(t) - \lambda P = \sum_i \gamma_i N_{0i} e^{-\beta_i t} - \lambda P \tag{1.5}$$

where N_i is the cell number of type *i* cell, N_{i0} is the initial cell number of type *i*, and β_i is the cell decay rate of type *i*. The γ_i is the protein secretion rate of type *i* and λ is the protein degradation rate. Equation 1.3-1.5 are describing the bulk dynamics. Here, the protein degradation is not based on the secretor and is hard to alter *in vivo*. The single cell protein secretion rate γ_i becomes one of the most important measurements while we are developing plasma cell therapy. Most importantly, associating molecular signature or cell marker to the protein secretion rate will maximize our goal to produce sustain and high amount of protein.

Standard single-cell analysis tools cannot simultaneously quantify external cellular information (e.g., secreted proteins) with cell surface and/or intracellular information. One possible method to infer information about secretions is to analyze the intracellular concentration of the transcripts (single cell transcriptomes) or proteins (flow cytometry) that potentially will be secreted. While transcripts associated with secreted proteins may sometimes correlate to secretion[17–19], transcript levels cannot adequately account for several post-transcriptional activities

such as RNA splicing, translation, post-translational modifications, enzymatic cleavage, or even storage of secreted proteins in secretory vesicles prior to secretion. Furthermore, intracellular proteins, including secreted proteins, can be analyzed, e.g., using intracellular cytokine staining, but through a destructive process that involves permeabilization and fixation of the cell. Forming pores in the cell is necessary for fluorescently-labeled antibodies to penetrate the intracellular space and bind to chemically fixed proteins. Downsides of permeabilization and fixation include the loss of cell viability and destruction of other intracellular molecules, such as mRNA, which limits downstream transcriptomic analysis. Finally, the presence of secreted proteins on or within the cell does not necessarily indicate that these proteins would have been secreted.

Other tools to characterize cell-secreted products lack the quantitative resolution, throughput, and multiplexing of flow cytometry and do not directly link secretions to transcriptomic information. Researchers have utilized optofluidic pens or other microfluidic compartments to isolate single cells and accumulate secreted products for analysis on solid surfaces near the cells. Two recent instruments that employ these approaches are the Beacon system from Berkeley Lights, and Isoplexis' Isolight system. Both systems use microscopic imaging to analyze the secreted products from cells, with dynamic range and the number of color channels constrained by the cameras and filter sets used[20–22]. In contrast, the gold standard in single-cell analysis, flow cytometers, leverage laser-based excitation and PMT-based detection to achieve sensitive multiplexed measurements with high dynamic range. Surface markers are not readily accessible in the Isolight system, while the Beacon system can analyze a few. The number of cells that can be analyzed depends on the number of optofluidic pens or microchambers on a single chip, usually between 1,000 to 10,000. While the Beacon system can sort cells after analysis, this is not achievable with the Isolight system. Another assay format that

is compatible with flow cytometry uses the cell's surface itself to capture secreted products (e.g., the cytokine-catch assay from Miltenyi). This assay format requires specialized bi-specific antibodies that bind to CD45 on leukocytes and capture specific cytokines but is not easily extensible to other secreted products or cells that lack consistent or high levels of CD45, including plasma B cells. Secretions can also diffuse away and bind to neighboring cells, leading to crosstalk since cells are not confined in individual compartments[23].

No current technology has been able to link the amount and type of secreted molecules from a single cell with its transcriptional profile, nor has this type of association been multiplexed at a scale of hundreds to thousands of single cells simultaneously. Developing a method that could explore the links between genome and secretory function could allow us to engineer secretory function and optimize the plasma cell therapy.

1.3. FIGURES

1.3.1. *ELISPOT spot analysis and IgG Plasma cells secretion heterogeneity.*

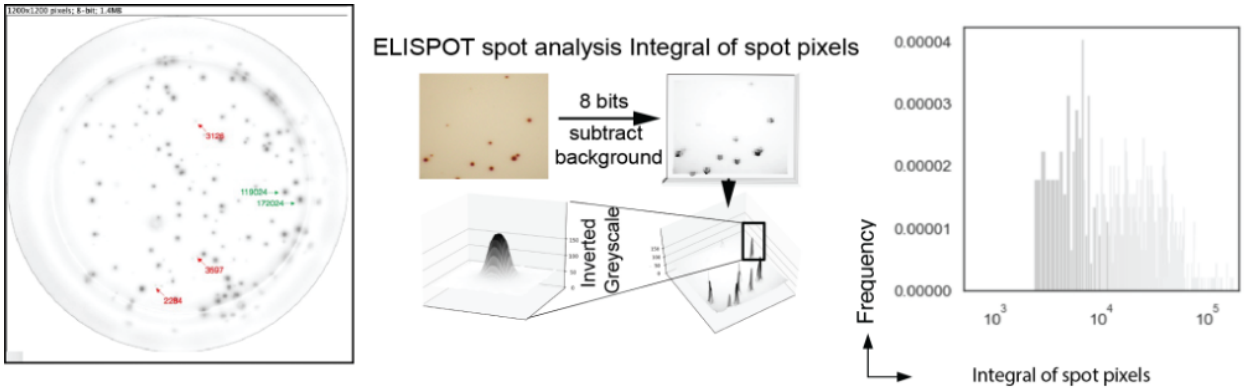

An ELISPOT image (left) showing IgG secretion for plasma cells following our differentiation protocol. Red arrows point to events with low IgG secretion (small faint spots) and green arrows point to events with higher IgG secretion (larger, more intense spots). The spot intensity is integrated over the entire spot area using ImageJ and the output histogram (right) represents the heterogeneous IgG secretion ability of the population.

1.4. BIBLIOGRAPHY

1. Lagassé, H. A. D. *et al.* Recent advances in (therapeutic protein) drug development. *F1000Res.* **6**, 113 (2017).

2. Veronese, F. M. & Mero, A. The impact of PEGylation on biological therapies. *BioDrugs* **22**, 315–329 (2008).

3. Czajkowsky, D. M., Hu, J., Shao, Z. & Pleass, R. J. Fc-fusion proteins: new developments and future perspectives. *EMBO Mol. Med.* **4**, 1015–1028 (2012).

4. Smith, B. J. *et al.* Prolonged in vivo residence times of antibody fragments associated with albumin. *Bioconjug. Chem.* **12**, 750–756 (2001).

5. Damgé, C., Maincent, P. & Ubrich, N. Oral delivery of insulin associated to polymeric nanoparticles in diabetic rats. *J. Control. Release* **117**, 163–170 (2007).

6. Halliley, J. L. *et al.* Long-Lived Plasma Cells Are Contained within the CD19(-)CD38(hi)CD138(+) Subset in Human Bone Marrow. *Immunity* **43**, 132–145 (2015).

7. Chu, V. T. & Berek, C. The establishment of the plasma cell survival niche in the bone marrow. *Immunol. Rev.* **251**, 177–188 (2013).

8. Nutt, S. L., Hodgkin, P. D., Tarlinton, D. M. & Corcoran, L. M. The generation of antibody-secreting plasma cells. *Nat. Rev. Immunol.* **15**, 160–171 (2015).

9. Hung, K. L. *et al.* Engineering Protein-Secreting Plasma Cells by Homology-Directed Repair in Primary Human B Cells. *Mol. Ther.* **26**, 456–467 (2018).

10. Voss, J. E. *et al.* Reprogramming the antigen specificity of B cells using genome-editing technologies. *Elife* **8**, (2019).

11. Johnson, M. J., Laoharawee, K., Lahr, W. S., Webber, B. R. & Moriarity, B. S. Engineering of Primary Human B cells with CRISPR/Cas9 Targeted Nuclease. *Sci. Rep.* **8**, 12144 (2018).

12. Hartweger, H. *et al.* HIV-specific humoral immune responses by CRISPR/Cas9-edited B cells. *J. Exp. Med.* **216**, 1301–1310 (2019).

13.Greiner, V. *et al.* CRISPR-Mediated Editing of the B Cell Receptor in Primary Human B Cells. *iScience* **12**, 369–378 (2019).

14.Nahmad, A. D. *et al.* Engineered B cells expressing an anti-HIV antibody enable memory retention, isotype switching and clonal expansion. *Nat. Commun.* **11**, 5851 (2020).

15.Moffett, H. F. *et al.* B cells engineered to express pathogen-specific antibodies protect against infection. *Sci Immunol* **4**, (2019).

16.Huang, D. *et al.* Vaccine elicitation of HIV broadly neutralizing antibodies from engineered B cells. *Nat. Commun.* **11**, 5850 (2020).

17.Vogel, C. & Marcotte, E. M. Insights into the regulation of protein abundance from proteomic and transcriptomic analyses. *Nat. Rev. Genet.* **13**, 227–232 (2012).

18.Liu, Y., Beyer, A. & Aebersold, R. On the Dependency of Cellular Protein Levels on mRNA Abundance. *Cell* **165**, 535–550 (2016).

19.Peterson, V. M. *et al.* Multiplexed quantification of proteins and transcripts in single cells. *Nat. Biotechnol.* **35**, 936–939 (2017).

20.Winters, A. *et al.* Rapid single B cell antibody discovery using nanopens and structured light. *MAbs* **11**, 1025–1035 (2019).

21.Liu, D., Paczkowski, P., Mackay, S., Ng, C. & Zhou, J. Single-Cell Multiplexed Proteomics on the IsoLight Resolves Cellular Functional Heterogeneity to Reveal Clinical Responses of Cancer Patients to Immunotherapies. *Methods Mol. Biol.* **2055**, 413–431 (2020).

22.Miwa, H., Dimatteo, R., de Rutte, J., Ghosh, R. & Di Carlo, D. Single-cell sorting based on secreted products for functionally defined cell therapies. *Microsyst Nanoeng* **8**, 84 (2022).

23.Dimatteo, R. & Di Carlo, D. IL-2 secretion-based sorting of single T cells using high-throughput microfluidic on-cell cytokine capture. *Lab Chip* **22**, 1576–1583 (2022).

Chapter 2.

EX VIVO ENGINEERED HUMAN PLASMA CELLS EXHIBIT ROBUST PROTEIN SECRETION AND LONG-TERM ENGRAFTMENT *IN VIVO*

This work has been published in: Cheng, R. Y.-H. *et al.* Ex vivo engineered human plasma cells exhibit robust protein secretion and long-term engraftment in vivo. *Nat. Commun.* **13**, 1–14 (2022).[24]

2.1. INTRODUCTION

Despite prior demonstrations of engineered PC engraftment *in vivo*, a major challenge that remains is engineering long-lived engraftment. Despite the longevity of a subset of PCs in prior studies with either *in vitro* [15] or *in vivo* [14,16] maturation of engineered PCs, engineered antibody titers decreased rapidly following PC elicitation. These data imply that as a field we still lack a complete understanding of the factors needed to elicit an engineered population of long-lived PCs that are comparable in capacity and longevity to a vaccine-elicited long-lived PC [25,26]. A small minority of plasmablasts (PBs)/PCs that traffic to the BM are thought to become established long-lived PCs [7]. Consequently, long-lived PCs may not be intrinsically long-lived, but instead require factors delivered locally in the BM to support longevity. Multiple types of PC survival factors are present in the BM, including extracellular matrix and cytokines or chemokines produced by stromal cells, dendritic cells, megakaryocytes and eosinophils. One key pro-survival factor that supports PC longevity is Interleukin 6 (IL6). However, mouse IL6 does not efficiently activate the human IL6 receptor [27,28], a feature that has impeded modeling of human PC function *in vivo* in mouse systems.

We engineered human B cells to express non-antibody therapeutics, differentiated them into PCs and engrafted them for weeks into immunodeficient mice [9]. However, similar to other engineered PC experiments, the engrafted PCs exhibited limited longevity *in vivo.* Although *ex vivo* differentiation of engineered PCs offers significant advantages for the delivery of non-antibody therapeutics including precise dose-control, quiescence in the cell product, and low risk of mutation in the therapeutic protein sequence, the method will only be successful with development of a process that can elicit molecular features that lead to differentiation into long-lived, BM-resident PCs.

Here, we used single-cell RNA sequencing, electron microscopy and *in vivo* modeling to identify that long-lived engraftable PCs represent the ~30% of *ex vivo* derived cultures that are CD138+ and CD38hi. We found that this sub-population of *ex vivo* generated PCs exhibit structural and transcriptional features of PCs isolated from human BM. These PCs were capable of survival for greater than one-year in mice engineered to express hIL6. Finally, we enumerated long-lived human PCs in mice and estimated that ~50,000 PCs are sufficient for production of therapeutically relevant antibody titers (10 μg/mL).

2.2. MATERIALS AND METHODS

2.2.1. *Study Design*

Deidentified human PBMCs were acquired under informed consent from the Fred Hutch Specimen Processing and Research Cell Bank (protocol #3942). All animal studies were performed according to the Association for Assessment and Accreditation of Laboratory Animal Care (AAALAC) standards and were approved by the SCRI Institutional Animal Care and Use Committee (IACUC).

The aim of this study is to evaluate the requirement of human cytokines for longevity in engrafted *ex vivo* differentiated human PCs. We differentiated PCs from naive B cells *ex vivo* and characterized these cells using flow cytometry, RNA sequencing and transmission electron microscopy. Next, an *in vivo* experiment was designed to test whether human PCs will engraft in mice in NSG mice with or without synthetic expression of hIL-6 or hBAFF. The *in vivo* longevity of PCs was assessed by quantifying the abundance of human antibodies, by

mathematical modeling and luminescence imaging. We characterized the effect of human IL-6 on PCs by measuring BrdU incorporation, caspase activation and ELISPOT. Sample sizes in each experiment are clarified in each figure and legend. Each experiment has at least 3 replicates and *ex vivo* experiments are designed to at least 3 biological replicates from independent donors.

2.2.2. *PC differentiation ex vivo*

We isolated B cells from healthy donors' PBMCs (Fred Hutchinson Cancer Research Center) using the EasySep Human B cell isolation kit (Stem Cell Technologies). Isolated B cells were culture in Iscove's modified Dulbecco's medium (Gibco), supplemented with 2-mercaptoethanol (55M) and 10% FBS. Cells were cultured for seven days (activation) in medium containing 100 ng/mL megaCD40L (Enzo Life Science), 1g/ml CpG ODN2006 (invitrogen), 50 ng/ml IL-2, 50 ng/ml IL-10 (Peprotech) and 10 ng/ml IL-15 (Miltenyi), for three days (PB differentiation) in medium containing 50 ng/ml IL-6 (Peprotech) 50 ng/ml IL-2, 50 ng/ml IL-10 and 10 ng/ml IL-15 and three days (PC differentiation) in medium containing 50 ng/ml IL-6, 10 ng/ml IL-15 and 15 ng/ml interferon-2B (Sigma-Adrich)[9].

2.2.3. *Flow cytometry*

Flow cytometric analysis was performed on an LSR II flow cytometer (BD Biosciences) and events were analyzed using FlowJo software (Tree Star). Flow cytometry gating for fluorescent proteins and viability, and immunophenotyping can be found in supplementary Figures.

2.2.4. *CITE-seq sample preparation and sequencing*

Following *ex vivo* differentiation, cells were treated with Ficol to remove the debris. Viable cells were labeled with oligo-conjugated antibodies (Supplementary Table 1) for tracking surface expression and sample identity (HTO, Biolegend, Supplementary Table 1) labeling using the Biolegend Totalseq-B protocol. Next, we sorted viable cells with a FACSAria (BD). Sorted cells were loaded into 10X Genomics Chip G (10X Genomics), at 10,000 cells per lane. Next, we prepared libraries using 10X Genomics Chromium Next GEM Single Cell v3.1 kit following 10X user guide (CG000317). Libraries from cell surface tags and transcripts were evaluated by tapestation (Agilent) before sequencing. Finally, libraries were pooled in a ratio of 80% RNA, 20% oligos and sequenced with NextSeq 1000/2000 kit (Illumina) using the following read length: 28 bp Read1, 10 bp i7 Index, 10 bp i5 Index, and 90 bp Read2.

2.2.5. *Single Cell RNA-seq analysis*

Fastq files were processed by CellRanger based on the human reference genome GRCh38. The h5 file is then further analyzed by python script. Data is demultiplexed by hashsolo[29] and following analysis including normalized, trajectory inference (data clustered using the Louvain-graph-based algorithm and reconstructed the lineage relations by PAGA), and other hierarchical clustering, dimensional reduction and cell clustering is analyzed by python package scanpy[30].

2.2.6. *B Cell Subset Bulk RNA sequencing*

Following *ex vivo* differentiation, PCs were isolated using EasySep Human CD138 positive isolation kit and PBs were isolated from the flow-through using positive selection with a CD38

MicroBead Kit (Miltenyi Biotec). Isolated PBs and PCs were stored in Trizol in -80° C. RNA extraction was performed using a RNeasy mini kit (Qiagen). Following extraction, cDNA synthesis, library preparation and RNA sequencing was done in Benaroya Research Institute Genomics Core Lab using Clontech's SMARTseq and Illumina's NexteraXT kits.

2.2.7. *RNAseq analysis*

FASTQ files were filtered and adaptors were trimmed using Trimmomatic[31]. We then use STAR[32] to map high-quality reads to the human genome reference sequence (version hg38) and associate read counts with each gene. Differential gene expression analysis was performed using DEseq2[33] with a false discovery rate cutoff of 0.05. We also used paired t-tests to assess differences between cell types across four different donors. Functional annotation clustering was performed using DAVID (database for annotation, visualization and integrated discovery)[34,35] online bioinformatic resource with a cluster selection requirement of an enrichment score cutoff of 1.0 and a Benjamini–Hochberg adjusted p-value of 0.1.

2.2.8. *CRISPR AAV editing*

CRISPR RNAs (crRNAs) and AAV-based homology arms for targeting and gene delivery to the CCR5 locus were identified and validated previously[9]. Briefly, B cells were isolated and activated for 2 days (as described above), and electroporated (Lonza) in batches of 200 million B cells with 4 uM of ribonucleoprotein (RNP) containing sgRNA, trRNA and Cas9 protein (IDT) in molar ratio=1:1: 0.83. After electroporation, cells were transferred into activation medium (1.5 million cells/mL) in the presence of AAV6 encoding *CCR5* repair templates for delivery of

firefly luciferase or hBAFF (20% AAV by volume). Medium was changed 18 hours following AAV6 administration.

2.2.9. *TEM imaging*

Cells were fixed in ½ strength Karnovsky's fixative (2.5% glutaraldehyde, 2% paraformaldehype in 0.1 M sodium cacodylate buffer, pH 7.3) overnight at 40 C. After centrifugation, cell pellets were rinsed with 0.1 M cacodylate buffer, treated with 1% osmium tetroxide for 1 hour, rinsed with cacodylate buffer and dehydrated through a graded series of alcohols and propylene oxide. Pellets were then embedded in Eponate12 resin (Ted Pella, Inc)70 nm ultrathin sections were cut using a Leica EM UC7 ultramicrotome, contrasted with uranyl acetate and lead citrate and imaged on a ThermoFisher Talos L120c transmission electron microscope at 120 kV. Digital images were acquired with a Ceta 16M CMOS 4kx4k digital camera system. For quantification whether ER exists or not, 6 lab members were presented with labeled representative images, and with 100 mixed unlabeled images from B cells (pooled day2 and day13). Each member scored each unlabeled image based on their assessment of whether the ER content was low (i.e. the image looked like the labeled image of an activated B cell) or high (i.e. the image looked like the labeled image of a PC).

2.2.10. *Animal experiments*

NOD.Cg-*Prkdc*^{scid}*IL2rg*^{tm1Wjl}/SzJ (NSG) mice were purchased from Jackson Laboratory. NOD.CB17-*Prkdc*^{scid}*Il2rg*^{tm1}/Bcgen (B-NDG) mice and NOD.CB17-*Prkdc*^{scid}*Il2rg*^{tm1}*Il6*$^{tm1(IL6)}$/Bcgen (humanized IL-6 B-NDG) mice were purchased from

Biocytogen. All mice were kept in a designated pathogen-free facility at the Seattle Children's Research Institute (SCRI). In the transplant experiments, 8-12 week old mice were conditioned with 25 mg/kg Busulfan (Selleckchem) via intraperitoneal injection. 24 hr after conditioning, 10 million *ex vivo* reprogrammed B cells were delivered into each recipient *via* retro-orbital (Figure 4) or tail-vein infusion (all other experiments). Mice were bled and were imaged using an IVIS imaging system (Perkin Elmer) 10 minutes following subcutaneous injection of luciferin (10 L/g) following the indicated schedules. Following sacrifice, the BM cells were collected, phenotyped, and/or cultured *ex vivo*. Sex was randomized prior to cell transfer; both male and female animals were used in the analysis. Animals were housed at ambient temperature and humidity.

2.2.11. *Analysis of antibody and exogenous protein secretion*

ELISA to quantify humanIgG/IgM (Total ELISA kit, Invitrogen) and hBAFF (Human BAFF/BLyS/TNFSF13B ELISA kit, R&D systems) were performed per manufacturer instructions (Supplementary Table 1). Single-cell antibody secretion was measured by ELISPOT (Supplementary Table 1). BM cells (500,000 cells per well) and *ex vivo* cultured PCs (4000 cells per well) were serially diluted four times, 2-fold on IgG (H+L) Cross-Adsorbed Goat anti-Human (Invitrogen) precoated MSIPS4W10 plates (Millipore). After 24 hours, the plates were washed and treated with Goat Anti-Human IgG-HRP (Southern Biotech). Detection of the secondary antibody was accomplished using peroxidase (AEC Substrate Kit, Vector Laboratories), and spots were read by an ImmunoSpot analyzer (Cellular Technology Limited). Images from each well with spot numbers below 50 were analyzed by Fiji ImageJ (2.1.0). The Macros code for batch analysis can be found in supplementary materials. The analysis detail and rationale are as previously described[36]. All the outputs in the csv format are then concatenated by

python script, and the histogram and kernel density estimate curves were computed by seaborn[37] and matplotlib[38] packages.

2.2.12. *Data availability*

The Bulk RNA sequencing read data in this study are available on GSE211984, and the single-cell and CITE-seq read data in this study are available on GSE212138. The complete list of all the studies is provided as Source Data. Source data are provided with this paper.

2.2.13. *Code availability*

The data was analyzed using published software packages and scripts. A python notebook was used to call routine statistical functions and to organize the data. In addition, the python source code used to perform data analysis is available from GitHub at (https://github.com/Rene2718/Long-term-engraftment-of-engineered-human-plasma-cells-).

2.3. RESULTS

2.3.1. *Single cell transcriptomics illustrate the heterogeneity of ex vivo differentiated human PCs*

Previously, we found that differentiation of human B cells into cultures containing antibody secreting cells results in a heterogeneous mixture of phenotypes[9]. To better understand this heterogeneity in *ex vivo* differentiated PCs, we evaluated B cells isolated from peripheral blood mononuclear cells (PBMC[TP1] [JR2]) from two donors immediately following cell expansion with T cell cytokines (day 7, Fig. 2.5.1a) and following differentiation (day 13, Fig. 2.5.1a) in culture

using cellular indexing of transcriptomes and epitopes (CITE-seq; Fig. 2.5.1b, and Table 2.6.1). To describe the differentiation of human B cells, we used PAGA for trajectory inference and the Louvain-graph-based algorithm to cluster cells, including both gene expression and CITE-seq surface marker quantification. We chose the root cluster to be that with the highest expression of the B cell markers MS4A1, CD19, IGHD, MHC-class II, and lowest expression of the PC markers CD38 and IgG[39,40] . We found that cells from each donor were detected at similar proportions in all clusters, which suggested that donor-donor variability did not contribute significantly to the overall results. Additionally, while cells from day 7 and day 13 were generally grouped into time-specific subclusters (Fig. 2.5.1b, left panel), we found some cells from the day 13 samples in the clusters predominantly containing day 7 cells and vice versa, which indicated that differentiation into PCs is ongoing. The clusters containing day 7 cells expressed markers of activated B cells (cluster 1 and cluster 6), B-blast (proliferating pre-PB, cluster 2), and pre-PB (cluster 4). In contrast, we found day 13 cells within interferon-stimulated activated B cells (cluster 3) and PB/PCs (cluster 0 and cluster 5). To verify the identity of the clusters, we plotted B cell programming master transcription factors (TFs): PAX5 (B cell TFs), EZH2 (Pre-PB TF), IRF4 and XBP1 (PC differentiation TFs) (Fig. 2.5.1c).

We observed two primary trajectories (Fig. 2.5.1b right). The first trajectory closely followed canonical B cell differentiation, starting from cells with markers of B cell activation (Fig. 2.5.1d, AICDA in Fig. 2.5.1c), MHC-class II (Fig. 2.5.1d), and proliferation (MKI67, Fig 2.5.1c); this trajectory includes PB and PC clusters with high expression of various immunoglobulins (Fig. 2.5.1d). As expected, surface marker expression via CITE-seq shows that B cell receptor (BCR/ anti-IgM oligos) expression decreased along pseudotime while the PC marker, CD38 (anti-CD38 oligos) increased (Fig. 2.5.1e). The major trajectory of B cells from

our culture system aligns closely with PC development. In the second and more minor trajectory (cluster 1/3), day 13 cells retain an activated B cell-like signature, however the predominant differences between day 7 and day 13 are interferon-induced genes, presumably due to IFN-alpha included in the B cell differentiation media (Fig. 2.5.1d).

Ex vivo differentiated PC cultures contain a heterogeneous mixture of phenotypes, including $IgM^{hi}CD38^{lo}$, $IgM^{lo}CD38^{lo}$, $CD38^{hi}CD138^{lo}$, and $CD38^{hi}CD138^{hi}$. Using a CITE-seq panel detecting these surface markers (Fig. 2.5.1f left), we superimposed the phenotype subsets onto the gene expression UMAP (Fig. 2.5.1f right, Fig. 2.5.1g). As expected, we found the majority of $IgM^{hi}CD38^{lo}$ cells mapped to clusters expressing an activated B cell signature. A small subset of these cells mapped to IgM PCs (clusters 3, 5), which indicates that these antibody secreting cells (ASC) likely retain surface BCR. We found that the UMAP clusters were driven predominantly by unique immunoglobulin isotypes and light chains and the $CD38^{hi}CD138^{lo}$ and $CD38^{hi}CD138^{hi}$ populations were scattered within those subclusters. One exception was that IgA and IgM PCs exhibited proportionally fewer $CD38^{hi}CD138^{hi}$ cells (Fig. 2.5.1f-g).

We next used gene set enrichment analysis to compare $CD38^{hi}$ to $CD38^{lo}$ cells within *ex vivo* differentiated PCs. We found that $CD38^{hi}$ are enriched for transcriptional signatures found in PC datasets[8,41,42]). Examples of genes enriched in $CD38^{hi}$ (Fig. 2.5.1h) are those that regulate secretory organelles (endoplasmic reticulum, golgi, secretory granule membrane) and antibody production (immunoglobulin, protein transport). As expected, canonical PC genes including CD38, CD138 (SDC1), SLAMF7, BCMA, PRDM1 and XBP1 (Fig. 2.5.1h). We next compared $CD38^{hi}CD138^{lo}$ and $CD38^{hi}CD138^{hi}$ cells and found that SDC1 (CD138), several IgG isotypes, and several adhesion molecules are enriched in CD138hi cells (Fig. 2.5.1h). Collectively, these

transcriptional features of *ex vivo* cultured human B cells align with our prior understanding of B cell differentiation into PCs[8,41,42].

2.3.2. *A subset of ex vivo differentiated PCs resemble bone marrow ASCs*

Despite literature showing that mitochondrial metabolism is important for PC differentiation[43–45], the single cell sequencing analysis did not unearth transcriptional changes associated with mitochondria. To address whether this signature PC feature is present in *ex vivo* differentiated PCs, we measured mitochondrial volume and stress in differentiated B cell subsets using the vital dyes MitoTracker Green and MitoTracker Red CMXRos respectively (Fig. 2.5.2a-b). MitoTracker Green staining was greater in $CD138^{hi}$ cells relative to $CD38^{+}$ cells. On the other hand, MitoTracker Red CMXRos staining was higher in differentiated B cells ($CD38^{++}$ and $CD138^{hi}$) compared to active B cells/blast ($CD38^{-}$ and $CD38^{+}$), which indicates that mitochondrial membrane potential increases as a function of *ex vivo* differentiation of B cells into PCs.

We next investigated whether *ex vivo* differentiation of B cells led to morphologies exhibited by human PCs. Transmission electron microscopy (TEM) showed that approximately 50% of day 13 differentiated B cells have increased endoplasmic reticulum content relative to day 2 activated B cells (Fig. 2.5.2c; quantification, Fig. 2.5.2d). We also observed condensation of mitochondria in the *ex vivo* differentiated PCs (Fig. 2.5.2c), which is indicative of active respiration[46]. These observations are consistent with previous observations of PC morphology[47] and demonstrate that *ex vivo* differentiated PCs share morphological features with human BM PCs.

2.3.3. *Ex vivo differentiated PCs home to the BM and CD138+ cells stably engrafted in an immunodeficient mouse model*

One of the important long-lived PCs features is homing to the BM[8,48]. To examine if *ex vivo* differentiated PCs can home to and be retained in the BM, we designed a gene-editing based luciferase reporter that could be monitored *in vivo*. We introduced the firefly luciferase coding sequence into an AAV-based repair template with homology arms that facilitate insertion and expression within the CCR5 locus following CRISPR-mediated gene editing[9] (Fig. 2.5.3a). We isolated and activated human B cells and introduced firefly luciferase using this template for homology directed repair (HDR)-based gene addition. After differentiation of edited cells into PBs and PCs, we isolated genomic DNA from a subset of cells and quantified HDR using ddPCR; 18.63% of alleles exhibited integration of the luciferase repair template.

Luciferase engineered PCs were transferred into NOD.Cg-*Prkdc*^{scid}*IL2rg*^{tm1Wjl}/SzJ (NSG) immune deficient mice (10 million cells per recipient), and subsequently tracked using *in vivo* imaging (Fig. 2.5.3a schematic). Two days post-transfer, gene edited cells accumulated in the hindlimbs and chest region (Fig. 2.5.3b-c; Fig. 2.5.4a). The signal localized to the chest diminished over time, likely reflecting initial trafficking of transferred cells to the lung or liver. In contrast, the signal in the hindlimbs and the sternum remained stable from day 15 to day 51 (Fig. 2.5.3b-c, Fig. 2.5.4a). Furthermore, human immunoglobulin G (hIgG) and human immunoglobulin M (hIgM) dynamics are consistent with luciferase signal (Fig. 2.5.3d; Fig. 2.5.4b-c). To measure the functional capabilities of the transferred PCs, we quantified hIgG by ELISA for up to one-year after transfer. Consistent with the luciferase imaging, hIgG peaked two

weeks post-transfer, diminished rapidly over the subsequent month and subsequently stabilized (Fig. 2.5.4c) at concentrations between 1000-3000 ng/ml for a year post adoptive cell transfer (Fig. 2.5.4c). These results demonstrate that *ex vivo* derived B cell populations can home to the BM, and that a subset of these cells reside within the BM and stably produce antibodies for as long as one year.

To investigate which populations in the *ex vivo* cultures are responsible for long-term *in vivo* engraftment, following *ex vivo* differentiation, we enriched for $CD138^+$ and $CD138^-$ cells and infused these subpopulations into NSG mice (Fig. 2.5.3e). We found that the $CD138^+$ cells engrafted similarly to unenriched cells, and that $CD138^-$ cells engrafted poorly (Fig. 2.5.3f-g). To investigate the differences between $CD138^+$ and $CD138^-$ PCs, we used bulk RNA sequencing. As we observed in the CITE-seq data (Fig. 2.5.4d), immediately after differentiation, several apoptotic genes were downregulated in $CD138^+$ PCs (Fig. 2.5.4e). Furthermore, upon culture of the $CD138^+$ cells for 6 additional days, we found that the PC homing markers CXCR4, CXCR6, and LFA-1[8,48], are increased in CD138+ PCs (Fig. 2.5.4f). Finally, negative (SOCS3;[49]) and positive (IL6R) regulators of IL-6 signaling, were decreased and increased respectively (Fig. 2.5.4f), suggesting that IL-6 signaling was upregulated in cultured PCs. Collectively, transcriptional changes in $CD138^+$ PCs likely contribute to engraftment and survival of *ex vivo* differentiated PCs *in vivo.*

2.3.4. *Human IL-6 and BAFF promote engraftment of ex vivo differentiated PCs*

We hypothesized that the decline in hIgG production over time in the mouse model might be partly explained by the lack of key human cytokines produced by the BM of NSG mice. For

example, mouseIL-6, a cytokine critical for PC longevity[6], does not efficiently activate human IL6R[27,50]. To test whether hIL-6 can improve survival or engraftment of *ex vivo* differentiated human PCs in NSG mice, we created a humanized IL-6 mouse model by delivering hIL-6 to neonates via lentiviral injection (schematic, Fig. 2.5.5a). Again, we generated *ex vivo* differentiated PBs and PCs, and adoptively transferred these cells into either control or similarly aged NSG recipients that were engineered via neonatal transduction with lentivirus expressing hIL-6 (serum hIL-6 quantified in Fig. 2.5.6a). hIgG production by engrafted PBs and PCs in mice expressing hIL-6 was significantly increased ~3-fold at all time points (Fig. 2.5.5b and Supplementary Fig. 4b). Furthermore, the antibody levels are highly correlated with hIL-6 in mice serum (Pearson correlation in Fig. 2.5.6c, quantified antibodies in Fig. 2.5.5b and Fig. 2.5.6e, hIL-6 in Fig. 2.5.6d).

Human BAFF (hBAFF) is a secreted protein produced by several myeloid subsets and B cells that enhances hIgG production by PCs *in vivo*[7,51,52]. To mimic local hBAFF production, we used HDR-based editing to introduce hBAFF and a cis-linked GFP reporter into human B cell cultures via delivery to the *CCR5* locus as previously described[9]. B cells edited to express hBAFF exhibited several significant changes in culture including higher proportions of CD38+ cells, IgG+ cells, and increased proliferation relative to B cells edited to unedited B cells (Fig. 2.5.7). We found that hBAFF-edited B cells transferred into NSG mice stably secreted higher levels of hIgG than unedited B cells (Fig. 2.5.5b-c). Additionally, B cells expressing hBAFF transferred into hIL-6-expressing mice produced higher quantities of hIgG (Fig. 2.5.5c), hIgM (Fig. 2.5.6e) and hBAFF (Fig. 2.5.5d) than those introduced into control NSG mice, indicating that hIL-6 and hBAFF acted in an additive way to promote PC longevity and/or protein production. Together, these findings demonstrate that provisioning NSG mice with human

cytokines enables long-term engraftment (>1 year) and antibody production (>10g/mL) by *ex vivo* differentiated human PCs.

2.3.5. *Modeling the dynamics of PC in vivo (Mathematical model 1)*

Following adoptive transfer of *ex vivo* differentiated human PCs, hIgG abundance rose sharply in the first 14 days post-engraftment. hIgG levels then decreased rapidly and stabilized starting at approximately 60 days post-engraftment. We hypothesized that distinct PC cell populations are responsible for this complex dynamic: a relatively large number of short-lived PCs contributing to the early increases in hIgG, whereas a smaller number of long-lived PCs responsible for stable hIgG production.

The number of ASCs and hIgG immediately following cell transfer is hard to model due to the following reasons: (1) Post-transfer, much of the inoculum accumulates in the lung and liver. A large percentage of transferred B cells are subsequently cleared by the host, potentially leaving only a small percentage of surviving cells. (2) We expect a portion of the cell inoculum to differentiate following *in vivo* transfer. (3) *In vitro* experiments indicate that the hIgG secretion rate, γ, is approximately steady 21 days following *ex vivo* differentiation. Therefore, for the purposes of this model, we fixed γ as a parameter. Finally, based on BRDU labeling of transferred cells, terminally differentiated PCs do not divide at a measurable rate; therefore in this model, we solely consider their death rate (decay).

Let us denote the number of PC as N and the amount of antibody hIgG as G. Their dynamic can be modeled by the following equations.

$$\frac{dN}{dt} = -\beta N \qquad (5.1)$$

$$\frac{dG}{dt} = \gamma N - \lambda G = \gamma N_0 e^{-\beta t} - \lambda G \qquad (5.2)$$

where β represents the PC decay rate, γ represents the hIgG secretion rate, and λ represents the clearance rate of hIgG. The solution of eq.5.2, the amount of antibody at a give time (t) is

$$G(t) = \frac{\gamma N_0}{\lambda - \beta}(e^{-\beta t} - e^{-\lambda t}) \qquad (5.3)$$

The parameters γ, λ are described previously [36,53–55]. We used Eq. 5.3 to model the PC behavior and fit the initial number of PCs that survive transit through the lung/liver, and/or differentiate and survive *in vivo* beyond 21 days (denoted as N_0) and the decay rate (β) of these cells (Fig. 2.5.8a). In this model, we explicitly ignore short-lived PCs that produce antibodies initially following transfer, but are not stably retained. We applied this model to discriminate between the experimental conditions (Fig. 2.5.5e-f). Based on the fitted results, the decay rate of long-lived PCs was similar in cells engrafted into hIL-6 expressing mice and those engrafted into control mice (Fig. 2.5.5g). However, hIL-6 increased the number of PCs capable of long-term engraftment that were retained in the BM immediately post transfer (Fig. 2.5.5h and schematic, Fig. 2.5.5i). In contrast, cell intrinsic expression of hBAFF appears to boost the initial PC numbers (Fig. 2.5.8b; top panel) but this is accompanied by more rapid decay (Fig. 2.5.8b; bottom panel). These data support prior reports showing that BAFF promotes expansion of PBs[7,56,57]. Finally, based on our estimates, approximately 500,000 PCs (~5% of the inoculum) are reproducibly retained in hIL-6 expressing mice, of which approximately 50,000 long-lived PCs are still present after 1 year (Fig. 2.5.8c-d).

To investigate whether the mathematical model was supported by experimental data, we next investigated whether recipient NSG mice that express hIL-6 exhibited an increase in the

proportion of PCs initially retained following engraftment. Again, we engineered *ex vivo* differentiated B cells to express luciferase and transferred these populations into hIL-6-transduced or control mice. Three days after infusion, we observed a significant increase in both the luciferase signal (Fig. 2.5.8e-f) and the level of secreted hIgG (Fig. 2.5.8g) in mice expressing hIL-6. Together, these observations support the conclusion that systemic hIL-6 primarily facilitates an increase in the number of PCs initially retained in the BM following adoptive transfer.

2.3.6. *Physiologic expression of hIL-6 promotes retention of BM engrafted PCs*

To explore features that regulate engraftment of *ex vivo* differentiated PCs in mice that express hIL-6 under physiological control, we made use of an immune deficient model with hIL-6 knocked into the mouse *Il6* locus. *Ex vivo* differentiated PCs engineered to express luciferase were engrafted into hIL-6-expressing mice or control animals, and evaluated in several ways (schematic, Fig. 2.5.9a). As we observed in mice physiologically expressing hIL-6, luciferase detected from edited B cells was retained in the BM at higher rates in hIL-6 mice than in controls (Fig. 2.5.9b). Similarly, we found that hIgG (Fig. 2.5.9c) and hIgM (Fig. 2.5.9d) levels were significantly higher in hIL-6 animals relative to control animals. In each experiment, we found that the differences in luciferase initially became apparent at 48 hours following transfer, suggesting that hIL-6 promotes retention of engrafted PCs in the BM.

To evaluate the phenotypes of engrafted human B cells, we sacrificed the animals 28 days post-transfer, and used flow cytometry to characterize the human cells in the BM. As expected, the human cell engraftment ($hCD45^+$) was higher in hIL-6 mice than in controls (Representative image Fig. 2.5.9e). Additionally, in both mouse hosts, most human cells

exhibited features expected in PCs including expression of CD38, CD138, and the antibody isotypes hIgA, hIgG or hIgM (Fig. 2.5.9e-f, while only IgG, IgM and CD138^{lo} subsets have significant differences under a significance level of $\alpha = 0.1$). We found that the number of durably engrafted hIgG PCs was approximately 10,000 / 10^8 BM cells. In humanized mice, the number of hIgG$^+$ PCs was highly correlated with hIgG abundance (Pearson's r = 0.93) in hIL-6 mice (Fig. 2.5.9g). Collectively, the luminescence, ELISA and cell phenotype data indicated that hIL-6 increased retention of PCs and longevity in immune deficient mice.

2.3.7. *Modeling the dynamics of PCs ex vivo (Mathematical model 2)*

We predicted that the boost in PC retention in the BM caused by hIL-6 was due to differences in death or proliferation of *ex vivo* differentiated PCs in animals upon transfer (Fig. 2.5.10a). To investigate how PC turnover is regulated by hIL-6, we differentiated PCs *ex vivo* using a three-stage culture system, isolated CD138$^+$ PCs and cultured them for an additional 21 days in the presence or absence of hIL-6. We quantified the number of surviving PCs over time and found that cell numbers decreased in both conditions. In models of short-term *in vitro* studies, we found that β as a parameter is only able to fit the first 6 days of observation (Fig. 6c, dash line). That is, the decay rate (β) of PCs immediately following *ex vivo* differentiation during the first 21 days of our observation changes with time. Notice that $\beta(t) = -dlnN/dt$, where the latter (change in PC number over time) can be estimated from the counting data (Fig. 2.5.11). We observed that $dlnN/dt$ has a linear-like decay. Therefore, we use $\beta(t) = \beta_0 + \beta_1' t$ to characterize the changes in decay rate over time and fit β_0 and β_1'. The ODE solution of $N(t)$ is,

$$N(t)/N_0 = e^{-(\beta_0 t + \beta_1 t^2)} \qquad (7.1)$$

The resulting dynamics of fitted β_0 and β_1 matched the data (Fig. 2.5.10c, solid line), and we presented all the fitted dynamics of all samples with hIL6 and without hIL6 (Fig. 2.5.10b). β_0 is the initial value of β. It can be interpreted as the acute effect of hIL6. β_1 is the slope of $\beta(t)$, characterizing the changes in decay rate over time. We observed that the fitted β_1 (Fig. 6d) are negative, demonstrating that PC decay rate decreased over time (Fig. 2.5.11). Here, negative $d\beta/dt$ can be explained by two possible factors. (1) The PC cells are initially composed of subpopulations with different decay rates $\{\beta^{(1)}, \beta^{(2)}, \beta^{(3)}, \ldots, \beta^{(m)}\}$, and based on Fisher's fundamental theorem of nature selection (FTNS), the decay rate becomes smaller as cells with larger proliferation rate or smaller death rate will dominate the population overtime [58]. (2) A subset of PCs can mature in culture and differentiate into long-lived PCs over time $\{\beta^{(1)}(t), \beta^{(2)}(t), \beta^{(3)}(t), \ldots, \beta^{(m)}(t)\}$, so intrinsically the decay rate is changing. We found that the initial value of decay rate, β_0, is significantly affected by hIL6 (p-value = 0.003) (Fig. 2.5.10d). The distributions of β with or without hIL6 for the first 6 days are prominently separated Fig. 2.5.11).

β_0's predominant difference aligns with the drastic change of $E[ffluc_{IL6+}]/E[ffluc_{IL6-}]$ for the first 3 days *in vivo* (Fig. 2.5.9b). We further show that the slope of β, characterized by β_1, is also different (Fig. 2.5.10d, p-value = 0.03). The difference in β_1 shows the β eventually converge to a similar level at day 21 even with significant difference at the beginning, which matches the closeness of β from the long-term model (Fig. 2.5.4i). Therefore, we see the converged decay rate from the two systems (hIL6 versus vehicle). The linear model of β can characterize the decay of β in 21 days as well. However, at the later stage of the decay, we observed that hIL6 does not affect β at later time points, although it is possible that other human cytokines or molecules would decrease cellular decay following establishment of populations of long-lived PCs.

Using this mathematical model, we found the nature of newly generated PCs are still undergoing further differentiation with more anti-apoptotic ability or/and PCs without anti-apoptotic just died and selectively remained the anti-apoptotic PC. And that hIL-6 promoted early, but not later PC survival.

2.3.8. *hIL-6 increases survival of ex vivo differentiated PCs by inhibiting apoptosis of $CD138^{lo}$ PCs*

To examine whether hIL-6 affects proliferation of ex vivo differentiated PCs or PBs, we repeated the three-stage differentiation culture, isolated CD138+ cells and CD138- cells and further cultured each population for 72 hours. At this point, we introduced BrdU and continued culturing for an additional 72 hours. Neither differentiated PCs nor differentiated PBs exhibited substantial amounts of proliferation *ex vivo* (Fig. 2.5.10e; <1% of cells divided in this 72 hour period), although we did find that BrdU labeling was significantly higher in CD138+ PCs in the presence of hIL-6.

Next, we directly measured the impact of hIL-6 on cell death. We quantified caspase activation using flow cytometry at several time points (1, 24 and 48 hours) following termination of the three-stage differentiation cultures. hIL-6 decreased active caspase levels in $CD138^{lo}$ PCs ($CD38^{hi}CD138^{lo}$; Fig. 2.5.10f), but not in active B cells or $CD138^{hi}$ PCs. We also found that relatively few $CD138^{hi}$ cells exhibited activated caspase, indicating that upon terminal differentiation to PCs, B cells exhibit increased survival. Together, these observations

demonstrate that hIL-6 primarily regulates PC durability by increasing cell survival immediately following differentiation.

2.3.9. hIL-6 increases per-cell secretion rate in PCs

In addition to durability of PC engraftment, the per cell secretion rate also contributes to total antibody production. To examine whether treatment with hIL-6 alters PC per cell secretion rate, we differentiated PCs using the three-stage culture method, and cultured $CD138^{+}$ cells for several time periods in media containing hIL-6 or vehicle. At each time point (0 days, 6 days, 11 days, 16 days and 21 days; schematic Fig. 2.5.10g), we resuspended a fixed number of cells in fresh media, collected media for hIgG quantification by ELISA. We found that *ex vivo* differentiated PCs treated with hIL-6 exhibited significantly larger quantities of hIgG (Fig. 2.5.10h) per cell from day 13.5, with the mean value approximately 50 pg/cell/day. We next quantified protein production at a single cell level using hIgG ELISPOT from *ex vivo* differentiated PCs cultured for 21 days with or without hIL-6. For each spot, we calculated spot intensity and plotted the ELISPOT size distribution using cells derived from three donors (Fig. 2.5.10i). We observed substantial heterogeneity in protein production between ASCs (approximately 10-fold). However, we found that PCs treated with hIL-6 had many more high-producing cells and an increased mean spot size (Fig. 2.5.10j). To examine whether *in vivo* exposure to hIL-6 alters protein secretion on a per cell basis, we quantified hIgG secretion from PCs isolated from the BM of mice engrafted with *ex vivo* differentiated PCs (see Fig. 2.5.4a). Similar to the *ex vivo* observations, PCs isolated from hIL-6 mice exhibited more high producing cells (Fig. 2.5.10k) and increased mean spot size (Fig. 2.5.10l). Finally, we adjusted the assumptions of our mathematical model of PC engraftment to account for different antibody

secretion rates in hIL-6 expressing mice (Table 2.6.2). The remodeling results (Fig. 2.5.12) did not alter the earlier conclusion that hIL-6 promotes retention of PCs in BM. Collectively, these data demonstrate that exposure to hIL-6 increases the survival, retention in BM and protein secretion of *ex vivo* differentiated PCs.

2.4. DISCUSSION

In this study, we show that human B cells can be differentiated *ex vivo* into PCs that exhibit multiple key features of long-lived PCs found within human BM including the transcriptional and metabolic program, cell surface phenotype and *in vivo* longevity and capacity for sustained endogenous protein production. The cell surface phenotype ($CD19^{lo}CD38^{hi}CD138^{+}$) and transcriptional features of *ex vivo* derived PCs closely resemble human long-lived antigen-specific ASCs[6]. Most notably, we show that *ex vivo* differentiated PCs migrate to the BM where they are retained and functional for > one year, demonstrating longevity, as well as sustained exogenous protein production following adoptive transfer. Finally, we show that *ex vivo* differentiated human PCs are dependent on signaling from hIL-6 for retention in the BM, survival following differentiation and optimal secretory capacity.

We demonstrate that *ex vivo* terminally differentiated PCs can survive *in vivo* for longer than a year in immunodeficient mice. Following vaccination, endogenous human PCs can compete into, and be retained within the BM niche well into adulthood[59]. Our data imply that immunodeficient mice lack key features that promote human PC survival in the BM niche, and thus underestimate the longevity of *ex vivo* derived PCs. Supporting this idea, we found that the half-life of human PCs in immunodeficient mice is approximately 138 days (based on decay rate,

0.005), which is comparable to mouse PC longevity in response to immunization[25,26]. In larger animals like rhesus macaque[60] and human beings[61], tetanus-specific PCs have a half-life of ~1350 days and ~4000 days respectively. Therefore, we hypothesize that transfer of autologous engineered human PCs will likely exhibit higher longevity in human hosts than in immunodeficient mice.

A possible reason that human PCs exhibit decreased engraftment capacity in mice is imperfect interactions between mouse cytokines and human receptors. Proteins involved in PC homing like CXCL12 and its receptor CXCR4 exhibit high degrees of homology (90% and 92% amino acid conservation respectively) and are likely cross-reactive between species[62,63]. Additionally, the integrin adhesion molecule LFA-1 can interact with mouse ICAM-1[64]. Despite some reported conservation in PC-regulating proteins, several cytokines are not as well conserved between the species. For instance, the BAFF (72% conservation) and BAFFR (54% conservation) interaction is imperfect as evidenced in engraftment studies showing that human PBMCs into hBAFF knock-in mice led to increased immature B cell development[65]. IL-6 (39% conservation) and IL6R (52%) are also poorly conserved between human and mouse. In a previous study, immunization of human CD34 grafts is greatly improved in hIL-6 knock-in mice[66]. In contrast to such studies, our work was designed to evaluate how human cytokines impact retention and durability of mature human PCs; a setting that tests the requirement for human cytokines in establishing and/or maintaining PC longevity. Whereas hIL-6 promoted PC retention/durability in our model, hBAFF also increased BM PC retention. Our findings are in contrast to prior work showing that hBAFF inhibits PC-dependent immune responses in a humanized mouse model[65]. We hypothesize that these differences reflect expression of hBAFF by the transferred PCs; a setting that may mimic local increases in hBAFF and/or membrane presentation as might occur

following immune activation. Our composite findings suggest that additional studies of *ex vivo* differentiated PCs (in hIL-6 mice or in animals expressing additional human cytokines) will help to identify other key aspects of human PC biology including surface receptor interactions, niche structure and support cells, and events that modulate competition of PCs into the BM niche. Experiments are in progress to explore the importance of cross-reactivity in additional cytokine (e.g., APRIL; 85% conserved) and receptor (e.g., TACI, BCMA; 51% and 62% conserved) interactions in PC modeling.

Survival of human[6,67] and mouse[68] BM-derived PCs *ex vivo* is augmented by co-culture with BM stromal cells or treatment with cytokines thought to be present in the BM microenvironment. Additionally, several factors found in BM stromal cell supernatants, including IL-6, promote *ex vivo* survival of antigen-specific mouse[68] and human[6,69] PCs. Our *in vitro* observations indicate that IL-6 can promote longevity via anti-apoptotic effects on $CD38^{hi}CD138^{lo}$ cells. Consistent with the idea that IL-6 promotes survival prior to terminal PC differentiation, the *in vivo* effect provided by IL-6 is most pronounced during the first month following transfer of *ex vivo* derived B cells. Similarly, while APRIL, BM stromal cell supernatants and hypoxia provide a significant immediate survival benefit to the blood-derived tetanus-specific PCs, the decay rate in *ex vivo* culture is similar across conditions[42]. Together, these results imply that survival benefits conferred by many BM cytokines could occur during PC maturation rather than following maturation. Finally, it is possible that persistence of *ex vivo* derived PCs in an immune competent setting could be boosted by treatments that transiently promote hIL-6 secretion, which is a topic of active investigation. Collectively, these data suggest that *ex vivo* derived PCs are sufficient to acquire a long-lived phenotype *in vivo*, but their survival is increased by IL-6-like signals along with APRIL and other possibly other BM-derived factors.

Although the full determinants for acquisition of a long-lived PC phenotype remain to be determined, recent evidence suggests that long-lived PCs require alterations in mitochondrial function and glucose uptake[45]. The transcriptional changes we observed in *ex vivo* derived PCs cultured for longer time periods are consistent with these prior findings. Although human BM PCs can be either $CD19^{+}$ or $CD19^{-}$[6,70], it has been proposed that CD19 loss is required for a long-lived PC phenotype. We observed a decrease in CD19 expression from day13 to day19 in *ex vivo* PC culture. However, *ex vivo* culture derived, long-lived PCs engrafted in humanized mice retained CD19 expression, albeit at low levels. Thus, loss of CD19 is not a prerequisite for a long-lived human PC phenotype. Finally, a striking observation from our study is that hIL-6 not only promotes long-term PC engraftment, but also functions to increase per cell antibody secretion rates. The distinct effects of hIL-6 on PC engraftment and protein production both likely contribute to the observed differences in long-term antibody production in the NSG-hIL-6 model and could also contribute to increased secretion of engineered proteins by a PC-derived cell therapy.

In summary, our findings help to deconvolute the multiple impacts of hIL-6 on generation and engraftment of long-lived human PCs. Further, future studies using the *ex vivo* PC generation and adoptive transfer platform described here, will help to uncover additional fundamental features of long-lived PCs, and in parallel, support the capacity to build and test PC-based cell therapies.

2.5. FIGURES

2.5.1. *Single cell transcriptomics illustrate the heterogeneity of ex vivo differentiated human PCs*

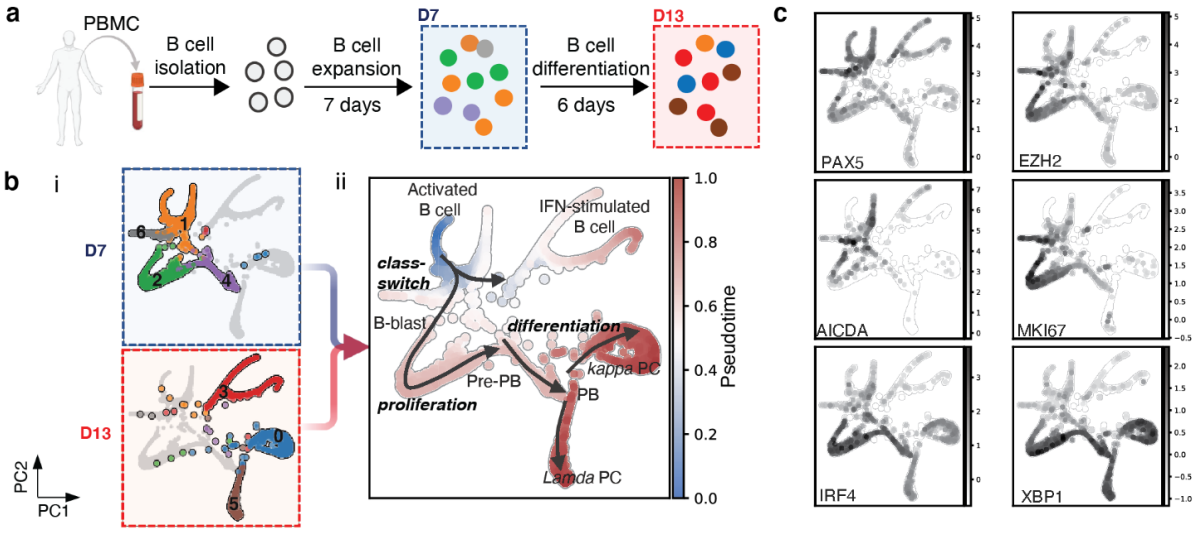

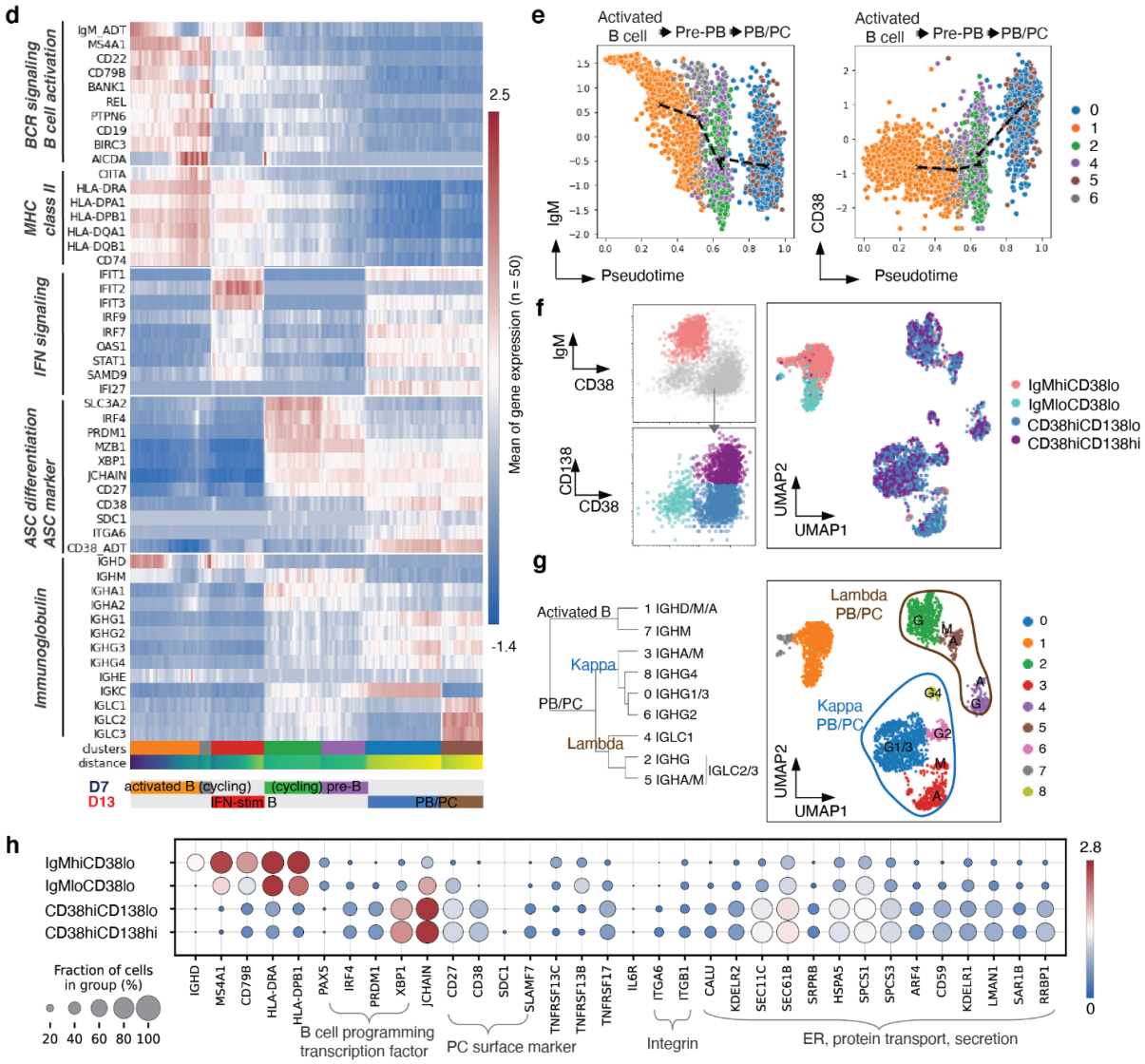

(a) Schematic of B cell culture ex vivo, and experimental setup: day 7 and day 13 cells were collected for CITE-seq. It was partially created with BioRender.com. **(b)** Single cell graph by PAGA trajectory analysis of day 7 and day13 cells, and heatmap by inferred pseudotime of all cells (n = 6011) from both time point and 2 biological replicates. Trajectory starts from the initial state node (cluster 1, activated B cells from day 7 cells) and ends at terminal state nodes (cluster 0/5, kappa/lambda PCs from day13 cells). Cell differentiation states in between are labeled according to their representative cell status. **(c)** Single cell trajectory graph heatmap showing expression of representative genes which indicate each cell status. **(d)** Expression heatmap of

Louvain clusters, gene sets in each pathway show gene regulation along B cell development. Each data point present in the heatmap is computed by the average of normalized gene expression from 50 cells. (**e)** Surface protein (antibody-derived tag) expression trend along pseudotime. BCR expression is downregulated and CD38 expression is upregulated during PC differentiation. **(f)** Classification of B cell subsets categorized by the indicated protein markers: $IgM^{+}CD38^{lo}$, $IgM^{-}CD38^{lo}$, $IgM^{+}CD138^{lo}$ and $IgM^{+}CD138^{hi}$. UMAP dimension-reduction projection of day13 B cells (n = 2897) from two biological replicates. (**g)** Predominant immunoglobulin expression in each subset from **f**. (**h)** Dotplot visualization of day 13 B cells (n = 2897): subsets are listed on y-axis and genes (features) are listed along the x-axis. Dot size represents percentage of cells in a group expressing each gene; dot color indicates mean expression level in a group.

2.5.2. *A subset of ex vivo differentiated PCs resemble bone marrow ASCs*

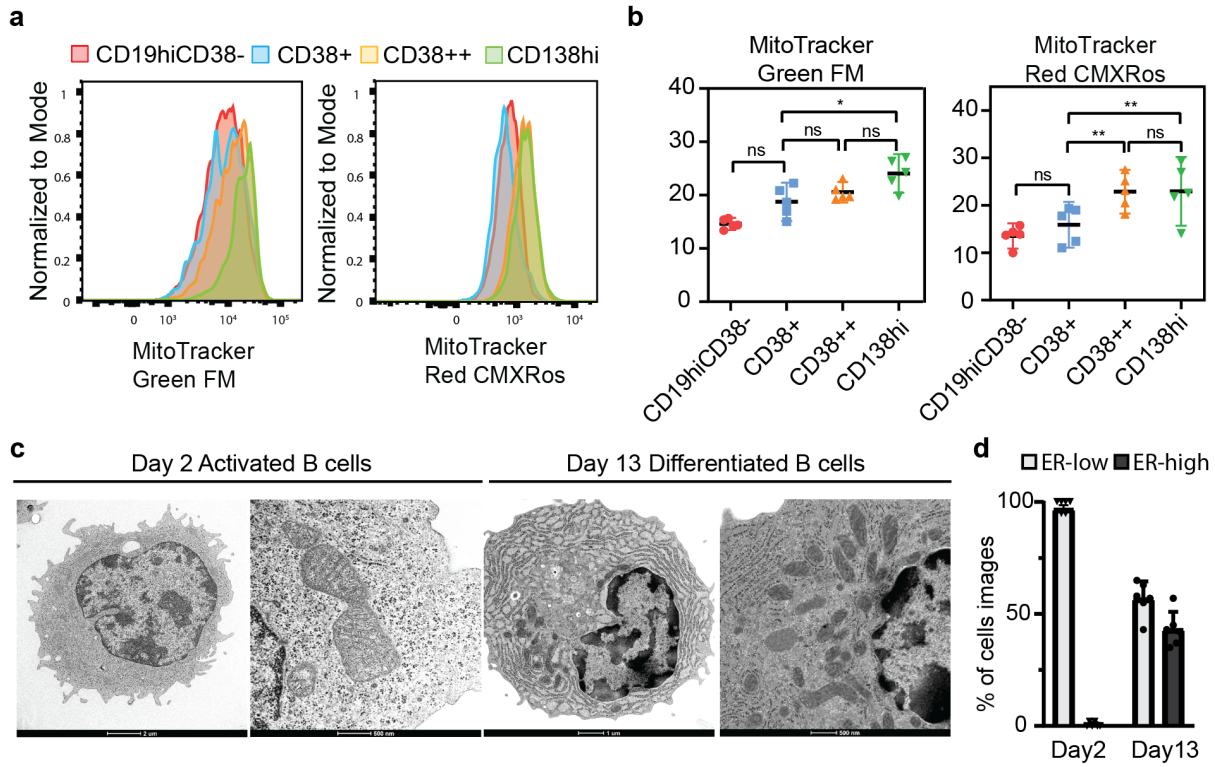

(**a, b**) Using the indicated protein markers: active B ($CD19^{hi}CD38^{-}$), $CD38^{+}$, $CD38^{++}$, and $CD138^{hi}$ flow cytometry showing expression of MitoTracker Green FM (mitochondrial volume) and MitoTracker Red CMXRos (mitochondrial stress) from different B cell subsets. The data (n=5 subjects) are normalized by minimal and maximal intensity per replicate and presented as mean and 95% confidence intervals. To assess significance, we used a paired one-way ANOVA with Tukey's multiple comparison test (* $p < 0.05$, ** $p < 0.01$, *** $p < 0.001$). P-values for $CD38^{+}$ and $CD138^{hi}$ with MitoTracker Green FM is 0.0123, for $CD38^{+}$ and $CD38^{++}$, $CD38^{+}$ and $CD138^{hi}$ with MitoTracker Red CMXRos are 0.0044 and 0.0041, respectively. Source data are provided as a Source Data file. (**c**) Transmission electron microscopy of day 2 and day 13 B cells from three-stage culture. (**d**) Quantification of rough endoplasmic reticulum (RER) in *ex vivo*

differentiated cultures. day 2 (43 images) and day 13 cells (60 images) were scored blindly for having prominent RER or not (n=6 participants).

2.5.3. *Ex vivo differentiated PCs home to BM and CD138+ PC is the main population engrafted.*

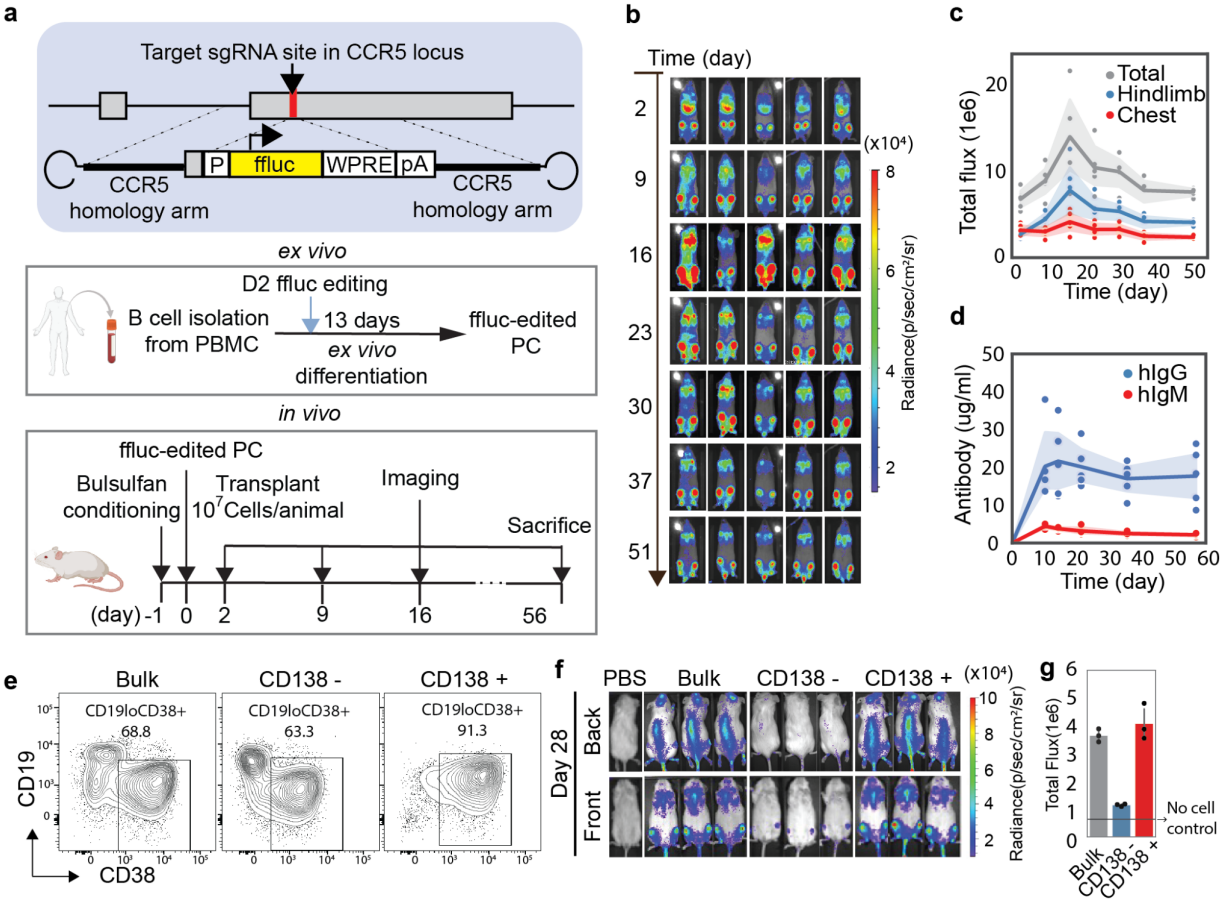

(a) Schematic of firefly luciferase showing the homology-directed repair strategy, the B cell engineering and differentiation strategy and the *in vivo* engraftment and tracking strategy. It was partially created with BioRender.com. **(b)** Representative images from an *in vivo* engraftment experiment tracking engineered B cells from Day 0 to day 51 using firefly luciferase imaging by IVIS (n=10 animals, 2 independent donors. The imaging data is representative from a single donor; the data from donor 2 is in Supplementary Fig. 3a-b). **(c)** Luciferase flux was quantified in the hindlimb and chest at each of the time points. **(d)** hIgG was quantified in serum by ELISA. **(c, d)** The line indicates the mean at each time point, and the shadow shows the 95% confidence intervals. Source data are provided as a Source Data file. **(e)** Flow cytometry of cell subsets after

enrichment with CD138 antibody. (**f)** Representative images and **(g)** quantification from *in vivo* subset engraftment tracking engineered B cells after a month. Cells were edited to express firefly luciferase and were imaged by IVIS (n=3 animals). Data are presented as mean +/- SD.

2.5.4. *Ex vivo* differentiated PCs home to BM and secrete hIgG for up to 1 year.

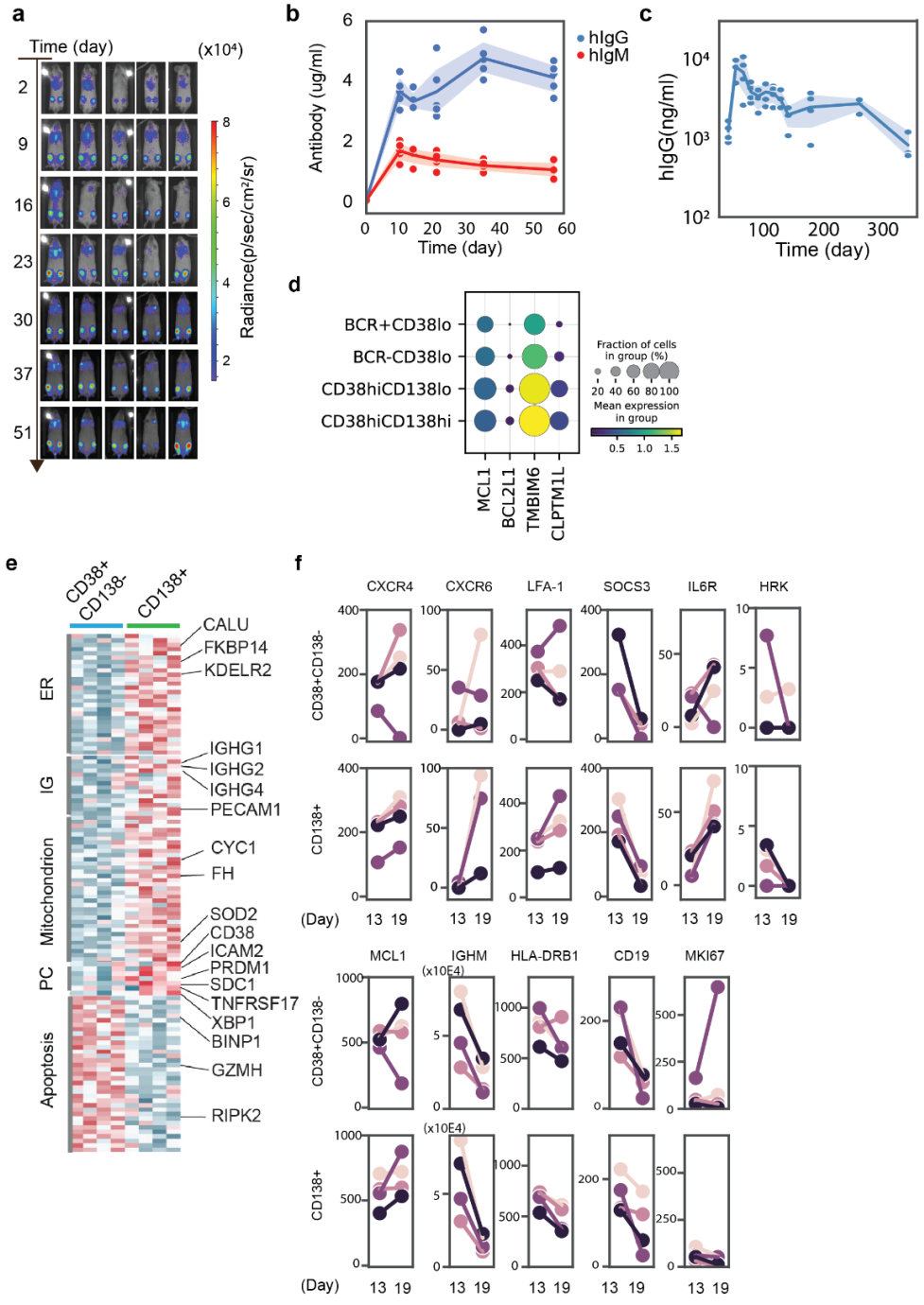

(a) Firefly luciferase gene was introduced by the HDR strategy into B cell *CCR5* locus at day 2 of three-stage culture, and *in vivo* engraftment tracking engineered B cells from Day 0 to day 51 using

firefly luciferase imaging by IVIS (The imaging data is representative from a single donor; donor 2). **(b)** hIgG was quantified in serum from Day 0 to day 51 by ELISA (donor 2, n=5 animals). The line indicates the mean at each time point, and the shadow shows the 95% confidence intervals. Source data are provided as a Source Data file. **(c)** hIgG was quantified in serum by ELISA for up to 1-year post-transfer (n = 4 animals). The line indicates the mean at each time point, and the shadow shows the 95% confidence intervals. **(d)** Dotplot visualization of day 13 B cells ($n = 2897$ cells) : subsets are listed on y-axis and genes are listed along the x-axis. Dot size represents percentage of cells in a group expressing each gene; dot color indicates mean expression level in a group. **(e)** A heatmap showing expression of representative genes from the RNA sequencing analysis from the CD138+ and CD38+CD138- fractions from 4 subjects (columns). **(f)** Gene counts from the indicated genes from the CD138+ and CD38+CD138- from 4 subjects at day 13 or day 19 in culture are presented (n = 4 subjects).

2.5.5. *hIL-6 and hBAFF promote engraftment of ex vivo differentiated PCs*

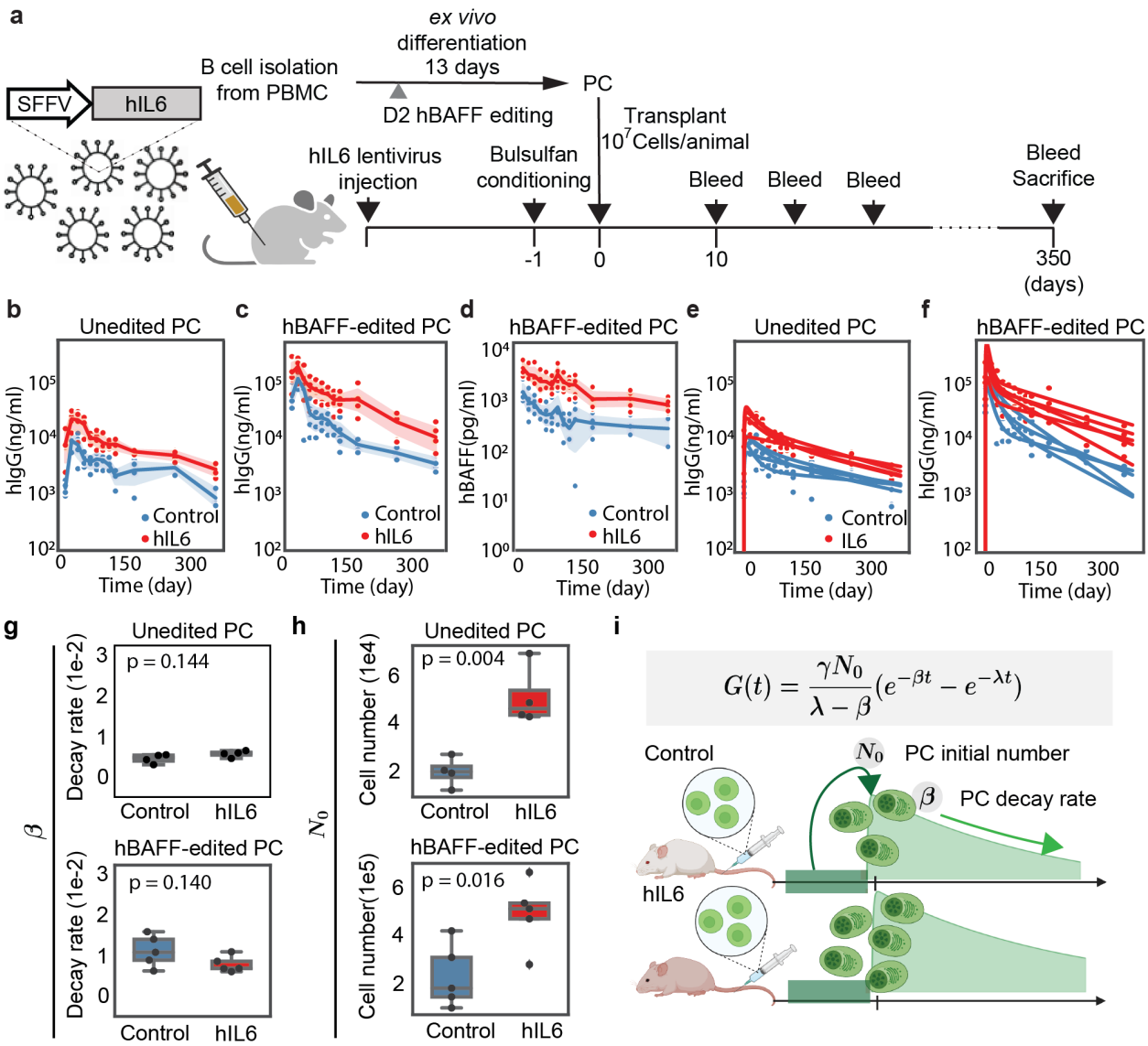

(a) Schematic describing *in vivo* infusion of *ex vivo* differentiated B cells. Mock (n=4 animals) or hBAFF (n=5 animals) edited cells were transferred into NSG mice engineered to express hIL-6 (hIL-6-NSG). It was partially created with BioRender.com. **(b-d)** ELISA was used to quantify B cell production of hIgG and hBAFF in NSG or NSG-hIL-6 animals. The line indicates the mean at each time point, and the shadow shows the 95% confidence intervals. Source data are provided

as a Source Data file. **(e, f)** Using antibody secretion rate and antibody degradation rate as parameters (Supplementary Table 2), we fitted curves to explain the observed hIgG dynamics in the indicated mouse models. **(g, h)** For each animal (Mock, n=4 animals; hBAFF, n=5 animals), we used the fitted curves to calculate decay rate and engrafted PC numbers. Box plot represents a central line denoting median value (50th percentile), while the box contains the 25th to 75th percentiles of the dataset with black whiskers marking the maximum (95th percentile) and minimum (5th percentile). P-values were calculated using an unpaired two-tailed Welch's t-test. **(i)** Schematic showing how the key parameters (initial engraftment number and decay rate) are altered by hIL-6. It was created with BioRender.com.

2.5.6. *PC protein secretion in hIL6-engineered mice and hBAFF-edited cells*

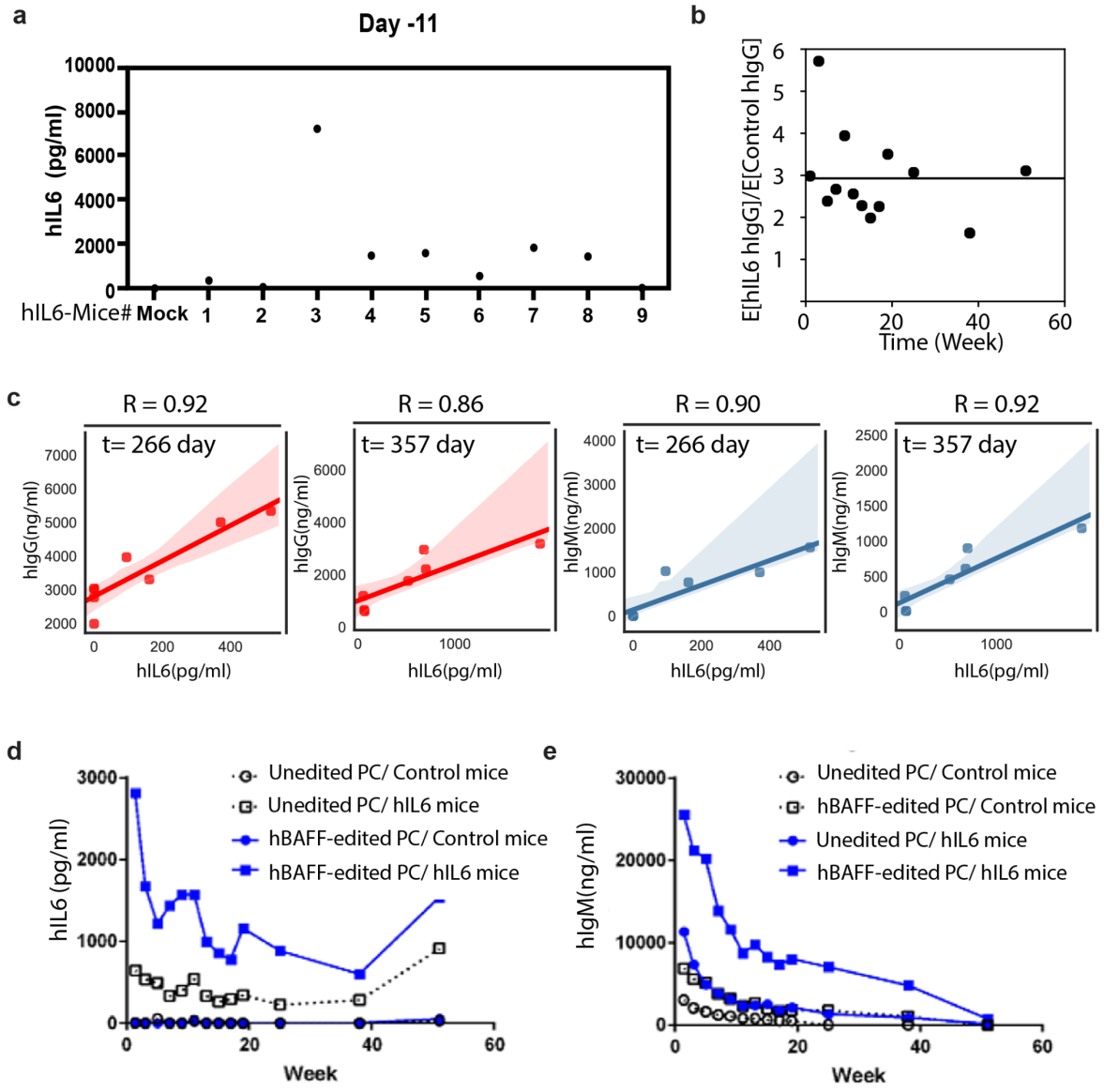

(a) hIL6 levels in hIL6-NSG mice serum before cell transplantation 11 days. Source data are provided as a Source Data file. **(b)** Ratio of the mean of hIgG in hIL6-NSG (n=5 animals) to that of NSG mice (n=4 animals). The horizontal line represents the mean of the fold change across all timepoints. **(c)** Pearson correlation between hIL6 and human antibodies in mice serum quantified

by ELISA at last two time points (t = 266 day and 357 day), each dot represents one animal (n=8 animals). **(d, e)** ELISA was used to quantify hIL6 in serum and B cell production of hIgM in NSG or NSG-hIL6 animals with unedited B cells and hBAFF-edited B cells. Data collected from unedited PC in control mice (n=4 animals), unedited PC in hIL6 mice (n=4 animals), hBAFF-edited PC in control mice (n=5 animals) and hBAFF-edited PC in hIL6 mice (n=5 animals).

2.5.7. *hBAFF increases the number of IgG ASCs.*

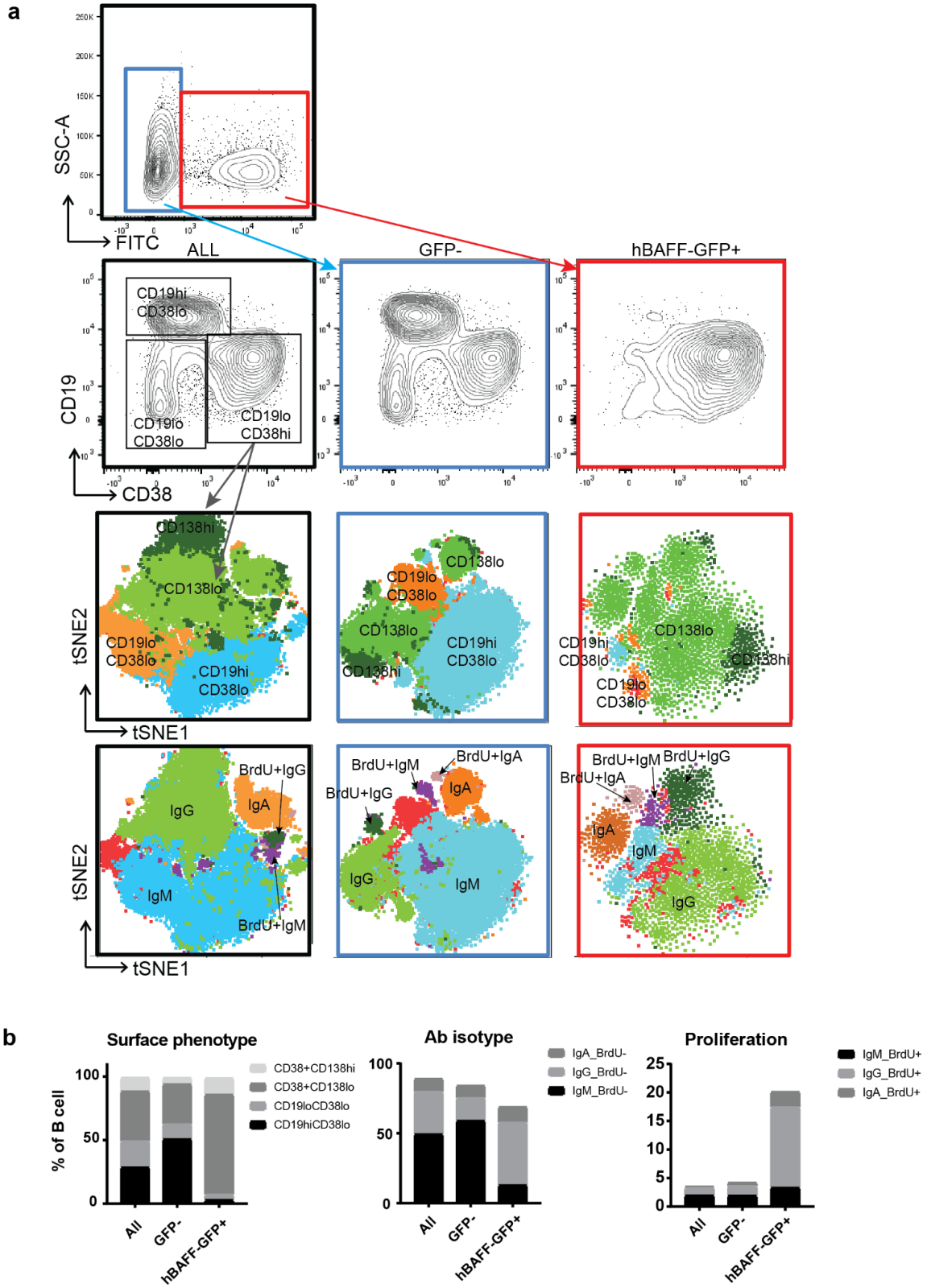

(a) Day 13 phenotype of hBAFF-edited B cells. Cells were stained with the indicated antibody markers. Cells were gated into GFP+ (hBAFF edited cells) and GFP- (unedited cells) and the marker expression was visualized using a tSNE plot. The color codes were indicated by the labels. **(b)** Stacked bar chart representing flow cytometry quantification of hBAFF-edited and unedited cells using the indicated antibodies.

2.5.8. *Model for longevity of engrafted PCs predicts dynamics in mice.*

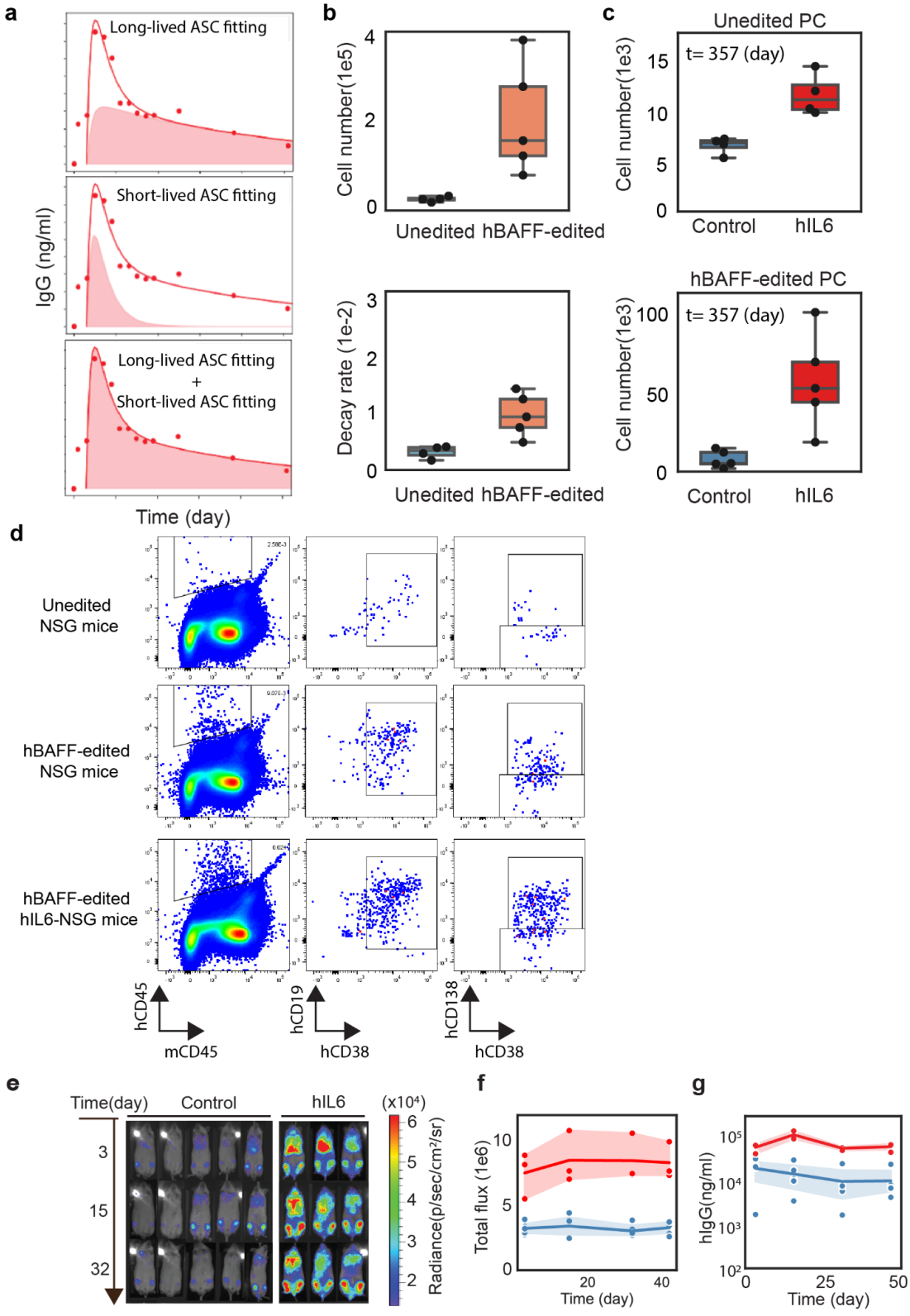

(a) Schematic of model fitting for hIgG dynamics in long and short-lived ASCs (model 1, Supplemental note). **(b)** Estimated engrafted cell number and decay rate by model 1 in NSG mice engrafted with unedited (n=4 animals) and hBAFF-edited cells (n=5 animals). **(c)** Long-lived PC cell numbers at the last time point as predicted by the model, equation 1 Supplemental note. **(b-c)** Box plot represents a central line denoting median value (50th percentile), while the box contains the 25th to 75th percentiles of the dataset with black whiskers marking the maximum (95th percentile) and minimum (5th percentile). **(d)** Flow cytometry showing the distribution of the indicated surface markers in cells collected from the BM in transfer experiments using unedited and hBAFF-edited cells collected in NSG or hIL6 NSG mice. **(e-f)** PCs engineered to express firefly luciferase were transferred into NSG (n=5 animals) and hIL6-NSG (n=3 animals) mice. The mice were imaged **(e)**, luciferase was quantified **(f)** and IgG levels were quantified **(g)** The shadows represent 95% confidence intervals and lines represent mean.

2.5.9. *Transfer of PCs into an immunodeficient mouse model expressing hIL-6 improves PCs engraftment*

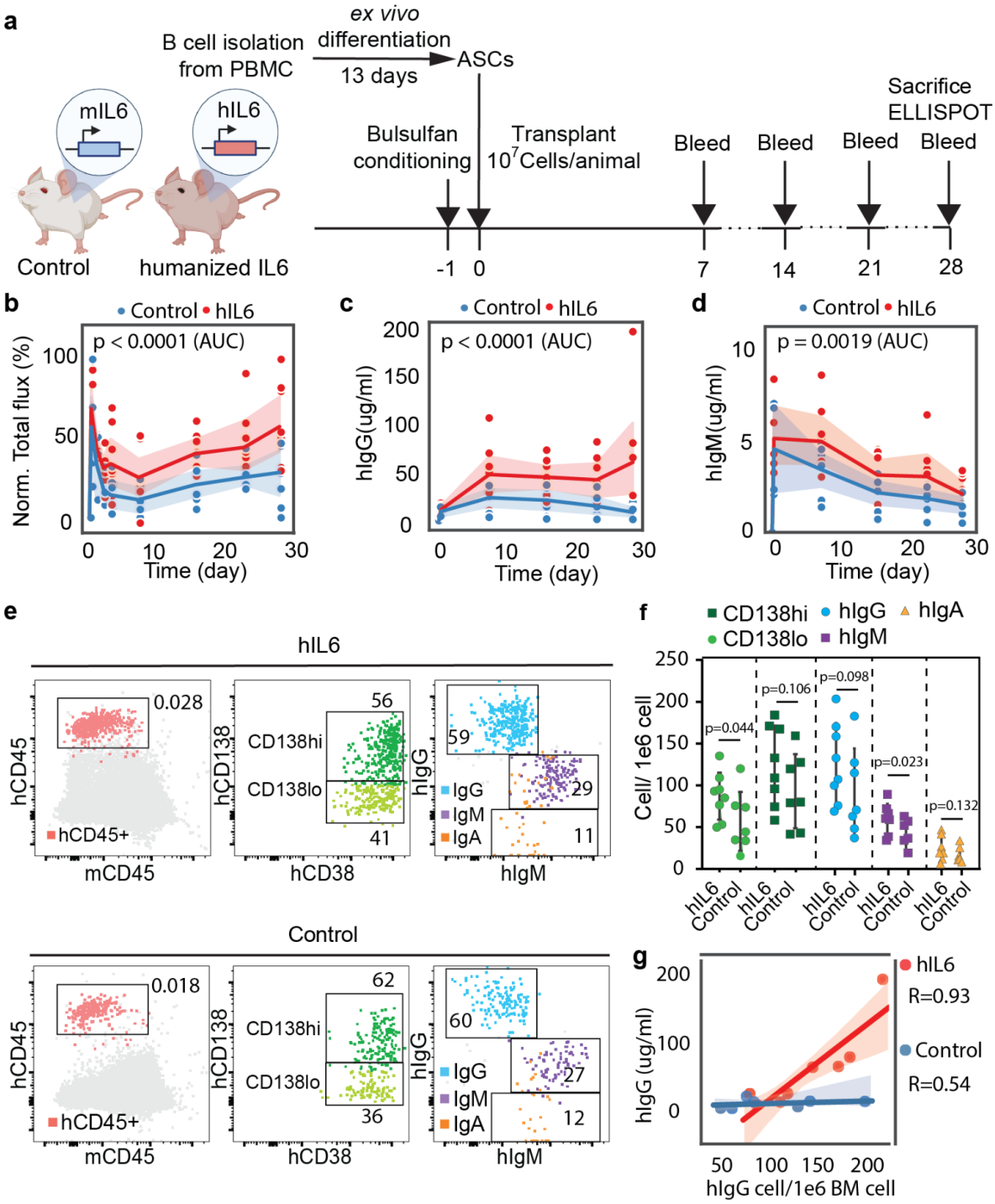

(a) Schematic describing transfer of *ex vivo* derived PCs into B-NDG (control; n=7 animals from 2 independent experiments) and hIL-6-B-NDG knock-in (hIL-6; n=8 animals from 2 independent experiments) mice. It was partially created with BioRender.com. **(b-d)** Firefly luciferase was quantified by IVIS imaging (normalized by Min-max normalization), hIgG and hIgM were quantified by ELISA and each point was plotted individually. The shadow represents the 95% confidence interval and line represents the mean. P-values were calculated in a two-sided t-test by comparing area under curve (AUC) from individual mice. P-values for normalized flux AUC and IgG AUC are 1.46E-05 and 1.37E-05, respectively. Source data are provided as a Source Data file. **(e, f)** Representative **e** and quantified **f** Flow cytometry of BM cells from sacrificed mice using the indicated antibodies (control; n=7 animals from 2 independent experiments) and hIL-6-B-NDG knock-in (hIL-6; n=8 animals from 2 independent experiments). Data are presented as mean +/- SD. Source data are provided as a Source Data file. **(g)** The relationship between hIgG antibody concentration and hIgG PCs counts in B-NDG mice and hIL-6-B-NDG mice. The correlation between them is presented by Pearson correlation coefficient based on their quasi-linear relationship and assumption of normality of variables. The line indicates the mean at each time point, and the shadow shows the 95% confidence intervals.

2.5.10. *hIL-6 prevents CD38^{hi}CD138^{lo} PC apoptosis and increases hIgG secretion rate*

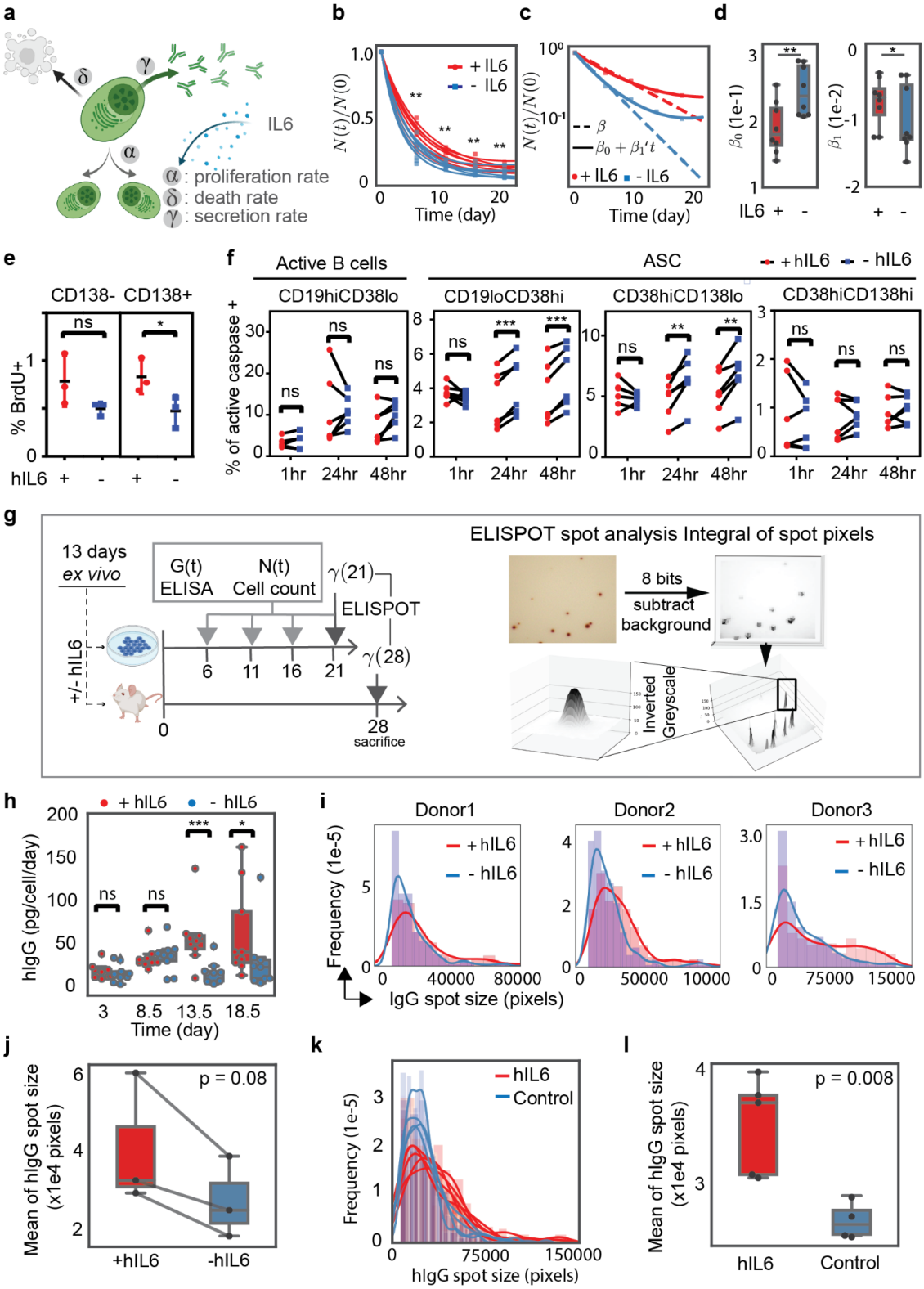

(a) Schematic showing possible PC features affected by hIL-6 including proliferation rate (α), death rate (δ), and antibody secretion rate (γ). (**b)** Following *ex vivo* differentiation of PCs, CD138+ cells were isolated and cultured for 20 days in the presence or absence of hIL-6. The cell number for each replicate (n=8; 4 independent donors) was plotted and curves were fitted (red and blue lines) based on the primary cell counting data. A two-sided paired t-test is performed for each timepoint, significance is under a significance level of $\alpha = 0.05$. (* $p < 0.05$, ** $p < 0.01$, *** $p < 0.001$). P-values from left to right are 0.001, 0.007, 0.004, and 0.006, respectively. Source data are provided as a Source Data file. (**c)** Representative fitted curves with constant decay rate () and time dependent decay rate (), respectively. (**d)** Fitted results of and from independent experiments (n=8; 4 donors). Box plot represents a central line denoting median value (50th percentile), while the box contains the 25th to 75th percentiles of the dataset with black whiskers marking the maximum (95th percentile) and minimum (5th percentile). P-values were calculated by a two-sided paired t-test. A two-sided paired t-test is performed, significance is under a significance level of $\alpha = 0.05$. (* $p < 0.05$, ** $p < 0.01$, *** $p < 0.001$). P-value for and are 0.0027 and 0.03, respectively. (**e)** *Ex vivo* differentiated PCs were labeled with BrdU at day 16 for 72 hours and analyzed by flow cytometry at day 19 (n=3 donors). A two-sided paired t-test is performed, significance is under a significance level of $\alpha = 0.05$. (* $p < 0.05$, ** $p < 0.01$, *** $p < 0.001$). Data are presented as mean +/- SD. Source data are provided as a Source Data file. **(f)** *Ex vivo* differentiated PCs were incubated with or without hIL-6 for the indicated time periods and flow cytometry was used to quantify Caspglow in the indicated phenotypic subsets (n=6 donors). P-values were elucidated by a two-sided paired t-test (* $p<0.05$; ** $p<0.01$, and ** $p<0.001$). **(g)** Schematic describing experimental outline for quantification of PC antibody secretion capacity *ex vivo* and *in vivo.* **(h)** hIgG secretion

calculated from ELISA and cell counts (pg/cell/day) from day 0 to day 21 after three-stage culture (n=9; 5 donors). P-values were calculated using a two-sided paired t-test, significance is under a significance level of $\alpha = 0.05$ (* $p<0.05$; ** $p<0.01$, and ** $p<0.001$). P-values from left to right are 0.61, 0.70, 0.0007, and 0.015, respectively. Source data are provided as a Source Data file. **(i)** Histogram and kernel density estimate (solid line) distributions of ELISPOT size from *ex vivo* day 13 CD138+ cells cultured with or without hIL-6 for 21 days. Data was normalized by scaling input vectors individually to unit norm. Source data are provided as a Source Data file. **(j)** Mean of ELISPOT spot in 3-dimensional size from *ex vivo* differentiated PCs cultured for 21 days (n=3 donors). P-values were calculated using a two-sided paired t-test. **(k)** Histogram and kernel density estimate (solid line) distributions of ELISPOT size converted from 3-dimensional pixels, quantified from ASCs from B-NDG mice (n= 4 animals) and hIL-6-B-NDG mice (n= 5 animals) at day 28. Data normalized by scaling input vectors individually to unit norm. Source data are provided as a Source Data file. **(l)** Mean of ELISPOT spot in 3-dimensional size from ASCs from B-NDG mice and hIL-6-B-NDG mice at day 28. P-values were calculated using a two-sided t-test. **(h, j, l)** Box plot represents a central line denoting median value (50th percentile), while the box contains the 25th to 75th percentiles of the dataset with black whiskers marking the maximum (95th percentile) and minimum (5th percentile). **(a, g)** were created with BioRender.com.

2.5.11. *hIL6 decreases the decay rate dynamics of CD138+ cells ex vivo*

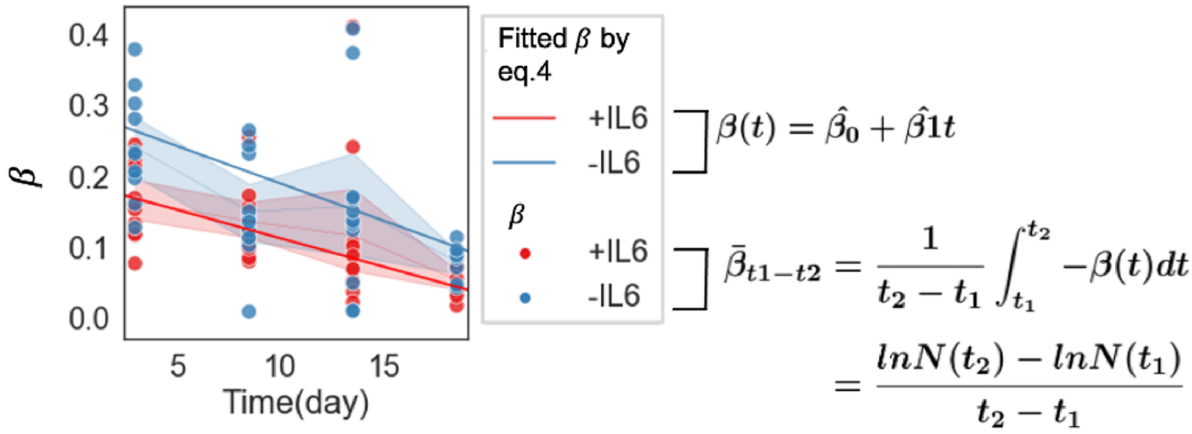

Decay rate of *ex vivo* day 13 CD138+ cells cultured with or without hIL6 for 21 days. Individual decay rates at the indicated time points are represented by dots, and the solid line represents the average decay rate as a function of time. β is fitted by eq.4 in model 2, based on CD138+ cell number dynamics. The line (dim) indicates the mean at each time point, and the shadow shows the 95% confidence intervals.

2.5.12. *Remodeling of long-term in vivo experiments*

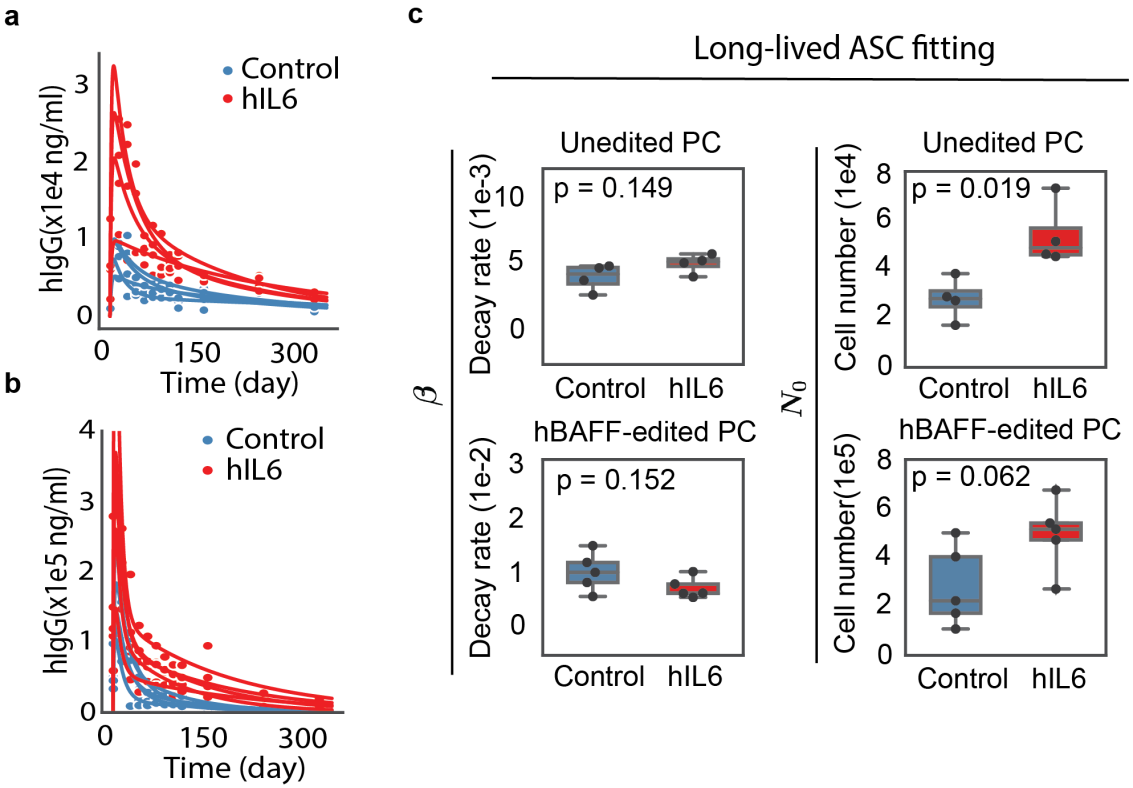

Histogram and kernel density estimate (solid line) distributions of ELISPOT size from *ex vivo* day 13 CD138+ cells cultured with or without hIL6 for 21 days. Data was normalized by scaling input vectors individually to unit norm.

2.6. TABLES

2.6.1. *Antibodies and kits*

Experiment	Item	Vendor	Catalog	Dilution fold
Flow cytometry	PE-Cy7 anti-human CD19	Biolegend	302216	200X
	PerCP-Cy5.5 anti-human CD38	BD	BDB551400	200X
	PE anti-human CD138	Biolegend	356504	100X
	PacBlue anti-human IgM	Biolegend	314514	300X
	APC anti-human IgM	BD	551062	300X
	APC-Vio® 770 IgA Antibody, anti-human	Miltenyi	130-113-473	200X
	AF700 anti-human IgG	BD	561296	200X
	PE-Cy7 Mouse Anti-Human CD45	BD	557748	200X
	Brilliant Violet 421 Anti-Human CD45	BD	563879	200X
	Brilliant Violet 605 anti-mouse CD45	Biolegend	103140	200X
	Brilliant Violet 510 anti-human CD19	Biolegend	302242	200X
	FITC anti-BrdU	BD	347583	50X
CITESEQ	TotalSeq™-B0251 anti-human Hashtag 1 Antibody	Biolegend	394631	1000X
	TotalSeq™-B0251 anti-human Hashtag 2 Antibody	Biolegend	394633	1000X
	TotalSeq™-B0251 anti-human Hashtag 3 Antibody	Biolegend	394635	1000X
	TotalSeq™-B0251 anti-human Hashtag 4 Antibody	Biolegend	394637	1000X
	TotalSeq™-B0136 anti-human IgM Antibody	Biolegend	314549	200X

	TotalSeq™-B0389 anti-human CD38 Antibody	Biolegend	303547	800X
	TotalSeq™-B0055 anti-human CD138 (Syndecan-1) Antibody	Biolegend	356543	100X
ELISPOT	Goat Anti-Human IgG-HRP	Southern Biotech	2040-05	1000X
	Anti-human IgG	ThermoFisher	A18813	250X
	AEC Substrate Kit, Peroxidase (HRP), (3-amino-9-ethylcarbazole)	Vector Laboratories	SK4200	
ELISA	Invitrogen™ IgG (Total) Human Uncoated ELISA Kit	Invitrogen	50-112-8849	
	Invitrogen™ IgM (Total) Human Uncoated ELISA Kit	Invitrogen	50-112-8719	
	ELISA MAX™ Deluxe Set Human IL-6	Biolegend	430504	
	Human BAFF/BLyS/TNFSF13B DuoSet ELISA	R&D	DY124-05	

2.6.2. *Parameters used in fitting equation 2.*

	Antibody secretion rate / volume of displacement	Antibody degradation rate	IgG	PCs decay rate	PC Initial number
	$\gamma(ng \cdot cell^{-1} \cdot day^{-1})$ / 2 ml	$\alpha\ (day^{-1})$	$G\ (ng/ml)$	$\beta\ (day^{-1})$	$N_0(cell)$
Mock	0.1 (adjusted: 0.75)	0.495	Experimental data	fitting	fitting
hIL6	0.1	0.495	Experimental data	fitting	fitting

2.7. BIBLIOGRAPHY

24. Cheng, R. Y.-H. *et al.* Ex vivo engineered human plasma cells exhibit robust protein secretion and long-term engraftment in vivo. *Nat. Commun.* **13**, 1–14 (2022).
25. Manz, R. A. *et al.* Humoral immunity and long-lived plasma cells. *Curr. Opin. Immunol.* **14**, 517–521 (2002).
26. Slifka, M. K., Antia, R., Whitmire, J. K. & Ahmed, R. Humoral immunity due to long-lived plasma cells. *Immunity* **8**, 363–372 (1998).
27. van Dam, M. *et al.* Structure-function analysis of interleukin-6 utilizing human/murine chimeric molecules. Involvement of two separate domains in receptor binding. *J. Biol. Chem.* **268**, 15285–15290 (1993).
28. Lacroix, M. *et al.* Novel Insights into Interleukin 6 (IL-6) Cis- and Trans-signaling Pathways by Differentially Manipulating the Assembly of the IL-6 Signaling Complex. *J. Biol. Chem.* **290**, 26943–26953 (2015).
29. Bernstein, N. J. *et al.* Solo: Doublet Identification in Single-Cell RNA-Seq via Semi-Supervised Deep Learning. *Cell Syst* **11**, 95–101.e5 (2020).
30. Wolf, F. A., Angerer, P. & Theis, F. J. SCANPY: large-scale single-cell gene expression data analysis. *Genome Biol.* **19**, 15 (2018).
31. Bolger, A. M., Lohse, M. & Usadel, B. Trimmomatic: a flexible trimmer for Illumina sequence data. *Bioinformatics* **30**, 2114–2120 (2014).
32. Dobin, A. *et al.* STAR: ultrafast universal RNA-seq aligner. *Bioinformatics* **29**, 15–21 (2013).
33. Love, M. I., Huber, W. & Anders, S. Moderated estimation of fold change and dispersion for RNA-seq data with DESeq2. *Genome Biol.* **15**, 550 (2014).
34. Huang, D. W., Sherman, B. T. & Lempicki, R. A. Systematic and integrative analysis of large gene lists using DAVID bioinformatics resources. *Nat. Protoc.* **4**, 44–57 (2009).
35. Huang, D. W., Sherman, B. T. & Lempicki, R. A. Bioinformatics enrichment tools: paths toward the

comprehensive functional analysis of large gene lists. *Nucleic Acids Res.* **37**, 1–13 (2009).

36. Bromage, E., Stephens, R. & Hassoun, L. The third dimension of ELISPOTs: quantifying antibody secretion from individual plasma cells. *J. Immunol. Methods* **346**, 75–79 (2009).
37. Waskom, M. seaborn: statistical data visualization. *J. Open Source Softw.* **6**, 3021 (2021).
38. Hunter. Matplotlib: A 2D Graphics Environment. **9**, 90–95 (2007).
39. Haghverdi, Büttner, Wolf, Buettner & Theis. Diffusion pseudotime 411 robustly reconstructs branching cellular lineages. *Nat. Methods*.
40. Wolf, F. A. *et al.* PAGA: graph abstraction reconciles clustering with trajectory inference through a topology preserving map of single cells. *Genome Biol.* **20**, 59 (2019).
41. Cocco, M. *et al.* In vitro generation of long-lived human plasma cells. *J. Immunol.* **189**, 5773–5785 (2012).
42. Garimalla, S. *et al.* Differential transcriptome and development of human peripheral plasma cell subsets. *JCI Insight* **4**, (2019).
43. Sandoval, H., Kodali, S. & Wang, J. Regulation of B cell fate, survival, and function by mitochondria and autophagy. *Mitochondrion* **41**, 58–65 (2018).
44. Martinez-Martin, N. *et al.* A switch from canonical to noncanonical autophagy shapes B cell responses. *Science* **355**, 641–647 (2017).
45. Lam, W. Y. *et al.* Mitochondrial Pyruvate Import Promotes Long-Term Survival of Antibody-Secreting Plasma Cells. *Immunity* **45**, 60–73 (2016).
46. Hackenbrock, C. R. Ultrastructural bases for metabolically linked mechanical activity in mitochondria. I. Reversible ultrastructural changes with change in metabolic steady state in isolated liver mitochondria. *J. Cell Biol.* **30**, 269–297 (1966).
47. Sanjuan Nandin, I. *et al.* Novel in vitro booster vaccination to rapidly generate antigen-specific human monoclonal antibodies. *J. Exp. Med.* **214**, 2471–2490 (2017).
48. Nakayama, T. *et al.* Cutting edge: profile of chemokine receptor expression on human plasma cells

accounts for their efficient recruitment to target tissues. *J. Immunol.* **170**, 1136–1140 (2003).

49. Babon, J. J., Varghese, L. N. & Nicola, N. A. Inhibition of IL-6 family cytokines by SOCS3. *Semin. Immunol.* **26**, 13–19 (2014).
50. Coulie, P. G., Stevens, M. & Van Snick, J. High- and low-affinity receptors for murine interleukin 6. Distinct distribution on B and T cells. *Eur. J. Immunol.* **19**, 2107–2114 (1989).
51. Mackay, F. & Browning, J. L. BAFF: a fundamental survival factor for B cells. *Nat. Rev. Immunol.* **2**, 465–475 (2002).
52. Zhang, X. *et al.* BAFF supports human B cell differentiation in the lymphoid follicles through distinct receptors. *Int. Immunol.* **17**, 779–788 (2005).
53. Li, F. *et al.* Mouse Strains Influence Clearance and Efficacy of Antibody and Antibody–Drug Conjugate Via Fc–FcγR Interaction. *Mol. Cancer Ther.* **18**, 780–787 (2019).
54. Ghetie, V., Ward, E. S. & Vitetta, E. S. Pharmacokinetics of Antibodies and Immunotoxins in Mice and Humans. in *Handbook of Anticancer Pharmacokinetics and Pharmacodynamics* (eds. Figg, W. D. & McLeod, H. L.) 475–498 (Humana Press, 2004).
55. Salmon, S. E. & Smith, B. A. Immunoglobulin synthesis and total body tumor cell number in IgG multiple myeloma. *J. Clin. Invest.* **49**, 1114–1121 (1970).
56. Avery, D. T. *et al.* BAFF selectively enhances the survival of plasmablasts generated from human memory B cells. *J. Clin. Invest.* **112**, 286–297 (2003).
57. Schneider, P. *et al.* BAFF, a novel ligand of the tumor necrosis factor family, stimulates B cell growth. *J. Exp. Med.* **189**, 1747–1756 (1999).
58. Fisher, R. A. *The genetical theory of natural selection*. (Рипол Классик).
59. Odendahl, M. *et al.* Generation of migratory antigen-specific plasma blasts and mobilization of resident plasma cells in a secondary immune response. *Blood* **105**, 1614–1621 (2005).
60. Hammarlund, E. *et al.* Plasma cell survival in the absence of B cell memory. *Nat. Commun.* **8**, 1781 (2017).

61. Amanna, I. J., Carlson, N. E. & Slifka, M. K. Duration of humoral immunity to common viral and vaccine antigens. *N. Engl. J. Med.* **357**, 1903–1915 (2007).

62. Lapidot, T. Mechanism of human stem cell migration and repopulation of NOD/SCID and B2mnull NOD/SCID mice. *Ann. N. Y. Acad. Sci.* **938**, 83–95 (2006).

63. Chatterjee, S., Behnam Azad, B. & Nimmagadda, S. The intricate role of CXCR4 in cancer. *Adv. Cancer Res.* **124**, 31–82 (2014).

64. Núñez, D. *et al.* A Functional Analysis on the Interspecies Interaction between Mouse LFA-1 and Human Intercellular Adhesion Molecule-1 at the Cell Level. *Frontiers in Immunology* vol. 8 Preprint at https://doi.org/10.3389/fimmu.2017.01817 (2017).

65. Lang, J. *et al.* Replacing mouse BAFF with human BAFF does not improve B-cell maturation in hematopoietic humanized mice. *Blood Adv* **1**, 2729–2741 (2017).

66. Yu, H. *et al.* A novel humanized mouse model with significant improvement of class-switched, antigen-specific antibody production. *Blood* **129**, 959–969 (2017).

67. Jourdan, M. *et al.* IL-6 supports the generation of human long-lived plasma cells in combination with either APRIL or stromal cell-soluble factors. *Leukemia* **28**, 1647–1656 (2014).

68. Cassese, G. *et al.* Plasma cell survival is mediated by synergistic effects of cytokines and adhesion-dependent signals. *J. Immunol.* **171**, 1684–1690 (2003).

69. Mesin, L., Di Niro, R., Thompson, K. M., Lundin, K. E. A. & Sollid, L. M. Long-lived plasma cells from human small intestine biopsies secrete immunoglobulins for many weeks in vitro. *J. Immunol.* **187**, 2867–2874 (2011).

70. Brynjolfsson, S. F., Mohaddes, M., Kärrholm, J. & Wick, M.-J. Long-lived plasma cells in human bone marrow can be either CD19+ or CD19. *Blood Adv* **1**, 835–838 (2017).

Chapter 3.

SEC-SEQ: ASSOCIATION OF MOLECULAR SIGNATURES WITH ANTIBODY SECRETION IN THOUSANDS OF SINGLE HUMAN PLASMA CELLS

This work has been preprinted in: Cheng, R. Y.-H. *et al.* SEC-seq: Association of molecular signatures with antibody secretion in thousands of single human plasma cells. *bioRxiv* 2022.08.25.505190 (2022) doi:10.1101/2022.08.25.505190.

3.1. INTRODUCTION

Organisms critically depend on the proteins or other factors which cells secrete into their environment that can act locally in a paracrine manner or systemically. For example, one of the main roles of B cells is to respond to antigens with the production and secretion of large quantities of immunoglobulins targeting antigen epitopes. In this process, antibody-secreting B cells differentiate, undergoing significant phenotypic, morphological, and genetic changes. Linking these functional changes in the capacity for secretion of immunoglobulins to genetic/phenotypic profiles at the single-cell level can uncover the population heterogeneity and potential new cell states.

We demonstrate a technology that overcomes these tradeoffs, combining the multiplexing and high-throughput quantitative analysis of surface markers by flow cytometry or transcripts by single-cell RNA-seq with the ability to quantify secretions (IgG) in the same single cells. The approach uses microscale hydrogel particles with a bowl-shaped cavity, called nanovials[72], which capture cells and their secretions and are compatible with flow cytometry and single-cell sequencing instruments. To study secretions of antibody-secreting cells, we apply this technology to achieve an 8-plex multiplexed secretion assay, including 6 channels dedicated to cell surface markers, 1 channel to cell viability, and a final channel to IgG secretion. The approach was compatible with fluorescence activated cell sorting (FACS) using the Nanocellect WOLF and imaging flow cytometry using the Amnis ImageStream$^{®X}$. By using oligonucleotide-barcoded antibodies, we could also link IgG secretion directly to transcriptomes in the same cells by introducing nanovials containing antibody secreting cells directly through a 10X Chromium single-cell RNA-seq workflow. This new method, SEC-seq has enabled us to learn several things

about the biology of antibody-secreting B cells and showed that transcripts involved in antibody production/metabolism rather than the antibody itself, were most highly associated with high secretion. We envision that this method could help us better understand the determinants of protein secretion in human antibody-secreting cells and other models, and better engineer secretory function, unlocking new therapeutic modalities.

3.2. MATERIAL AND METHODS

3.2.1. *Cell culture methods*

All cells were cultured in incubators at 37°C and 5% CO2 in static conditions unless otherwise noted.

Human primary B cells. We isolated B cells from healthy donors' peripheral blood mononuclear cells (Fred Hutchinson Cancer Research Center) using the EasySep Human B cell isolation kit (Stem Cell Technologies). Isolated B cells were cultured in Iscove's modified Dulbecco's medium (Gibco) supplemented with 2-mercaptoethanol (55 mM) and 10% FBS. Cells were cultured for seven days (activation) in medium containing 100 ng/mL megaCD40L (Enzo Life Science), 1 mg/ml CpG ODN2006 (invitrogen), 40 ng/mL IL-21 (Peprotech), and then for three to five days (plasmablast/plasma cell differentiation) in medium containing 50 ng/mL IL-6 (Peprotech),10 ng/mL IL-15 and 15 ng/mL interferon-2B (Sigma-Aldrich).

Hybridoma cells. HyHel-5 cells were maintained in IMDM media (Invitrogen 12440053) supplemented with 10% FBS (Invitrogen 16000044) and 1% penicillin/streptomycin (Invitrogen). Cells were passaged down to a final concentration of $2x10^5$ cells/mL every three days.

Raji cells. Cells were sourced from ATCC (CCL-86^{TM}) and maintained in RPMI-1640 ATCC modification media (Invitrogen A1049101) supplemented with 10% FBS (Invitrogen) and 1% penicillin/streptomycin (Invitrogen). Cells were passaged down to a final concentration of $2x10^5$ cells/mL every three days.

3.2.2. *Methods of coating nanovials*

Nanovials were coated with streptavidin by mixing equal volumes of streptavidin (300 g/mL) and nanovials (n=340,000) for 15 mins at room temperature followed by three washes which consisted of resuspension in clean washing buffer (supplementary Table S1) and centrifugation at 400 x g. The coating antibody mix was prepared by making a 10X dilution of biotinylated anti-IgG (0.5 mg/mL) and biotinylated anti-cell surface protein (anti-CD27 or anti-CD45) (0.5 mg/mL) in washing buffer (final antibody concentration 0.05 mg/mL per antibody). Equal volumes of the coating antibody mix, and the streptavidin coated nanovials were combined and placed at room temperature for 30 minutes or 4°C overnight. Antibody coated nanovials were washed twice in washing buffer. After the final wash, the supernatant was removed and the nanovials were resuspended in cell media. The final prepared nanovials were placed on ice until cell loading.

3.2.3. *Methods of cell loading in nanovials*

Differentiated human B cells were first processed by ficoll density gradient centrifugation to remove dead cells and debris. For secretion experiments, 5 mL of blocking antibody (anti-IgG, Southern Biotech) was added to the 50 mL cell solution to yield a final concentration of 25 mg/mL. Then 55 mL of the cell solution (244,000 cells) was mixed with 20 mL of concentrated nanovials

(n= 340,000) at a ratio of 1:1.4 (cell: nanovial) on ice by pipetting for 30 seconds with a circular motion. Cells were loaded into nanovials by carefully pipetting throughout the pellet of nanovials. We then added 1 mL of biotin-free medium and incubated the mixed cells and nanovials on ice for 1 hour without any perturbation.

3.2.4. *Methods of incubation of cells with nanovials*

After the 1 hour loading process, samples were placed on top of the strainer and washed by 1 mL wash buffer two times. A 15 mL falcon tube was precoated with washing buffer, and used for cell collection by inverting the strainer and placing on top of the tube. 2 mL of washing buffer was used to wash the nanovials off the strainer and into the falcon tube. We then centrifuged the 15 mL falcon tube containing the filtered nanovials at 300 x g at 4°C for 5 min, and resuspended nanovials into B cell medium pre-warmed to 37°C. The falcon tubes containing nanovials in media were then incubated at 37°C on a rotator for gentle agitation (10 rpm) for 30 minutes to accumulate secretions on nanovials.

3.2.5. *Methods of cell staining of surface markers and secreted IgG*

FACS tubes were precoated with staining buffer (supplementary Table S1). After incubation to capture secretions, nanovial samples in falcon tubes were then centrifuged at 400 x g for 5 mins and resuspended into FACS tubes with a cocktail of antibodies (supplementary Table S2) to stain cell surface markers and secreted IgG in staining buffer. Samples were stained on ice for 20 minutes, then washed twice, before analysis by flow cytometry.

3.2.6. *Methods of flow cytometric analysis*

Flow cytometric analysis was performed on an LSR II flow cytometer (BD Biosciences) and events were analyzed using FlowJo software (BD). Flow cytometry gating for fluorescent proteins and viability, and immunophenotyping can be found in the supplement.

3.2.7. *Methods of imaging flow cytometric analysis*

An ISX 493 MKII equipped with a 405, 488, 560, 592, 642 and 785 nm lasers were used to interrogate B cell secretion capture on nanovials. 40000 objects were collected under 20x magnification with laser power and channel assignments as listed in Supplemental Tables S3 and S4.

Quantification of IgG signal on nanovials from cell secretions was performed through the gating strategy illustrated in Supplemental Figure S4. First, objects in focus were identified by the GradientRMS function in the brightfield channel. Single nanovial objects were separated from debris and multicellular aggregates based on an Aspect Ratio vs Area. Visual inspection of objects located in the gates drawn in S4B confirms correct placement of gate settings. CD38/CD138 double positive cells were further identified via the intensity feature on the CD38 and CD138 channel and separated into high and low signal populations. The amount of IgG secretion for these four populations was quantified by constructing a "nanovial mask" by subtracting the area localized to cells (CD38 or CD138) from the mask identified in the brightfield channel.

3.2.8. *Methods for visualizing nanovials through 10X Genomics Chip G*

Fluorinated oil with surfactant, gel bead solution and nanovial solutions were added into the reservoirs of the 10X Genomics Chip G. 3 mL syringes (Becton Dickinson) were connected to the bead and sample inlet reservoirs via PEEK tubing (IDEX) and a coupler molded out of PDMS. Syringe pumps (PhD 2000, Harvard Apparatus) were used to inject air into the reservoirs and pressurize the bead and sample inlets and drive flow. Droplet formation videos were recorded using an inverted microscope (Nikon TE300) equipped with a high-speed camera (ZWO ASI144MM).

3.2.9. *Mixed species SEC-seq validation experiment*

Barcoded nanovial preparation (Raji sample). Nanovials (4 million/mL) were modified by mixing a solution of nanovials in washing buffer with a cocktail of 40 mg/mL streptavidin and 20 mg/mL TotalSeqC conjugated streptavidin (Biolegend) solution at equal volumes. The sample was then placed on a rotator (speed) at room temperature for 30 minutes. Nanovials were washed three times by centrifuging the sample at 200 xg for 5 minutes, removing the supernatant, and resuspending in washing buffer. Following washing, the streptavidin modified nanovial solution was then mixed with a solution containing 8 μg/mL anti-human CD45 (Biolegend) at equal volume. The nanovials were then placed on a rotator at 4°C overnight. The nanovials were then washed three times as above and resuspended in cell media before proceeding with cell experiments.

Non-barcoded nanovial preparation (Hybridoma sample). Nanovials (4 million/mL) were modified by mixing with a solution of 60 mg/mL streptavidin at equal volume following standard procedures as described above. The streptavidin modified nanovial solution was then mixed with a solution containing an antibody cocktail comprising 8 mg/mL anti-mouse CD45 (R&D Systems)

biotinylated according to manufacturer instructions. (Thermo) and 20 mg/mL Goat anti-Mouse IgG FC (Jackson Immuno Research) at equal volume.

Raji and Hybridoma cells were loaded separately into nanovials on ice and incubated for 1 hour to allow binding. Background cells were removed using a 20 μm cell strainer and cells were then incubated in a CO2 incubator at 37°C for 30 min to accumulate secreted IgG. The hybridoma sample was stained with a 12 μg/mL solution of TotalSeqC conjugated anti IgG1 antibody (Biolegend) and incubated for 45 minutes on Ice. Samples were then washed three times with ultra-pure PBS containing 0.04% BSA (Invitrogen). The Raji and Hybridoma samples were mixed at a 1:1 ratio prior to proceeding with single-cell sequencing library preparation. Libraries were prepared at the UCLA sequencing core using the 10X Genomics Chromium Next GEM Single Cell 5' Kit v2 + Feature barcode libraries. Approximately 8000 nanovials were added in the sample lane and emulsified with barcoded beads with the Chromium instrument. Libraries were QC'd using the tapestation (Agilient) and sequenced using NovaSeq S2 (100 Cycles). FASTQ files were processed by cellranger and the Barnyard reference genome (refdata-gex-GRCh38-and-mm10-2020-A) was used for alignment. An additional custom reference genome was appeneded for alignment to identify transcripts for the known heavy and light chain sequences of the hybridoma cell line (HyHel-5). Data visualization and analyses was performed using Loupe Browser (v6.0) and Seurat.

3.2.10. *SEC-seq human ASCs sample preparation and sequencing*

Following *ex vivo* differentiation, cells were treated with Ficoll to remove any debris. Viable cells were immediately loaded onto nanovial and incubated to accumulate secretions, as described

above. After accumulating secretions on the nanovials, samples are stained with PE anti-IgG (BD), and a secondary antibody (anti-PE) that was labeled with barcoded oligonucleotides (Biolegend). Next, we sorted viable cells loaded on nanovials with the WOLF cell sorter (Nanocellect) by threshold on the negative SYTOX population (Figure S8). Sorted cell-loaded nanovials were introduced into the 10X Genomics Chip G (10X Genomics), at 2500-10000 cell-loaded nanovials per lane. Next, we prepared libraries using 10X Genomics Chromium Next GEM Single Cell v3.1 kit following the 10X user guide (CG000317). Libraries from the oligonucleotide barcoded antibodies bound to nanovials and transcripts were evaluated by tapestation (Agilent) before sequencing. Finally, libraries were pooled at a ratio of 80% cellular RNA to 20% oligonucleotide barcoded antibodies and sequenced with NextSeq 1000/2000 kit (Illumina) using the following read length: 28 bp Read1, 10 bp i7 Index, 10 bp i5 Index, and 90 bp Read2.

3.2.11. *Single Cell RNA-seq analysis*

FASTQ files were processed by cellranger based on the human reference genome GRCh38. The h5 file was then further analyzed using a custom python script. Data analysis including normalized, dimensional reduction, hierarchical clustering, leiden clustering and differential gene analysis were performed with scanpy[30].

3.2.12. *ELISpot (enzyme-linked immunospot)*

PBS pre-wetted 96 well plates (Millipore) were coated overnight at 4 °C with goat anti-human IgG (H + L) capture antibody (Jackson Immunoresearch). 100 mL of IMDM was used to block each well for 2 hours at 37°C. A designated number of cells were washed with PBS and resuspended in 2X cytokine cocktail in IMDM. We added 100 mLof cells to the elispot plate directly and incubated at 37°C in an incubator overnight. Cells were then washed away, and plates were washed

six times. Secreted IgG was detected by binding to HRP-conjugated goat anti-human IgG secondary antibody (Southern Biotech). Spots were developed with AEC Substrate Kit, Peroxidase (HRP) reagents (Vector Laboratories). The spots were quantified using the Cellular Technology Limited; CTL ImmunoSpot software.

3.3. RESULTS

3.3.1. *Workflow for quantifying IgG secretion by human plasma cells*

We first developed a workflow for loading and analyzing the secretions of single human B cells adhered to hydrogel nanovial particles (Fig. 3.5.1). This workflow involves capturing single cells into nanovial cavities by linking nanovials to conjugated antibodies targeted to surface proteins. Once captured into nanovials, cells are incubated to facilitate the accumulation of secreted IgG onto anti-IgG antibodies pre-coated to the cell-associated nanovial surface. The nanovial-bound secreted IgG and other cell surface markers are then tagged with antibodies with either fluorescent labels or oligonucleotide barcodes. Labeled nanovials and cells are then analyzed using flow cytometry, imaging flow cytometry, or sorted by FACS and analyzed by single-cell sequencing.

To identify optimal surface markers to capture ex vivo differentiated human plasmablast/plasma cells[9] into nanovials, we tested a panel of antibodies against surface proteins (CD45, CD27, CD38, CD31) expressed in B cells and analyzed capture by flow cytometry. Nanovials are made of highly transparent hydrogel, however, the shape and larger size leads to a unique scatter signature that is readily distinguished from other cell events[73]. Cells loaded on nanovials were discriminated from free cells and empty nanovials using a combination of flow

cytometry scatter and fluorescence gating. Based on live-dead stain, only live cells were gated in the downstream analysis (Fig. 3.5.2a). We found that antibodies against CD27 yielded the highest percentage of total cells captured, and the captured cells represented a broad range of cell types, including $CD19^{high}$ active B cells, as well as $CD19^{low}$ IgM^+ cells, IgA^+ cells, and IgM/IgA double negative cells (Fig. 3.5.2b).

3.3.2. *Quantifying IgG secretion in plasma cells expressing different cell surface markers*

Previously, we found heterogeneity in antibody secretion rate for plasma cells measured using ELISPOT (Fig. 1.3.1), however, we were unable to investigate these sub-populations further due to the inability to characterize other properties of cells in the ELISPOT format. Using nanovials, we can use flow cytometry to simultaneously quantify IgG secretion along with cell surface and intracellular proteins at the single-cell level. To explore the heterogeneity of phenotype in human antibody-secreting cells, we isolated B cells from peripheral blood mononuclear cells (PBMCs), and differentiated these into heterogeneous populations of plasma cells, plasmablasts and activated B cells ex vivo[9] (see methods for more details). After differentiation, we loaded cells onto 55 mm-diameter nanovials functionalized with anti-CD27 and anti-human IgG, and stained cells with a panel of B cell/plasma cell and immunoglobulin class surface markers to define sub-populations, as well as anti-IgG for detecting secreted IgG on nanovials (Fig. 3.5.3a). A large fraction of loaded B cells exhibited a phenotype consistent with plasmablasts (PBs) or plasma cells (PCs; $CD19^{lo}CD38^+$), which may represent antibody secreting cells (ASCs). A small portion of loaded cells exhibited a phenotype of activated B cells ($CD19^{hi}CD38^{lo}$). The ASCs could further be categorized by antibody isotype. We observed sub-populations of cells with surface expression of

IgM or IgA, and double negative (DN) cells that are most likely IgG^+ ASCs; few IgE cells are present in our culture system (Fig. 3.5.3b).

We next associated IgG secretion with the different B cell subtypes. As expected, activated B cells and the majority of IgA and IgM cells exhibited little to no IgG secretion (Fig. 3.5.3b). To address the potential cross-reactivity and diminish the signal from free cells in the loading step, we included unbound anti-IgG antibody in solution during the cell loading procedure to block these interactions. After making these changes to the protocol, we showed that IgM^+ cells had reduced IgG^+ signal (Fig. 3.5.4). A large percentage of DN cells exhibited high levels of IgG secretion (Fig. 3.5.3b-c). However, the distribution of IgG secretion in DN cells was bi-modal, indicating that a large percentage of these cells did not produce IgG despite the fact that most expressed surface markers that are conventionally associated with ASCs (Fig. 3.5.3c).

To further investigate the surface markers associated with IgG secretors, we further gated DN cells based on thresholds of CD38 and CD138 (boxes, Fig. 3.5.3c), markers which increase in expression during PC maturation. Of the DN cells, we observed increased proportions of IgG secreting cells depending on the expression of PB/PC maturation markers: low in immature PBs ($CD38^+CD138^{lo}$; ~20% IgG), intermediate in PBs ($CD38^{++}CD138^{lo}$; ~60% IgG) and high in PCs ($CD38^{++}CD138^{hi}$; ~80% IgG, Fig. 3.5.3c). Overall, these data showed that CD138 positivity was the best marker to identify a B cell as an IgG secretor or not (Fig. 3.5.3c). When we compared the mean fluorescence intensity (MFI) of IgG between PCs and immature PBs, we observed significant increases in the PCs (Fig. 3.5.3d). These data demonstrate that while PC phenotype corresponds to a large increase in the proportion of IgG secretors, there is also a small increase in secretion amount by PCs relative to immature PBs.

We used imaging flow cytometry (Amnis ImageStream) to confirm that the anti-IgG signals we observed in PCs originated from single cells and were secreted into the associated nanovial. We analyzed loaded B cells on ImageStream (Gating strategy, Fig. 3.5.5) and used the images to measure fluorescence on the nanovials and cells separately. The signal for secreted IgG was distinct from fluorescence in the cell and evident as a crescent/ring shape on the inner surface of nanovials (Fig. 3.5.3e). Upon quantification of IgG in the other cell phenotypes, we found that $CD38^{++}CD138^{hi}$ PCs exhibited significantly higher IgG^{+} signal relative to $CD38^{++}CD138^{lo}$ or $CD38^{+}$ cells (Fig. 3.5.3f and representative images Fig. 3.5.6). Collectively, these data indicate that $CD138^{hi}$ PCs are the predominant source of secreted IgG in human plasma cell cultures.

3.3.3. *Compatibility of nanovial analysis with single-cell sequencing*

We first evaluated the general compatibility of nanovials with single-cell transcriptomic sequencing using the 10X Genomics Chromium system. The Chromium system uses a microfluidic droplet generator to encapsulate cells with single barcoded hydrogel beads inside drops, where lysis and single-cell reverse transcription is performed. The gel beads contain oligonucleotides that hybridize to mRNA and other feature barcodes from the cell sample that also comprise a unique barcode that can be associated with each single cell. In our modified workflow, we simply replaced the cell sample in the microfluidic chip with nanovials loaded with cells (Fig. 3.5.7a). Nanovials with a diameter of 35 mm could be introduced into the microfluidic chips and entered into microfluidically generated droplets (Fig. 3.5.8a-b). Nanovials of larger sizes could flow through the chips, but only after deforming significantly to pass through the channels (Fig.

3.5.8c), which led to clogging in some experiments. To reduce the chance of clogging, we used 35 mm-diameter nanovials for the remaining single-cell sequencing experiments.

We found that mRNA from mouse hybridoma cells and human Raji cells seeded on nanovials was successfully transcribed and sequenced. The number of transcripts and transcribed genes recovered from Raji cells on nanovials was comparable to freely suspended cells (Fig. 3.5.7b). Notably, nanovials can be tagged with feature barcodes (a nanovial barcode) by coating with oligonucleotide-conjugated streptavidin. We used this feature to differentiate Raji cells loaded on nanovials from cells freely floating in suspension (Fig. 3.5.7b). Similarly, we used reads of anti-IgG associated feature barcodes to categorize hybridoma cells as off nanovial, on nanovial with low anti-IgG barcode reads, or on nanovial with high anti-IgG barcode reads (Fig. 3.5.7c). Similar to our results with Raji cells, we found a comparable number of transcripts and gene numbers recovered from hybridoma cells on nanovials when compared to free hybridoma cells, which were largely independent of the amount of IgG secretion (Fig. 3.5.7c).

We next evaluated mixing by loading mouse hybridoma cells and human Raji cells on separate batches of nanovials and mixing the batches together before loading them into the microfluidic device. We prepared nanovial samples at the recommended concentration to recover 1000 - 2000 cells (10,000 nanovials assuming 10-20% cell loading). At this concentration we found the majority of cells had single species-specific gene reads (Fig. 3.5.7d), while a small minority (1.5%) had both human and mouse reads, suggesting coincident loading of two cell types in a droplet (Fig. 3.5.9). We searched the cDNA library for heavy and light chain sequences for the anti-hen egg lysozyme (HEL) antibody produced by the hybridomas. Sequences were recovered from the hybridoma population and were not detected in the Raji

cells, as expected (Fig. 3.5.7d). Consequently, using nanovials did not lead to increased cell-cell mixing (i.e. shared barcodes for more than one cell) compared to statistical expectations.

By adding an oligonucleotide-barcoded anti-IgG label, we could link the secretion of IgG to the mouse transcriptome for individual cells on nanovials, an approach we refer to as secretion encoded cell sequencing (SEC-seq). As expected, the lowest number of anti-IgG feature barcode reads were associated with free cells (not loaded in nanovials) (Fig. 3.5.7e). In contrast, events with the highest IgG feature barcode reads were associated with mouse hybridomas on nanovials. As expected, most Raji cells on nanovials had low anti-IgG feature barcode reads, with a small group with higher reads proportional to the fraction of nanovial multiplet events (Fig. 3.5.7e).

3.3.4. *Simultaneous quantification of protein secretion and single-cell transcriptome sequencing (SEC-seq)*

After confirming the ability to perform linked secretion analysis and single-cell sequencing, we applied the SEC-seq technique to explore the transcriptomes of ex vivo differentiated human ASCs as a function of their IgG secretion phenotypes. In this workflow, we adapted the SEC-seq protocol by pre-sorting nanovials containing viable human B cells immediately prior to loading into emulsions with the 10X Barcoded Beads (Fig. 3.5.11a, and gating in Fig. 3.5.10a, Cell Ranger QC summary in Fig. 3.5.10b). The data from the sequencing was analyzed to simultaneously quantify IgG secretion (SEC) via signal from barcoded IgG antibodies (left panel, Fig. 3.5.10b) and gene expression sequencing (right panel, Fig. 3.5.10b). Clustering of the transcriptional data was largely driven by expression of the specific antibody isotypes (Fig. 3.5.12). The majority of IgG-secreting cells were in clusters expressing IGHG1, IGHG2, IGHG3 and IGHG4 (Fig. 3.5.12), with a small

minority in clusters expressing IGHM, IGHA1. We did *not* observe a strong correlation between the quantity of UMIs and IgG secretion signals (Fig. 3.5.10c). Finally, factors conventionally associated with PB/PC differentiation (XBP1, IRF4, PRDM1) were expressed uniformly in all subclusters, regardless of antibody isotype identity or IgG secretion level (Fig. 3.5.10d). Because the strength of the secretion signal did not correlate with overall transcription or with levels of conventional PB/PC transcriptional activators, we reasoned that additional differentially expressed genes specifically regulate IgG secretion.

3.3.5. *Using SEC-seq to determine transcriptional signatures associated with IgG secretion*

To classify PCs by isotypes, we used a similar strategy as we previously used to gate double negative cells by flow cytometry. The distributions for the gene counts of IgA and IgM were bimodal (Fig. 3.5.13a). We drew "gates" for $IGHM^+$, $IGHA^+$ at the local minimum between the modes in each distribution and further analyzed the DN cells (Fig. 3.5.13a). In agreement with the flow cytometry data, we observed a log increase in the median number of unique IgG barcode reads in the DN population relative to the IgM/IgA populations (Fig. 3.5.13b). Based on the distribution of IgG barcodes in the $IGHM/A^+$ cells, we calculated confidence intervals and established a cutoff of 5 logs (~90% confidence, red line Fig. 3.5.13b-c). We then segmented the population by defining IgG secretors as DN cells with unique IgG barcodes exceeding 5 logs plus ~30% and non-secretors with those with unique IgG barcodes fewer than 5 logs minus ~30% (dotted lines, Fig. 3.5.13c). Approximately 12% of the loaded nanovials were IgG positive in the cell sort (Fig. 3.5.10a, right panel), which is comparable to the ~14% of IgG secretors we quantified in the scRNA sequencing data.

Next, we asked how the IgG secretors were distributed in each subcluster. After projection of IgG secretors onto the UMAP (Fig. 3.5.13d), we found that the majority of IgG secretors (red dots) overlap with IgG clusters, and a small minority overlap with the IgA/M clusters (see also Fig. 3.5.12). Upon looking at the percentage of IgG secretors in each subcluster, we found that IgG clusters have on average ~ 25% IgG secretors and ~ 40% non-secretors, whereas the remaining clusters were predominantly non-secretors. The IGHG3 (cluster 9) and IGHG4 (cluster 11) subclusters exhibited higher and lower percentages of IgG-secreting cells, respectively, possibly indicating different levels of IgG secretion among PCs expressing these isotypes. In contrast, we found there was a similar percentage of IgG secretors and non-secretors when cells expressed either light chain kappa or lambda (Fig. 3.5.13d). One subcluster within the IgG group expressed the PC progenitor markers PAX5 and CD19 but exhibited a similar percentage of IgG-secretors (cluster 8, Fig. 3.5.13d-e), demonstrating that a subset of PC progenitors are capable of IgG secretion. Finally, although the PC markers CD38, PRDM1 (also known as BLIMP1), and TNFRSF17 (also known as BCMA) do not vary greatly among the subclusters, XBP1 (a master regulator of the unfolded protein response) is enriched in clusters 9 and 10,[74] those that have the largest numbers of IgG-secreting cells (Fig. 3.5.13d-e).

3.3.6. *IgG secretion is highly regulated by mitochondrial metabolism and protein transport*

Identifying genes associated with IgG secretion is a primary objective of this work. We conducted differential gene expression analysis to compare IgG secretors and non-secretors (see definition above). We then applied gene enrichment analysis (GSEA) to GO: biological process (Fig. 3.5.14a). The most highly enriched genes were related to mitochondrial associated gene sets, including ATP synthesis coupled electron transport, oxidative phosphorylation, mitochondrial

electron transport NADH to ubiquinone (Fig. 3.5.14a, Fig. 3.5.15a), etc. The other major enriched genes are translation process and trafficking proteins, e.g., endoplasmic reticulum (ER) to golgi vesicle mediated transport and protein localization to ER (Fig. 3.5.14a, Fig. 3.5.15a). We also applied GSEA to the HALLMARK dataset,and found MYC-target genes are highly enriched (Fig. 3.5.14b, Fig. 3.5.15b). Previous studies demonstrated that Myc target genes are highly associated with ribosome function, oxidative phosphorylation, protein export, etc[75,76].

We then listed the top highly and differentially expressed genes between secretors and non-secretors (Fig. 3.5.14c). Several UPR-relevant genes, e.g. SSR3, SSR4, and SEC61B, are known for being highly expressed in PCs[74,77]. Among the IgG isotypes, IGHG3 transcripts were increased in IgG secretors, although IGHG2 transcripts were decreased. As expected PCs expressed only one antibody isotype and the majority of IgG cells expressed IgG1 (75%), followed by IgG2 (12%), IgG3 (9%), and IgG4 (3%). As implied by the cluster analysis we found that IGHG3-expressing PCs had a higher percentage of IgG secretors, whereas those expressing IGHG2 and IGHG4 had fewer (Fig. 3.5.14d). Regardless of the isotype, we found little correlation between steady-state IgG transcripts and IgG secreted protein (Fig. 3.5.14e), which implies that steady-state transcript levels do not predict the degree of antibody secretion in PCs.

Contrary to our expectation, we found that transporters of fructose (SLC2A5), but not glucose (e.g. SLC2A1) were expressed more highly in IgG secretors. We evaluated glucose import by incubating PCs with the glucose analogue 2-NBDG. Consistent with the idea that the levels of glucose import do not drive antibody secretion we found that within DN cells there is no association between 2-NBDG import and IgG secretion (Fig. 3.5.14f left). In contrast, after staining for mitotracker and ER, we found that PCs with high mitochondrial volumes or cells

with high-ER content were predominantly IgG secretors (Fig. 3.5.14f, middle panel and right panel). Based on this integration of single-cell secretion and gene expression data, it is likely that the rate-limiting determinants of antibody production/secretion are the cellular programs required for protein secretion, rather than transcript availability. These programs include those regulating protein translation, ER/golgi transport, and protein post translational modification accompanied by mitochondrial respiration, autophagy, and oxidant detoxification (Fig. 3.5.14g).

3.4. DISCUSSION

The new methods introduced in this work allowed us to simultaneously interrogate the degree of IgG secretion with surface markers and mRNA at the single-cell level in primary human B cell subpopulations. In single experiments, we were able to analyze more than 3000 cells, directly linking IgG secretion amount with transcriptomes, and more than 8000 cells linking IgG secretion to surface markers. This unprecedented scale of experiments enabled characterization of secretion phenotypes in subpopulations of PCs. PCs that exclusively expressed *IGHG3* and to a lesser extent *IGHG1* were found to have a larger fraction of the subpopulation with IgG secretion signal compared to other subclasses. This could reflect a differential secretion rate or differences in anti-IgG binding that is subclass dependent[78,79]. Importantly, our data reinforce the need to assay cell secretory function directly, since gene expression of the underlying protein is not highly correlated to protein levels[80] or protein secretion. For example, the level of expression of any of the IgG heavy chain subclasses (IGHG1-4) individually had poor correlation to IgG secretion (Fig. 3.5.14e, r=0.10-0.18).

By leveraging standard equipment and workflows, the SEC-seq approach should be widely adoptable by other researchers, which promises to amplify the impact of the technique. Cells loaded on nanovials can be directly input into the microfluidic droplet generator used in the 10X Chromium system, and all other processes follow standard workflows for single-cell transcriptomics. Nanovials do not interfere with lysis, reverse transcription, or downstream cDNA library preparation or sequencing steps. The number of transcripts and gene count for cells on and off of nanovials remained similar (Fig. 3.5.7b) and doublet events remained comparable to those observed in cells alone (Fig. 3.5.7d). In fact, all of the components used to perform SEC-seq are commercially available including the biotinylated nanovials (Partillion Bioscience) and oligonucleotide barcoded antibodies (Biolegend). Linking secreted protein function with specific nucleic acid sequences of heavy and light chains of IgG (Fig. 3.5.7d) or alpha and beta chains of T cell receptors (TCRs) can enable functional discovery workflows for new monoclonal antibodies or engineered TCR-based therapies[22]. A parallel study is also exploring the transcriptome that underlies secretion of high levels of vascular endothelial growth factor by mesenchymal stromal cells (unpublished work), which can elucidate features associated with therapeutic sub-populations of cells. We demonstrate here that the technique is compatible with standard CITE-seq[81] reagents to create workflows that link surface proteins, secreted proteins, and single-cell transcriptomes[82]. More broadly, nanovials can link surface markers and secreted proteins in viable cells selected using multicolor FACS. Here we demonstrated an 8-color panel, but like surface-marker only panels, the scale of markers should only be limited by the spectral overlap of fluorophores.

CD138 has long been identified as a marker of differentiated human PCs, including long-lived PCs[6,83] that functionally regulates plasma cell survival in the bone marrow[84,85]. However,

there is no reported association between CD138 surface expression with the degree of antibody secretion. Here, we provide definitive evidence that CD138 is a useful marker for *ex vivo* differentiated human PCs that are actively secreting IgG. The marker enriches for the largest fraction of IgG secretors (>75%) compared to other markers like CD38. Similar to what has been observed previously[86,87], we also found that a subset of CD38low cells secrete IgG, and do so at a slightly decreased degree than other IgG secretors. In addition to the biological implications of these findings, the study also suggests that future work to isolate antibody sequence information from PCs, e.g. for discovery of monoclonal antibodies[88], should have the most success using CD138 as a marker for magnetic or nanovial-based enrichment.

Antibody-secreting plasma cells exhibit unique biochemical features that enable prolific protein secretion (reviewed in[89,90]). Protein secretion by PCs is regulated by a transcriptional program dependent on PRDM1 (also known as Blimp1) and the unfolded protein response gene, XBP1. PRDM1 is a multifunctional transcriptional activator and repressor involved in the maturation of developing B cells into PCs[91,92], and in maintenance of immunoglobulin secretion by PCs[93]. As expected, we observed that high IgG secretors exhibited increased mitochondrial and ER volume, as well as transcription of core pathways regulating mitochondrial biogenesis, ER, translation and processing of antibodies. These core secretory pathways are regulated by mTOR, which is activated by PRDM1[94] in PCs. We also identified several unexpected genes that are increased in IgG secretors and may be critical for their function including CD79A, the complement regulator CD59 and macrophage inhibitory factor MIF, which could regulate cells in the PC bone marrow microenvironment.

XBP1 is most highly expressed in the clusters with highest IgG secretion, which suggests that increased levels of the unfolded protein response pathway may facilitate increased

immunoglobulin secretion[95]. In contrast, PC-specific knockout of XBP1 eliminates immunoglobulin secretion[93] by PCs without eliciting cell death. Collectively, these results suggest that tuning XBP1 levels could transiently increase or decrease the amount of antibody secreted by PCs. To be activated, XBP1 transcripts are regulated at the level of splicing by the upstream unfolded protein response gene IRE1[96]. Recently, pharmacological compounds have been developed that increase[97] or decrease[98] IRE1 activity, and thus regulate the degree of spliced, active XBP1. In future studies, we envision using nanovials and/or SEC-seq to identify nontoxic pharmacological and/or genetic strategies that can increase and/or decrease immunoglobulin secretion. We envision that such molecules could be used to transiently increase the antibody responses to pathogens and/or decrease antibody responses in antibody-driven disease like lupus or arthritis.

We show that nanovial technology and SEC-seq can be used to link the levels of antibody secretion to cell surface markers, transcriptional signatures, and vital dyes. This technology enables us, for the first time, to study the molecular determinants of protein secretion by PCs. Because high and low secreting cells can be captured by cell sorting, we predict that this technique will be used to study PC secretion at a single cell level and co-evaluate a myriad of parameters including, but not limited to epigenetics, metabolomics, signaling, loss of function and mutational scans. Beyond the analysis of secreted immunoglobulins, the technique can unlock the ability to study >3000 proteins that are part of the human secretome,[99] ultimately identifying shared, or unique, molecular underpinnings of secretion pathways that are critical for cell communication and function from the single-cell to the organismal level.

3.5. FIGURES

3.5.1. *Workflow to link IgG secretion to surface markers and transcriptomes at the single-cell level.*

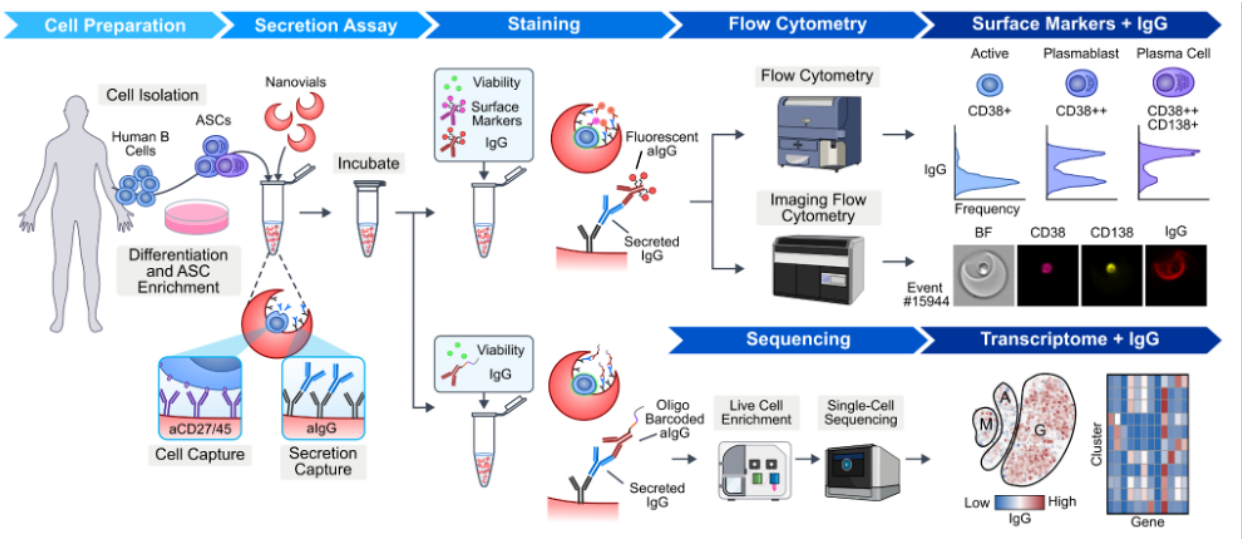

Human B cells are isolated from donors and expanded in a differentiation cocktail to enrich antibody secreting cells (ASCs). Cells are then loaded into a slurry of nanovials in a tube where they bind to antibodies on the nanovials against cell surface markers (CD27, CD45). Cells are incubated to accumulate secreted IgG on the nanovial surface via anti-IgG capture antibodies, and then nanovials are stained with fluorescent or oligo-barcoded anti-IgG. Cells associated with the nanovials are also stained with viability and other surface marker stains. Stained nanovials and associated cells are analyzed by flow cytometry (LSR II flow cytometer) or imaging flow cytometry (ImageStream) or sorted (Nanocellect WOLF) for single-cell transcriptomics using the 10X Chromium system. Data linking IgG secretion with surface markers and transcriptomes at the single-cell level is acquired and analyzed.

3.5.2. *Nanovial secretion assay flow cytometry gating strategy and characterization of cell loading using antibodies against different cell surface markers.*

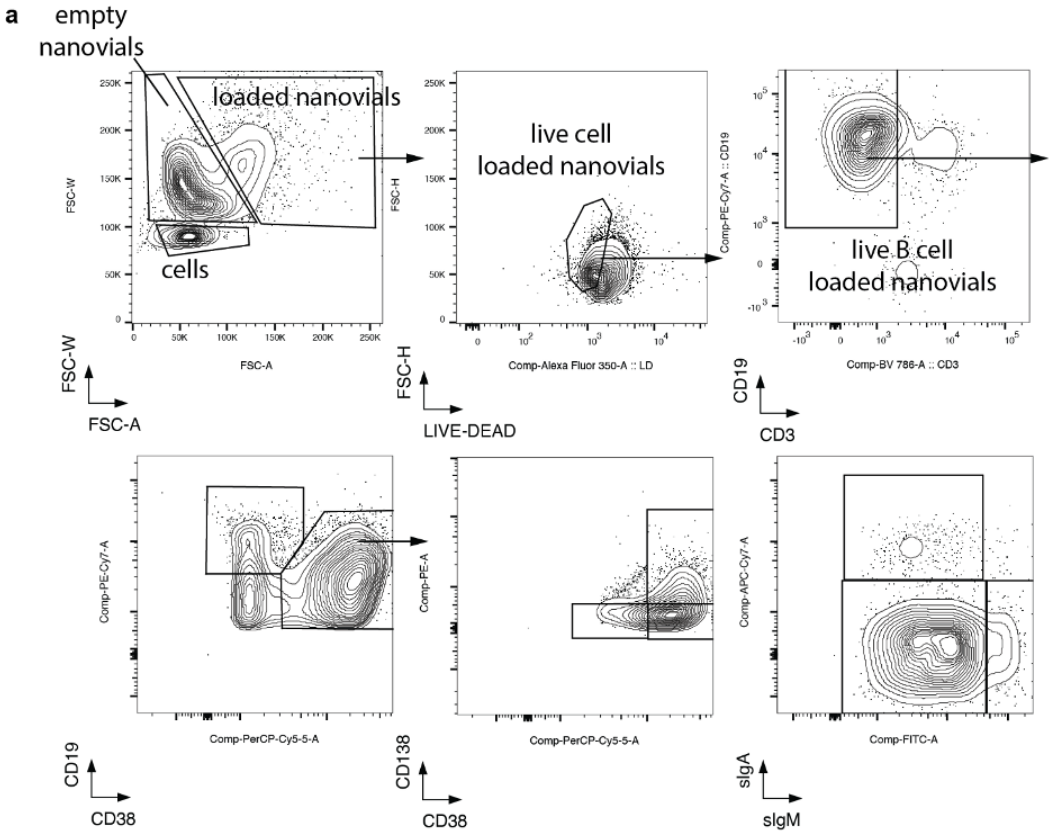

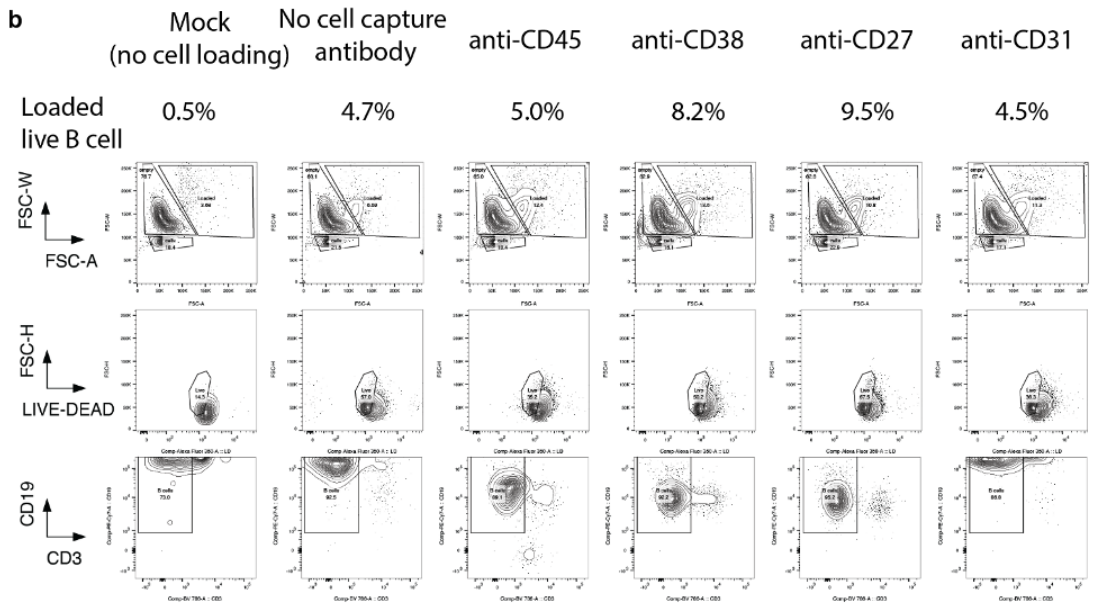

(a) Gating strategy for live B cell loaded nanovials used for surface marker and IgG secretion analysis. **(b)** Flow plots of cell loading with different cell capture antibodies linked to the nanovials. Loaded live B cell percentage is calculated by dividing the loaded live B cell counts by the total number of nanovial counts (loaded nanovial counts + empty nanovial counts).

3.5.3. *Linking IgG secretion to cell surface markers and intracellular machinery using flow cytometry.*

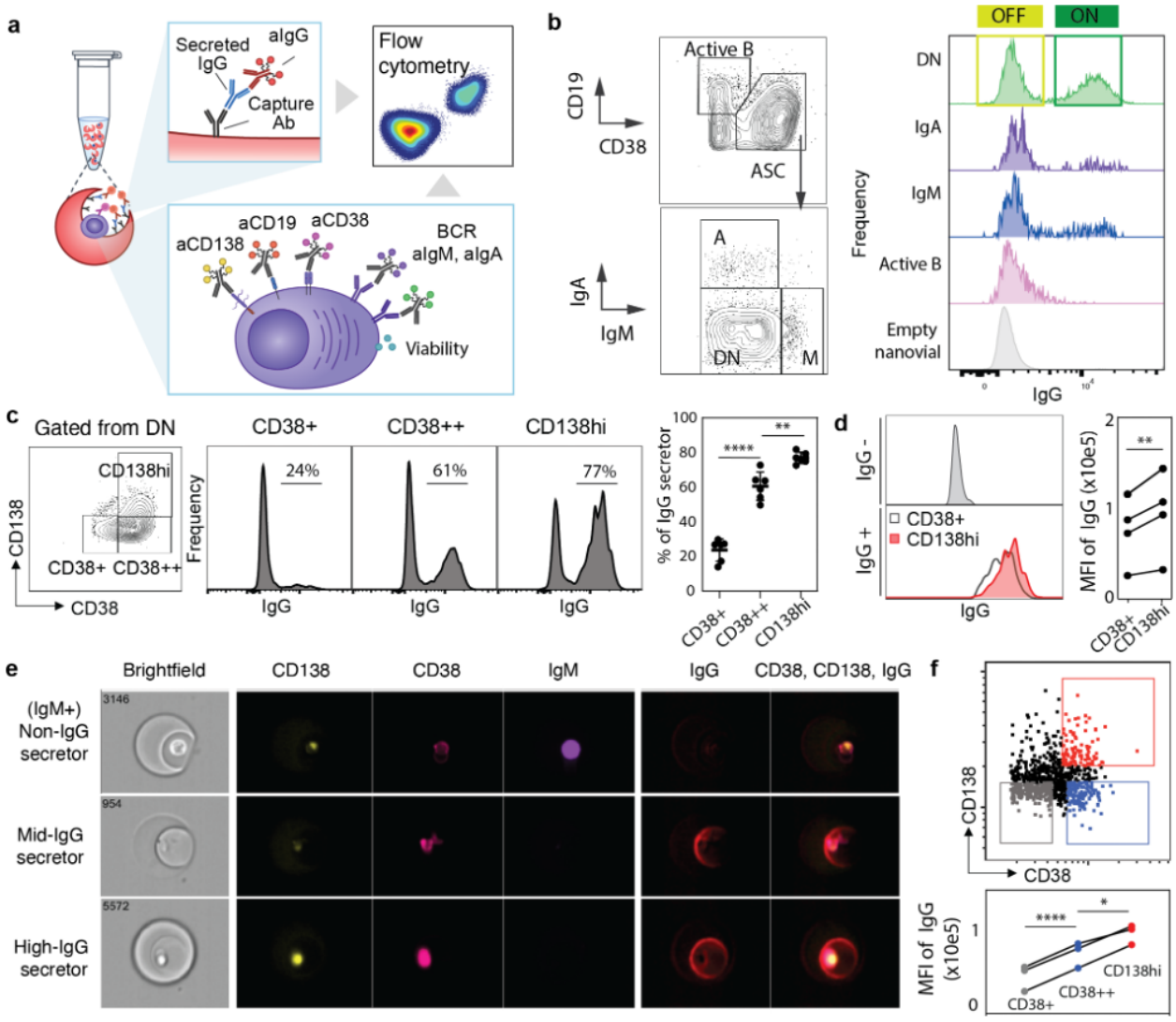

(**a**) Schematic of staining format used to analyze single B cell IgG secretion and cell surface markers using flow cytometry. (**b**) Flow cytometry density scatter plots for surface markers to identify populations of ASCs from active B cells (n=999) using CD19 and CD38 staining. IgA cells (n=319), IgM cells (n=436), and ASCs not producing either IgA or IgM (double negative, DN, n=6004)) were gated based on IgA and IgM staining. Fluorescence histograms of IgG secretion signal for the various identified gates and empty nanovials containing no cells. (**c**)

Contour plot for CD38 and CD138 staining in the DN population and fluorescence histograms of IgG signal from populations within these gates. Dot graph presents the % of IgG secretors from each ASCs subset (n = 5, from 2 donors). To assess significance, we used a paired one-way ANOVA with Tukey's multiple comparison test (* $p < 0.05$, ** $p < 0.01$, *** $p < 0.001$). (**d**) Histogram of IgG levels for IgG non-secretors and IgG secretors from different ASC subsets. Linked dot graph presents the mean fluorescence intensity (MFI) of IgG secretors from each ASC subset. A two-sided paired t-test is performed for each experiment (n = 4, from 1 donor); significance is under a significance level of $\alpha = 0.05$. (* $p < 0.05$, ** $p < 0.01$, *** $p < 0.001$). (**e**) Imaging cytometry results confirm that IgM^+ cells have low levels of secreted IgG, CD138low and CD38low populations have intermediate levels of secreted IgG, and $CD138^+CD38^{++}$ have the highest levels of secreted IgG. (**f**) Imaging flow cytometry gating strategy for IgG quantification by cell subtype (upper). Dot graph presents the MFI of IgG from each ASC subset (n = 3, from 3 individual donors). To assess significance, we used a paired one-way ANOVA with Tukey's multiple comparison test (* $p < 0.05$, ** $p < 0.01$, *** $p < 0.001$).

3.5.4. *Nanovial secretion with or without anti-IgG blocking.*

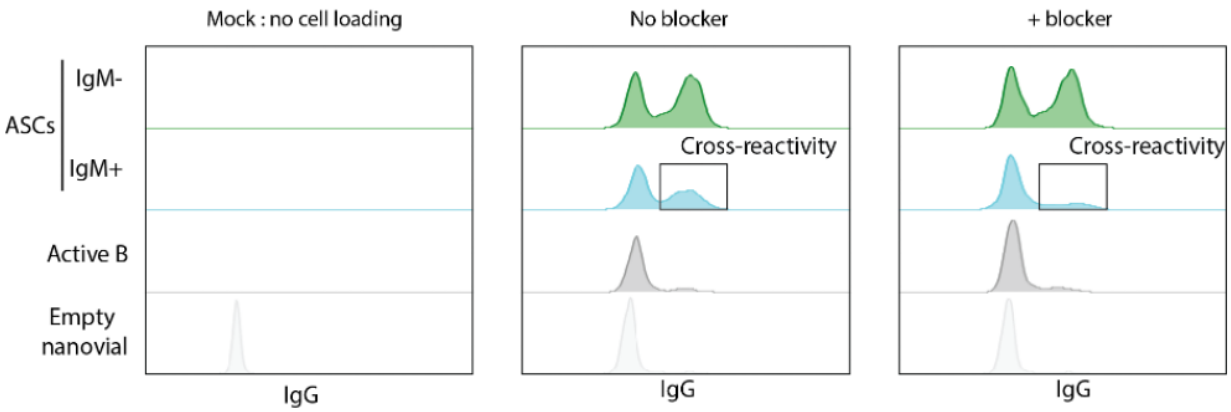

We adjusted the loading strategy to reduce cross-reactive IgG signal to nanovials containing IgM cells. In order to reduce cross-reactivity cells are incubated with anti-IgG as a sink for secreted IgG during the cell loading step and then the anti-IgG solution is washed prior to the cell secretion incubation step.

3.5.5. *Nanovial secretion assay gating strategy on the ImageStreamX® MKII.*

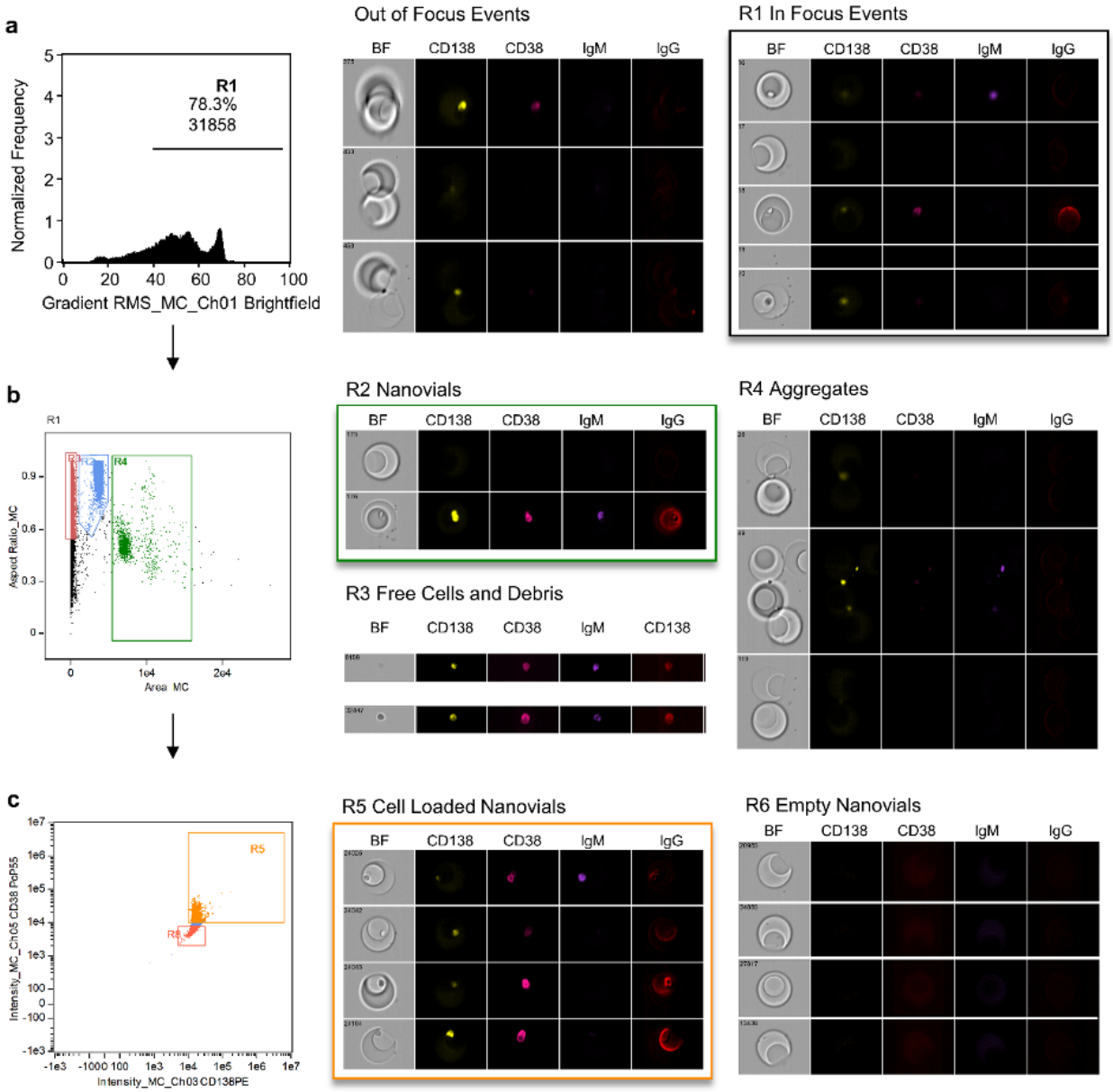

(a) In focus events are identified by gating on the root mean square gradient of the brightfield channel (Gate R1). **(b)** Events associated with small debris, free cells, nanovials, and nanovial aggregates can be assigned based on the aspect ratio and area of the event. Gate R2 contains single nanovials. **(c)** Cell-loaded nanovials are then gated based on a threshold level of CD38 and CD138 signals (Gate R5).

3.5.6. *Additional images of cell loaded nanovials taken with the ImageStreamX® MKII.*

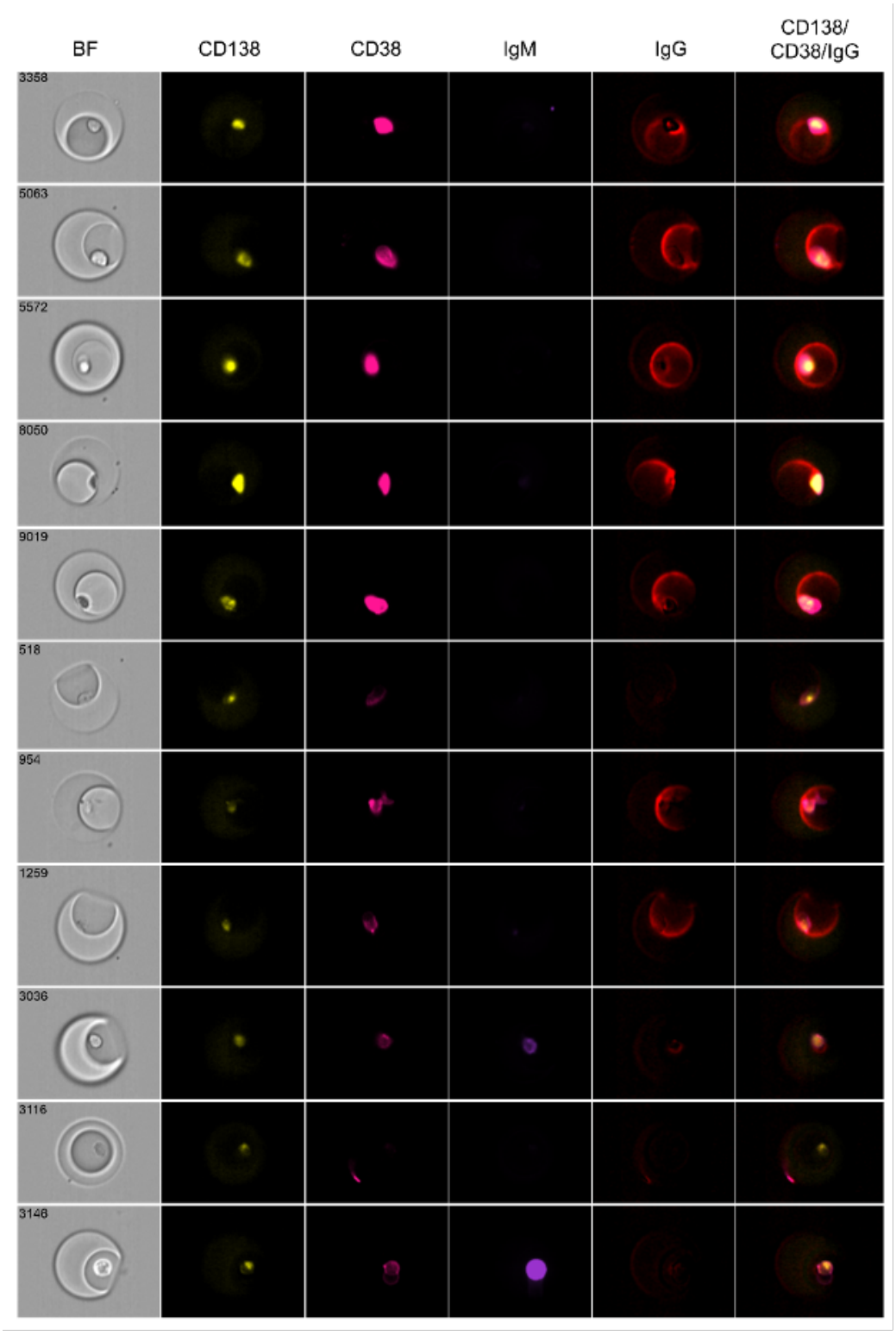

Compared to the punctate cell surface signal for surface markers, the secreted IgG signal is clearly seen across the hemispherical cavity of the nanovial.

3.5.7. *Compatibility of nanovials with single-cell transcriptomic sequencing using the 10X Genomics Chromium system.*

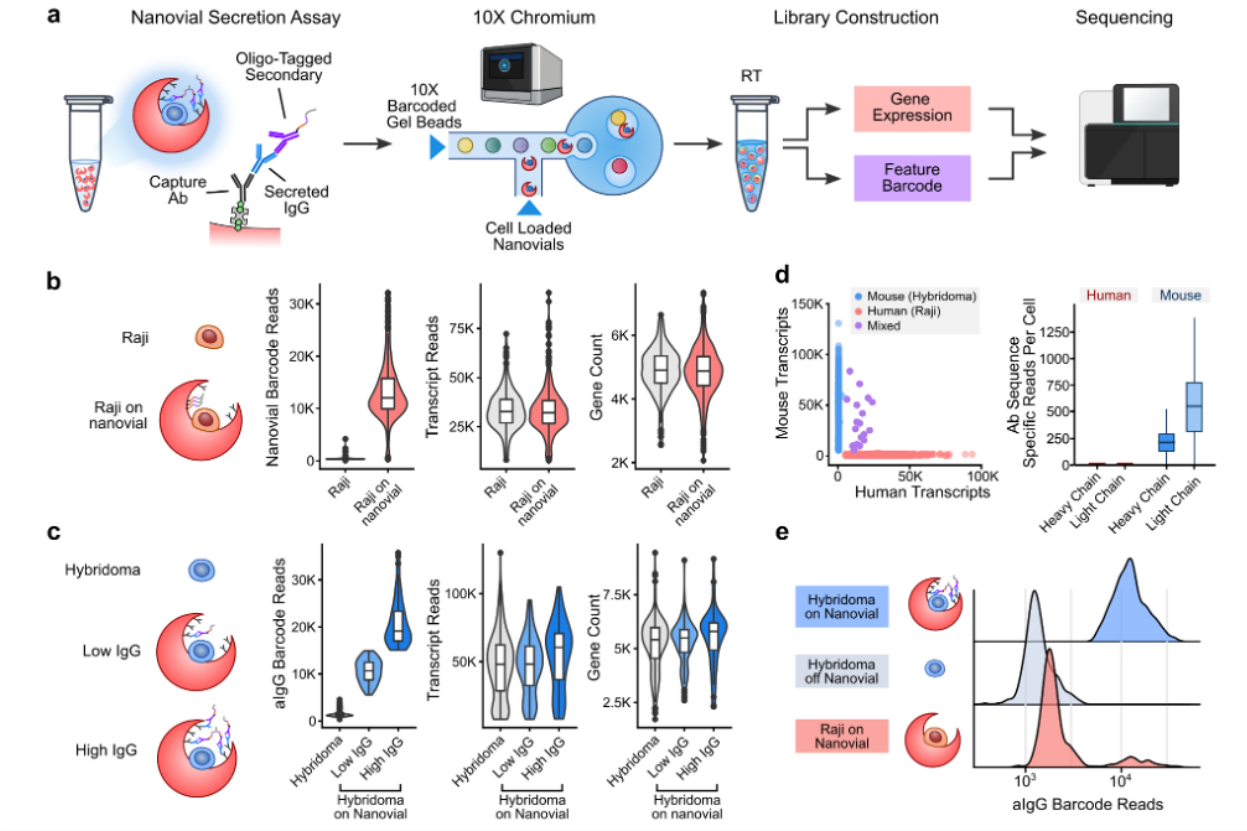

(**a**) Workflow for barcoding and analyzing secretions on nanovials. Captured secreted IgG is labeled with oligonucleotide-modified anti-IgG antibodies. Nanovials and associated cells are introduced into the 10X Chromium Next GEM Chip and emulsions are formed containing nanovials and Barcoded Gel Beads. Reverse transcription (RT) is performed to create cDNA and then amplified to form separate feature barcode and gene expression libraries. These libraries are sequenced, and feature barcode reads are linked to each cell's transcriptomes. (**b**) Human Raji cells on nanovials (transcripts linked with a streptavidin feature barcode, Nanovial Barcode) are compared with Raji cells off nanovials based on the number of transcript reads and gene count.

(**c**) Mouse hybridoma cells that secrete IgG that are off nanovials are compared to cells on nanovials based on the number of anti-IgG feature barcode reads, transcript reads, and gene count. (**d**) Scatter plot of mouse vs. human transcript counts when equal amounts of human Raji and mouse hybridoma cells on nanovials are input into the Chromium system. Specific heavy and light chain antibody sequences are recovered from mouse hybridoma cells. (**e**) Secreted IgG feature barcode read histograms for hybridomas on nanovials, hybridomas off nanovials, and Raji cells on nanovials.

3.5.8. *High-speed microscopy images of the 10X Genomics gel beads and nanovials loading into droplets formed on the 10X Next GEM chip G.*

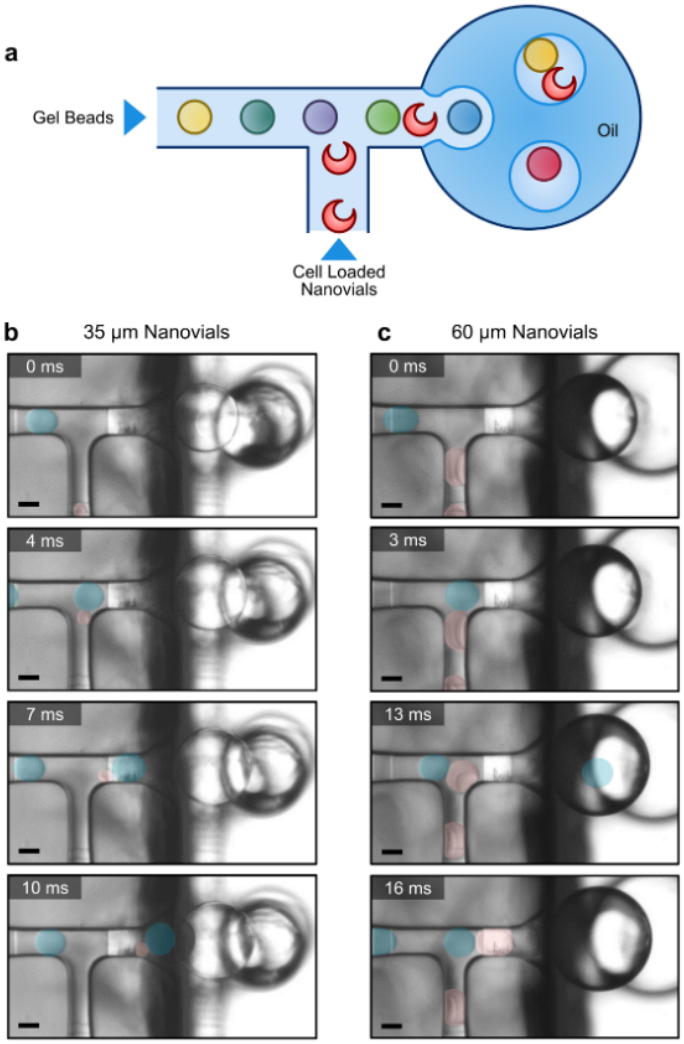

(a) Gel beads and nanovials are loaded through the gel bead inlet and cell sample inlets, respectively, as shown in the illustration. (b) 35 µm outer diameter nanovials pass through the cell sample inlet without obstruction and load into forming droplets. (c) 60 µm nanovials become constrained in the sample inlet and eventually pass through after deforming. Gel Beads and nanovials are false-colored blue and pink, respectively, to aid in visualization. Scale bar: 50 µm.

3.5.9. *Statistics on multiplet events from the mixed species experiments shown in*

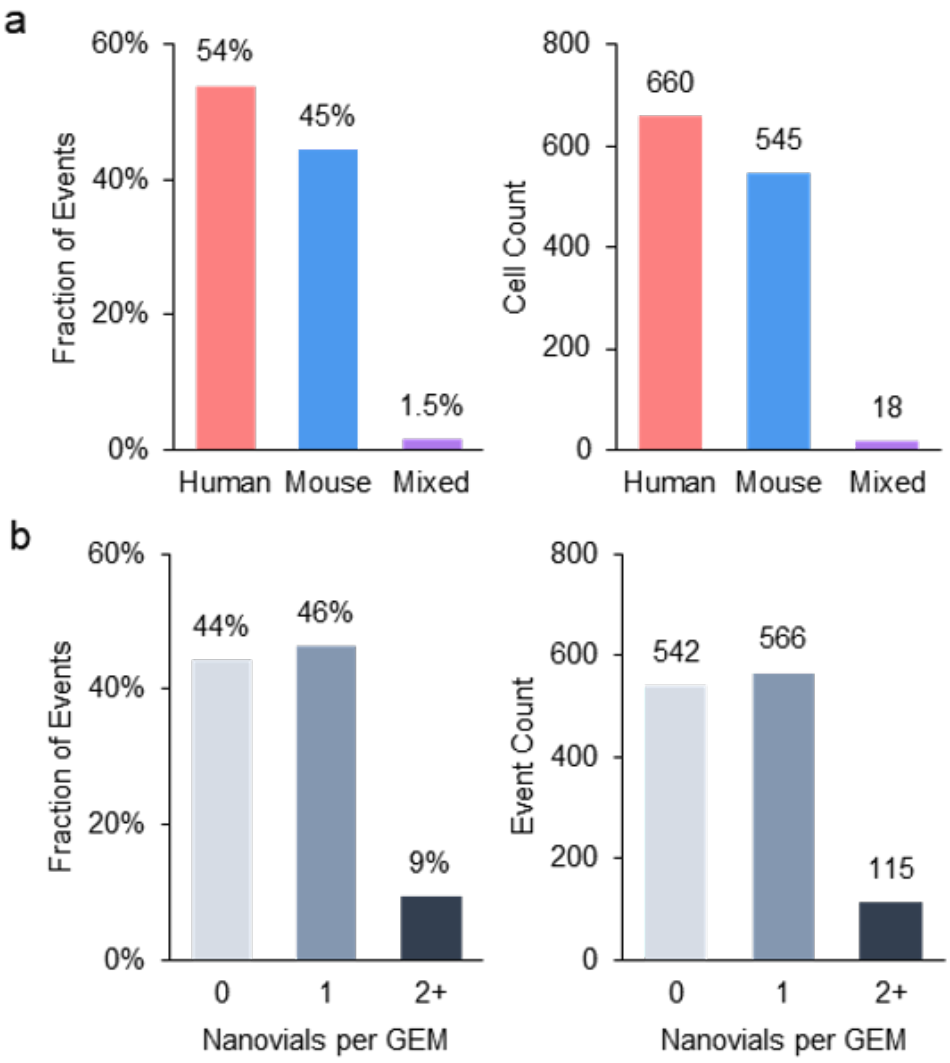

Nanovials were loaded into the 10X Chromium chip at the recommended concentration for cells to achieve 10,000 nanovial events. Approximately 10% of nanovials were loaded with cells and a roughly equal population of cells were off the nanovials. (a) The fraction of events based on species classification are plotted. The cell multiplet rate is close to the expected value reported in the 10X literature based on cell count (0.8% expected, 1.5% actual). (b) Fraction of events associated with 0, 1, or 2 or more nanovials. Using feature barcode reads on nanovials we

discriminated the number of nanovials per cell event. Given there are ~10 times the number of nanovials as cells for this experiment the number of events with multiple nanovials are within the expected range (7.6% expected, 9% actual).

3.5.10. *Sorting live-cell-containing nanovials for SEC-seq and Cell Ranger QC*

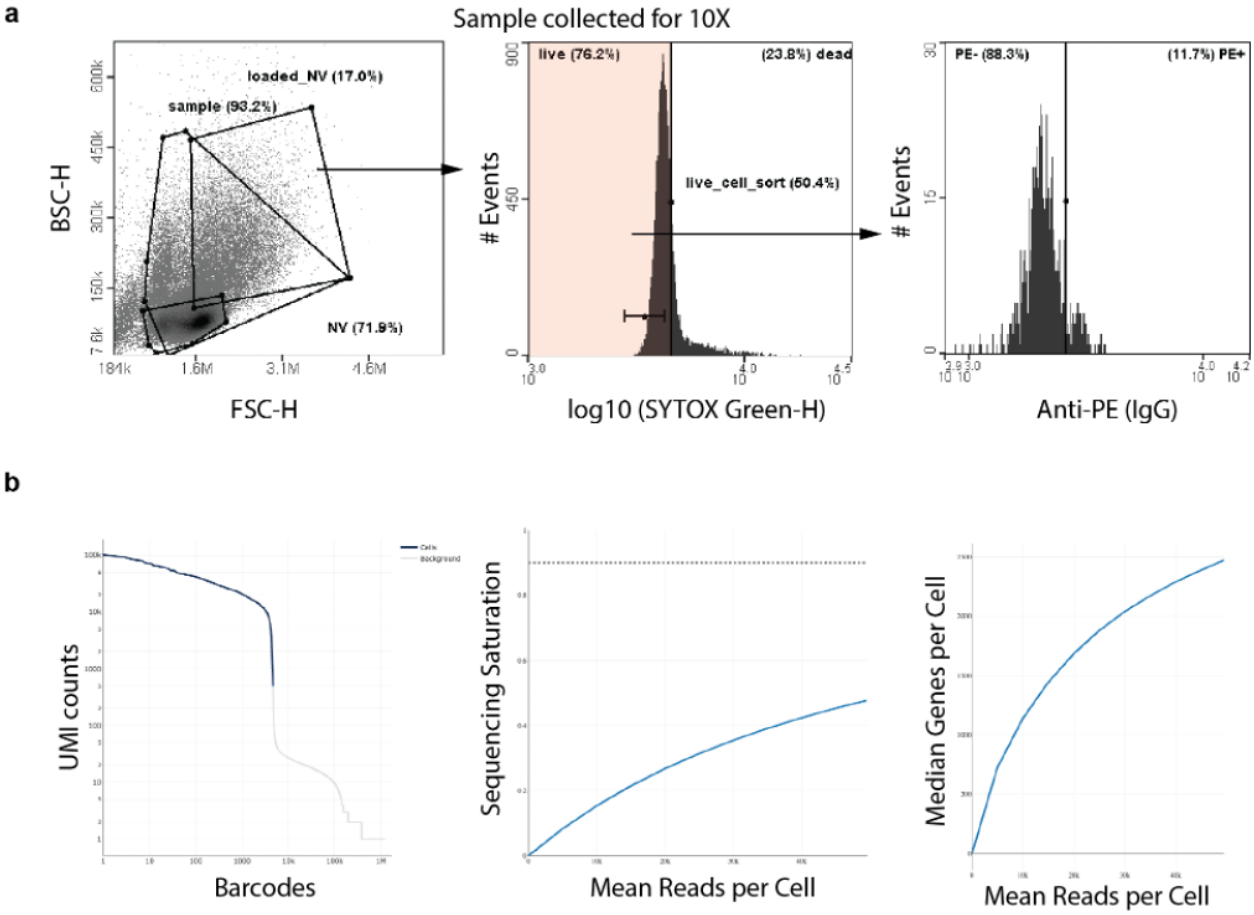

(a) Sorting strategy for live-cell-containing nanovials using the Nanocellect WOLF prior to loading into the 10X Chromium Next GEM chip. All live cells that were loaded on nanovials were collected independent of secretion amount. Analysis of the sorted population showed a distribution of secretors with ~12% of the population above the marked threshold. **(b)** 10X Cell Ranger QC summary. Barcode rank plot represents the UMI count separation between cells and background (left). Sequencing saturation plot shows the sequencing depth is ~50% by using a NextSeq 1000/2000 kit (middle). Median genes per cell plot shows the full sequencing depth is about 2500 median genes per cell.

3.5.11. *SEC-seq: single-cell transcriptomic sequencing associated with IgG secretion.*

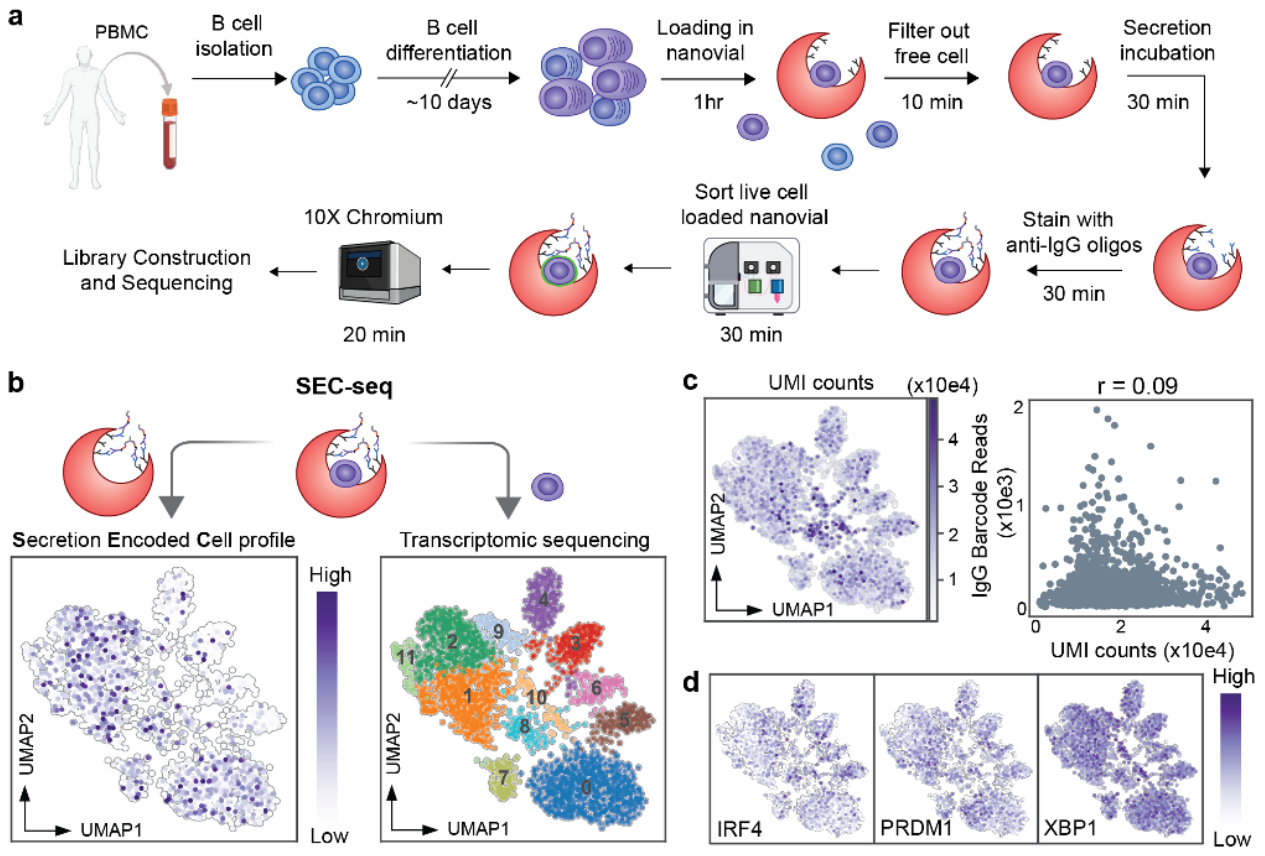

(a) Workflow for SEC-seq to link IgG secretion to transcriptome at the single-cell level. **(b)** Transcriptome-based clustering of single-cell expression profiles of human ASCs (right), and corresponding secreted IgG levels projected on the same UMAP plot (left), n = 3060. **(c)** UMI counts projected on the UMAP (left), and scatter plot of UMI counts and IgG barcode reads (right). r is Pearson correlation coefficient. **(d)** Transcript levels of representative genes projected on the UMAP plot from panel (b) represents transcription factors (TFs) for plasma cells (PCs).

3.5.12. *UMAP of immunoglobulins.*

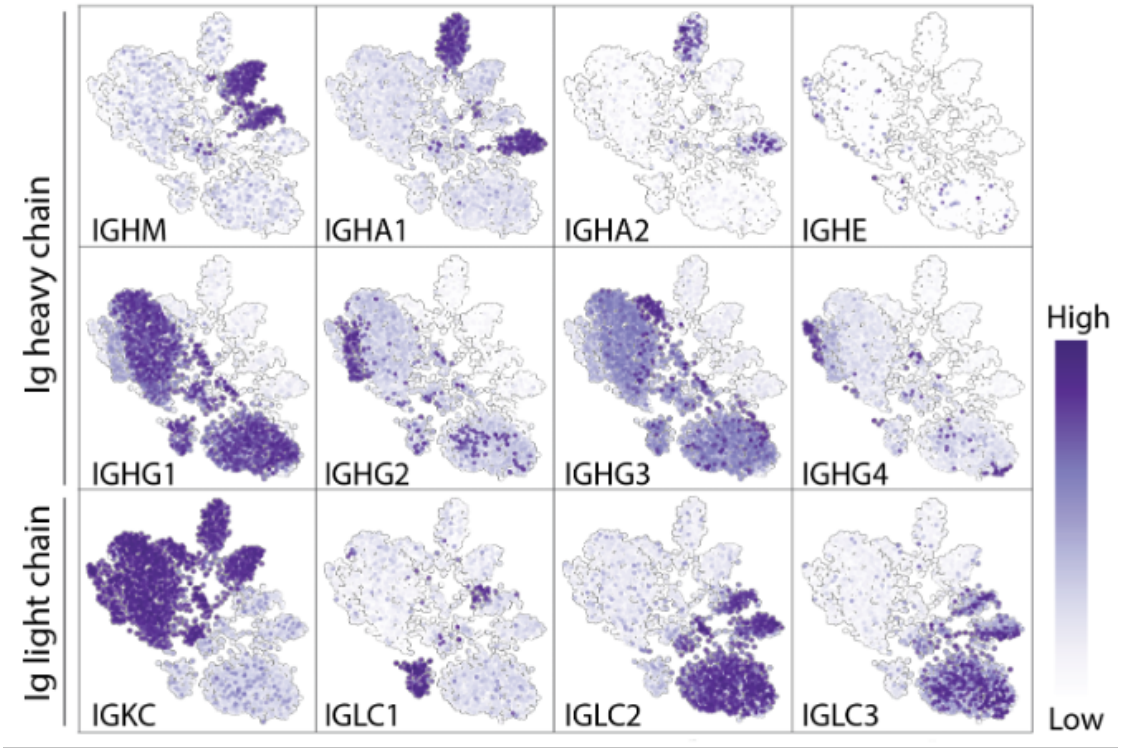

Transcript levels of immunoglobulin genes projected on the UMAP plot from Figure 4b. The top row represents non-IgG immunoglobulin classes, the middle row represents IgG subclasses, and the bottom row represents immunoglobulin light chain.

3.5.13. *IgG secretors are associated with different gene expression clusters.*

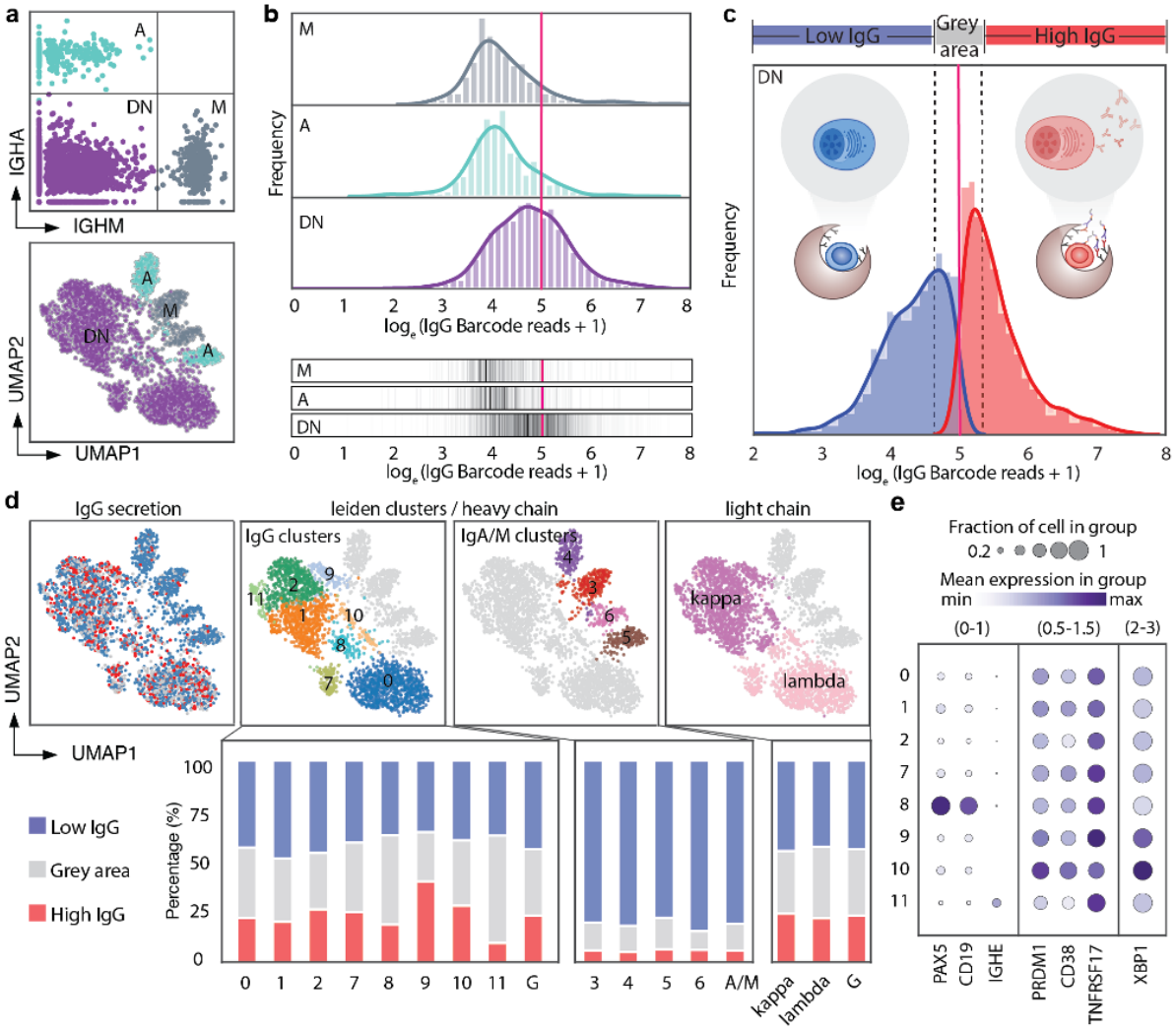

(a) IgM, IgA and DN populations are gated based on expression level of *IGHA* and *IGHM* genes. Identified populations are projected on the gene expression UMAP plot. (b) Histogram (upper) and density gradient graph (lower) of unique IgG barcode reads in each subset. Red line is a threshold set at 5 log reads. (c) Schematic describing the thresholding used to define high IgG secretors, intermediate (grey area), and non-secretors (d) IgG secretors (red) and non-secretors (blue) projected onto UMAP; IgG clusters, IgA/M clusters and light chain clusters of UMAP (upper). Bar graphs display the percentage of in the three thresholded regions using thresholds of

below 4.7 (non-secretors), between 4.7 and 5.3 (grey area), and above 5.3 (secretors) for each indicated cluster corresponding to the upper panel. (e) Dot plot from numbered clusters identified in (d) with indicated genes associated with a low percentage of IgG secretors (clusters 8,11) and a high percentage IgG secretors (clusters 9, 10). Numbers on top of the dot plot with parentheses indicate the minimum and maximum of mean expression in each column.

3.5.14. *Analysis of SEC-seq data to identify enriched genes associated with IgG secretion.*

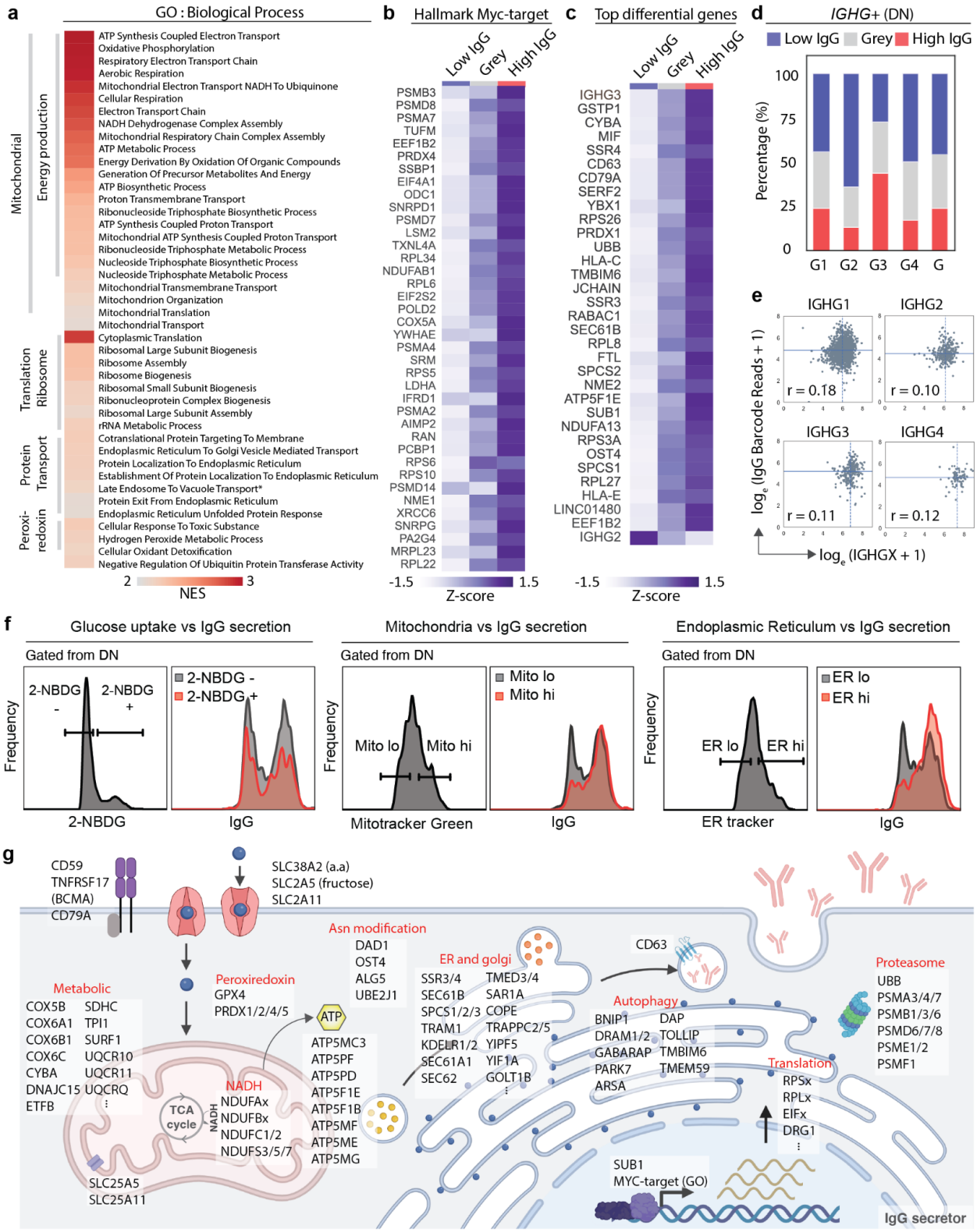

Gene set enriched list in GO biological process from gene set enrichment analysis (GSEA); heatmap represents the normalized enrichment score (NES). **(b)** ~Top 40 genes enriched in HALLMARK MYC TARGETS V1 from GSEA. Heatmap represents the z-score of mean of gene expression from each group. **(c)** Top differentially expressed genes and highly expressed (adjusted p-value < 0.1 and mean of gene expression > 5) of IgG secretors. Heatmap represents the z-score of mean of gene expression from each group.**(d)** Bar graphs display the percentage of cells in the three thresholded regions using thresholds of below 4.7 (non-secretors), between 4.7 and 5.3 (grey area), and above 5.3 (secretors) for each sub-class of IgG. **(e)** Scatter plots of IGHG log transcripts and log IgG barcode reads. The horizontal lines represent the median of IgG barcode reads and the vertical lines represent the median of IGHG transcript reads. r is the Pearson correlation coefficient. **(f)** Histograms of IgG secretion levels compared with glucose uptake +/-, high/low mitochondria activity and high/low ER amount. (**g**) Schematic cartoon of top 500 genes upregulated in IgG secretors based on different gene function clustering (DAVID) and GSEA.

3.5.15. *GSEA plot and gene list in core enrichment.*

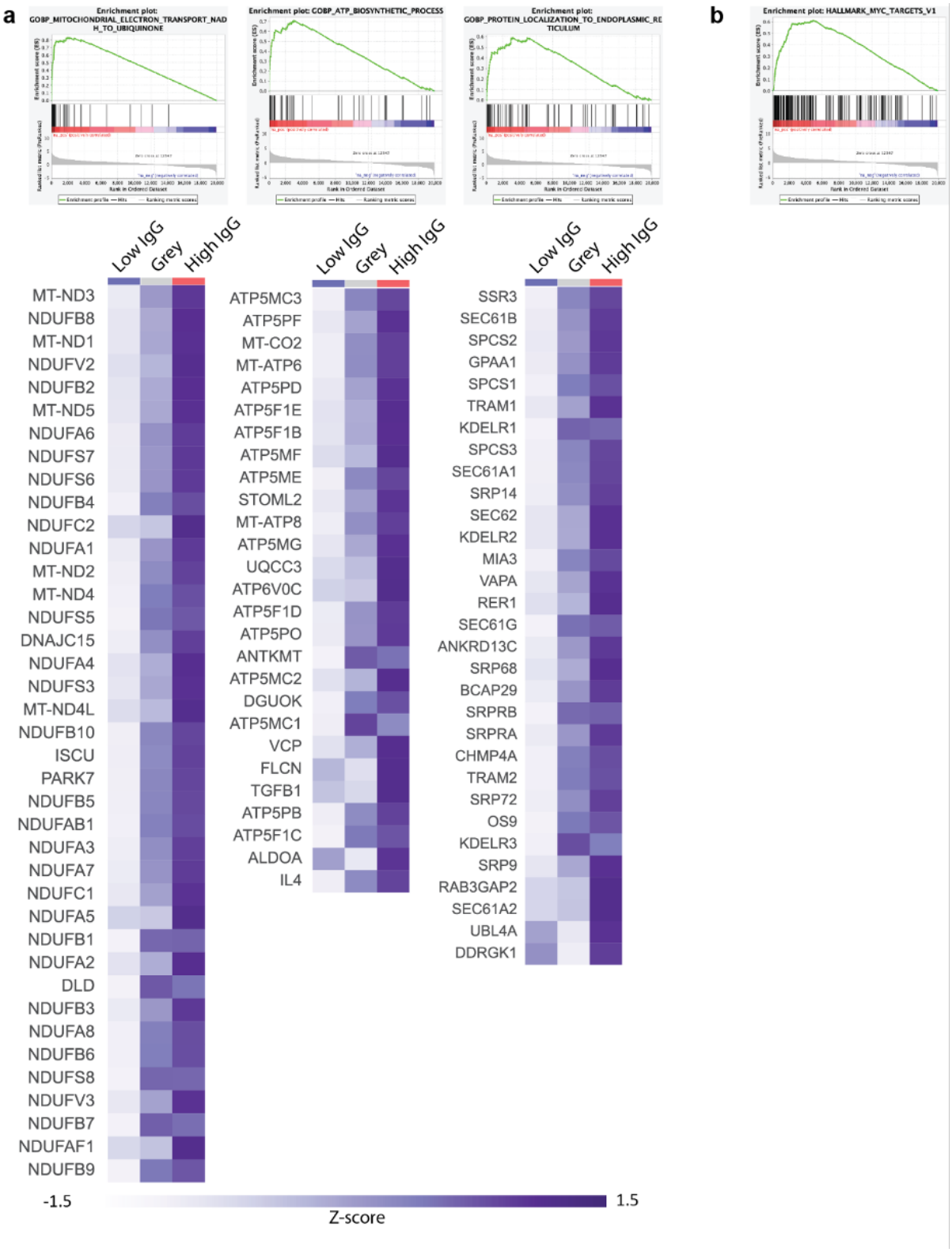

(a) Representative GSEA plots and gene lists in core enrichment in GO biological process: Mitochondrial electron transport NADH to ubiquinone (left), ATP biosynthesis process (middle) and Protein localization to endoplasmic reticulum (right). (b) GSEA plot of Hallmark MYC-targets V1 that have the expanded gene list in Figure 6.

3.6. TABLES

3.6.1. *Buffer and reagents*

Buffer/Medium	Item	Vendor	Catalog	Concentration
Washing buffer	DPBS	Fisher Scientific	14190250	
	BSA	VWR life science	0332-100G	0.50%
	Pluronic F-127	Sigma	P2443-250G	0.05%
Staining buffer	DPBS	Fisher Scientific	14190250	
	FBS	Sigma	F0926-500ML	2%
	Pluronic F-127	Sigma	P2443-250G	0.05%
Sorting Buffer	PBS	Cytiva	SH30256.01	
	Blocker BAS (10%) in PBS	Thermo Scientific	37525	1%
	Pluronic F-127	Sigma	P2443-250G	0.05%
B cell loading medium	DMEM+GlutaMAX	Gibco	10569-010	
B cell secretion medium	Lonza BioWhittaker Iscove's Modified Dulbecco's Medium (IMDM) without L-Glutamine	Fisher	BW12726F	
	FBS	Sigma	F0926-500ML	10%
	GlutaMAX 100X	Gibco	35050-061	1X
	2-Mercaptoethanol	Fisher	O3446I-100	55um

3.6.2. *Antibodies*

Experiment	Item	Vendor	Catalog	Clone
human B cell capture antibody	Biotin anti-human CD45 Antibody	Biolegend	304004	HI30
human B cell capture antibody	Biotin anti-human CD38 Antibody	Biolegend	303518	HIT2
human B cell capture antibody	Biotin anti-human CD27 Antibody	Biolegend	356426	M-T271
human B cell capture antibody	Biotin anti-human CD31 Antibody	Biolegend	536604	O92E4
human IgG capture antibody/blocking antibody	Goat Anti-Human IgG Fc, Multi-Species SP ads-BIOT	Southern Biotech	2014-08	Polyclonal
Flow Cytometry	PE-Cy7 anti-human CD19	Biolegend	302216	HIB19
Flow Cytometry/Amnis	PerCP-Cy5.5 anti-human CD38	BD	BDB551400	HIT2
Flow Cytometry/Amnis	PE anti-human CD138	Biolegend	356504	MI15
Flow Cytometry/Amnis	PacBlue anti-human IgM	Biolegend	314514	MHM-88
Flow Cytometry	APC anti-human IgM	BD	551062	G20-127
Flow Cytometry	APC-Vio® 770 IgA Antibody, anti-human	Miltenyi	130-113-473	IS11-8E10
Flow Cytometry	AF700 anti-human IgG	BD	561296	G18-145
Amnis	APC anti-human IgG	BD	562025	G18-145
SEC-seq cross-sp	TotalSeq™-C0971 Streptavidin	Biolegend	405271	
SEC-seq cross-sp	anti-mouse CD45	R&D Systems	AF114	Polyclonal
SEC-seq cross-sp	Goat anti-Mouse IgG FC	Jackson Immuno Research	115-065-071	Polyclonal

SEC-seq cross-sp	TotalSeq™-C1167 anti-mouse IgG1 Antibody	Biolegend	406636	RMG1-1
SEC-seq	PE Mouse Anti-Human IgG	BD	555787	G18-145
SEC-seq	TotalSeq™-B0911anti-phycoerythrin (PE) Antibody	Biolegend	408113	PE001

3.6.3. *ImageStreamX MKII fluorochrome layout*

Ch	Band	Fluorochrome	Target	Notes
1	430-470	Brightfield	Morphology	FIXED
2	470-560			
3	560-595			
4	595-660	PE	CD138	Plasma cell marker
5	660-745	PerCP Cy5.5	CD38	Plasmablast/plasma cell marker
6	745-785	SSC	Granularity	
7	430-505	Pac Blue	IgM	Surface bound, not captured on nanovial
8	505-575			
9	575-595	Brightfield	Morphology	FIXED
10	595-660			
11	660-720	APC	IgG	Antibody released to nanovial by plasma B cells
12	720-785			

3.6.4. *ImageStreamX MKII collection information*

Instrument: ISX 493	405 power: 120mw	488 power: 400mW	560 power: Off	
592 power: Off	642 power: 150mW	785 power: 2 mW	Mag: 20x	
INSPIRE: Current	Bin: None	Core diameter: 10	Velocity: 66	%Bd: 7
CameraSync: 38.9	Focus: 0.89	Core Tracking: 11	Focus Tracking: 0	

3.7. BIBLIOGRAPHY

71.Cheng, R. Y.-H. *et al.* SEC-seq: Association of molecular signatures with antibody secretion in thousands of single human plasma cells. *bioRxiv* 2022.08.25.505190 (2022) doi:10.1101/2022.08.25.505190.

72.de Rutte, J. *et al.* Suspendable Hydrogel Nanovials for Massively Parallel Single-Cell Functional Analysis and Sorting. *ACS Nano* (2022) doi:10.1021/acsnano.1c11420.

73.de Rutte, J., Dimatteo, R., Zhu, S., Archang, M. M. & Di Carlo, D. Sorting single-cell microcarriers using commercial flow cytometers. *SLAS Technol* **27**, 150–159 (2022).

74.Shaffer, A. L. *et al.* XBP1, downstream of Blimp-1, expands the secretory apparatus and other organelles, and increases protein synthesis in plasma cell differentiation. *Immunity* **21**, 81–93 (2004).

75.Kim, J., Lee, J.-H. & Iyer, V. R. Global identification of Myc target genes reveals its direct role in mitochondrial biogenesis and its E-box usage in vivo. *PLoS One* **3**, e1798 (2008).

76.Luo, P. *et al.* Transcriptional positive cofactor 4 promotes breast cancer proliferation and metastasis through c-Myc mediated Warburg effect. *Cell Commun. Signal.* **17**, 36 (2019).

77.Schubert, D. *et al.* Plasma cell deficiency in human subjects with heterozygous mutations in Sec61 translocon alpha 1 subunit (SEC61A1). *Journal of Allergy and Clinical Immunology* vol. 141 1427–1438 Preprint at https://doi.org/10.1016/j.jaci.2017.06.042 (2018).

78.Roux, K. H., Strelets, L. & Michaelsen, T. E. Flexibility of human IgG subclasses. *J. Immunol.* **159**, 3372–3382 (1997).

79.Carrasco, B. *et al.* Crystallohydrodynamics for solving the hydration problem for multi-domain proteins: open physiological conformations for human IgG. *Biophys. Chem.* **93**, 181–196 (2001).

80.Reimegård, J. *et al.* A combined approach for single-cell mRNA and intracellular protein expression analysis. *Commun Biol* **4**, 624 (2021).

81.Stoeckius, M. *et al.* Large-scale simultaneous measurement of epitopes and transcriptomes in single cells. Preprint at https://doi.org/10.1101/113068.

82.Steier, Z. *et al.* Single-cell multi-omic analysis of thymocyte development reveals NFAT as a driver of CD4/CD8 lineage commitment. Preprint at https://doi.org/10.1101/2021.07.12.452119.

83.Wijdenes, J. *et al.* A plasmocyte selective monoclonal antibody (B-B4) recognizes syndecan-1. *Br. J. Haematol.* **94**, 318–323 (1996).

84.McCarron, M. J., Park, P. W. & Fooksman, D. R. CD138 mediates selection of mature plasma cells by regulating their survival. *Blood* **129**, 2749–2759 (2017).

85.Joyner, C. J. *et al.* Maturation of Human Long-lived Plasma Cells Results in Resistance to Apoptosis by Transcriptional and Epigenetic Regulation. *bioRxiv* 2021.05.22.445269 (2021) doi:10.1101/2021.05.22.445269.

86.Tangye, S. G., Avery, D. T. & Hodgkin, P. D. A division-linked mechanism for the rapid generation of Ig-secreting cells from human memory B cells. *J. Immunol.* **170**, 261–269 (2003).

87.Jourdan, M. *et al.* Characterization of a transitional preplasmablast population in the process of human B cell to plasma cell differentiation. *J. Immunol.* **187**, 3931–3941 (2011).

88.Pedrioli, A. & Oxenius, A. Single B cell technologies for monoclonal antibody discovery. *Trends Immunol.* **42**, 1143–1158 (2021).

89.Trezise, S. & Nutt, S. L. The gene regulatory network controlling plasma cell function. *Immunol. Rev.* **303**, 23–34 (2021).

90.Gaudette, B. T. & Allman, D. Biochemical coordination of plasma cell genesis. *Immunol. Rev.* **303**, 52–61 (2021).

91.Shapiro-Shelef, M. *et al.* Blimp-1 is required for the formation of immunoglobulin secreting plasma cells and pre-plasma memory B cells. *Immunity* **19**, 607–620 (2003).

92.Kallies, A. *et al.* Initiation of plasma-cell differentiation is independent of the transcription factor Blimp-1. *Immunity* **26**, 555–566 (2007).

93.Tellier, J. *et al.* Blimp-1 controls plasma cell function through the regulation of immunoglobulin secretion and the unfolded protein response. *Nat. Immunol.* **17**, 323–330 (2016).

94.Jones, D. D. *et al.* mTOR has distinct functions in generating versus sustaining humoral immunity. *J. Clin. Invest.* **126**, 4250–4261 (2016).

95.Taubenheim, N. *et al.* High rate of antibody secretion is not integral to plasma cell differentiation as revealed by XBP-1 deficiency. *J. Immunol.* **189**, 3328–3338 (2012).

96.Yoshida, H., Matsui, T., Yamamoto, A., Okada, T. & Mori, K. XBP1 mRNA is induced by ATF6 and spliced by IRE1 in response to ER stress to produce a highly active transcription factor. *Cell*

107, 881–891 (2001).

97.Grandjean, J. M. D. *et al.* Pharmacologic IRE1/XBP1s activation confers targeted ER proteostasis reprogramming. *Nat. Chem. Biol.* **16**, 1052–1061 (2020).

98.Harnoss, J. M. *et al.* Disruption of IRE1α through its kinase domain attenuates multiple myeloma. *Proc. Natl. Acad. Sci. U. S. A.* **116**, 16420–16429 (2019).

99.Uhlén, M. *et al.* Proteomics. Tissue-based map of the human proteome. *Science* **347**, 1260419 (2015).

Chapter 4.

SUMMARY, DISCUSSION, AND FUTURE DIRECTION

4.1. SUMMARY AND DISCUSSION

In Chapter 2, we uncovered the heterogeneity of cell products on day13 (Fig 2.5.1). We found the cells of interest for plasma cell therapy were primarily CD138+ cells. In the CD138+ isolation *ex vivo* experiment, an intrinsic anti-apoptotic program is active in the CD138+ population after 13 days of culture (IL-6, IL-15, IFN-alpha) even without a BM environment. In the extra 21 days culture we learned the decay rate decreases overtime. We've also observed that the antibody secretion rate of CD138+ cells is increased overtime with hIL-6 culture. Both experiments implied the CD138+ PCs could be a heterogeneous population with different decay rates and antibody secretion rates. However, the interplay of secretion capability and the anti-apoptotic program remains unclear. Second, the contribution of decay rate and antibody secretion rate changing overtime is majority from single cell's further development or the beginning of the outstanding subpopulation take over culture (Fisher's fundamental theorem of natural selection) remains unknown. Further study of the heterogeneity within the CD138+ population is likely to provide fundamental information useful for generation of cell products enriched for longevity and protein production.

Addition of IL-6 to CD138+ PC cultures (day 13 to day 34) improves antibody secretion per cell. However, the decay rates eventually converge, implying that the decay rate program and antibody secretion program could be independent in this experimental setting. Combined single cell transcriptomic and epigenetic profiling studies using prolonged cultures, with and without IL-6, are likely to further improve our understanding of PC development and differentiation. Furthermore, we can utilize SEC-seq to uncover what's programs mediate antibody secretion in IL-6 cultured PCs.

In summary, our findings provide a comprehensive view of *ex vivo* engineered PCs and their in vivo engraftment and functional capacity and at the same time, open many interesting questions for future investigation.

4.2. FUTURE DIRECTION

4.2.1. *Methodology to reprogram ex vivo PCs*

In chapter 2 and chapter 3, we learned that a subset of CD138+ PCs over 10 days *ex vivo* culture is potentially the optimal subpopulation for PC therapy. CD138+ PCs, compared to CD138- cells, exhibit many key transcriptomic features of long-term PCs, prominently including homing and engraftment in the BM. However, our current *ex vivo* culture conditions retain about 50% non-CD138+ cell types. Further optimization of the *ex vivo* differentiation culture system is likely to be crucial for optimal PC therapies.

We've tested multiplex cytokines in phase I B cell activation (Figure 4.3.1) and phase II PB/PC differentiation (start from naive B cells). Preliminarily, we found 'IL-21 combo' condition can improve CD138hi cell number in phase I and that IL-10 limits CD138hi cell generation in Phase II culture. Future experiments testing the clusters of interest (Fig. 4.3.1) with single cell techniques may provide key information. Transcriptome, epigenetic regulation and BCR clonality could be three areas to discover.

Previously we've learned that CD138hi cells have 0-1% active caspase + and CD138lo cells have 2-8% active caspase + (Fig. 2.5.10f). This implies that these populations exhibit different decay rates. We could utilize single cell VDJ 5' gene expression or single cell labeling to track the single cell/clonality dynamics overtime for cells after day13. This could permit us to

track plasma cell dynamics in a single cell instead of a bulk cell level (Fig. 2.5.10b), and potentially find key regulators.

From chapter 1 and multiplex experiments, we learned IL-2 and IL-21 are critical cytokines for PC differentiation in *ex vivo* culture and IL-6 is critical in both *ex vivo* and *in vivo* settings; with signaling mediated via each of these cytokines using STAT3. Knockout the inhibitory signals, e.g., PTEN, SOCS1, SOCS3, JMJD1C, could possibly reprogram PCs and alter the survival or antibody secretion.

Lastly, editing to introduce therapeutic proteins in the conditions we have optimized and monitoring therapeutic protein levels *in vivo,* overtime, will be crucial to validate and best understand the methodologies required for generation of clinically relevant, efficient PC therapies.

4.2.2. *SEC-seq application*

Current data in chapter 3 leave many critical questions uninvestigated. Transcription factors (TFs) likely play a key role in turning on the secretion program, upregulation of translational programs in the secreting cells are likely critical, and post-translational modifications could sabotage or enhance antibody secretion. Additionally, it's important to know while PC is stressed from making/pumping tons of antibodies, what genes are maintaining cell survival.

Knocking out genes that we found relevant in secretors is the next step we want to utilize to expand on our current finding from SEC-seq, by targeting, for example, RBPs, or transporters (SLCx), TFs. This approach would allow us to define genes that are functionally important for antibody secretion and with more optimization, we can potentially expand this approach by combining SEC-seq technology with CRISPR screening.

Secreted immunoglobulins from *ex vivo* differentiated PCs are potentially able to target different antigens. Therefore, we could potentially use 10X BEAM (Barcode Enabled Antigen Mapping) to map to antigens with secretors' antibodies. With the donor's antibody-antigen profile, we can further use PBMC from the donor and *ex vivo* differentiation to PC, immunoglobulin (2-50 pg/cell/day) can be amplified exponentially and unlimited time from PCs, for use to generate immunoglobulin products; or potentially for use as cell therapy to treat immunoglobulin deficient patients. Using 10X single 5' Gene expression, we can analyze the secretory antibodies BCR sequence corresponding to the antigen. And we can further study the antibody repertoire against the antigens of interest

Additionally, we can study the extracellular cell matrix interaction with plasma cells at single cell level by coating different chemical modified ligands on nanovials. Using SEC-seq we could then determine how transcription profile of PCs are modulated by different environments.

Finally, as nanovials utilize a PEG hydrogel, this provides a potential for cell encapsulation for cell transplantation. Engineered allogeneic plasma cells are likely a target for host cell surveillance and rejection. With an optimal matrix coated nanovial and the advantage of plasma cell's quiescence, nanovial encapsulated plasma cells might be directly transplanted into the BM as an alternative strategy to avoid host T and NK cell surveillance.

4.3. FIGURES

4.3.1. *IL-21 is critical to prime B cell for differentiation in Multiplex cytokine/CpG in Phase I*

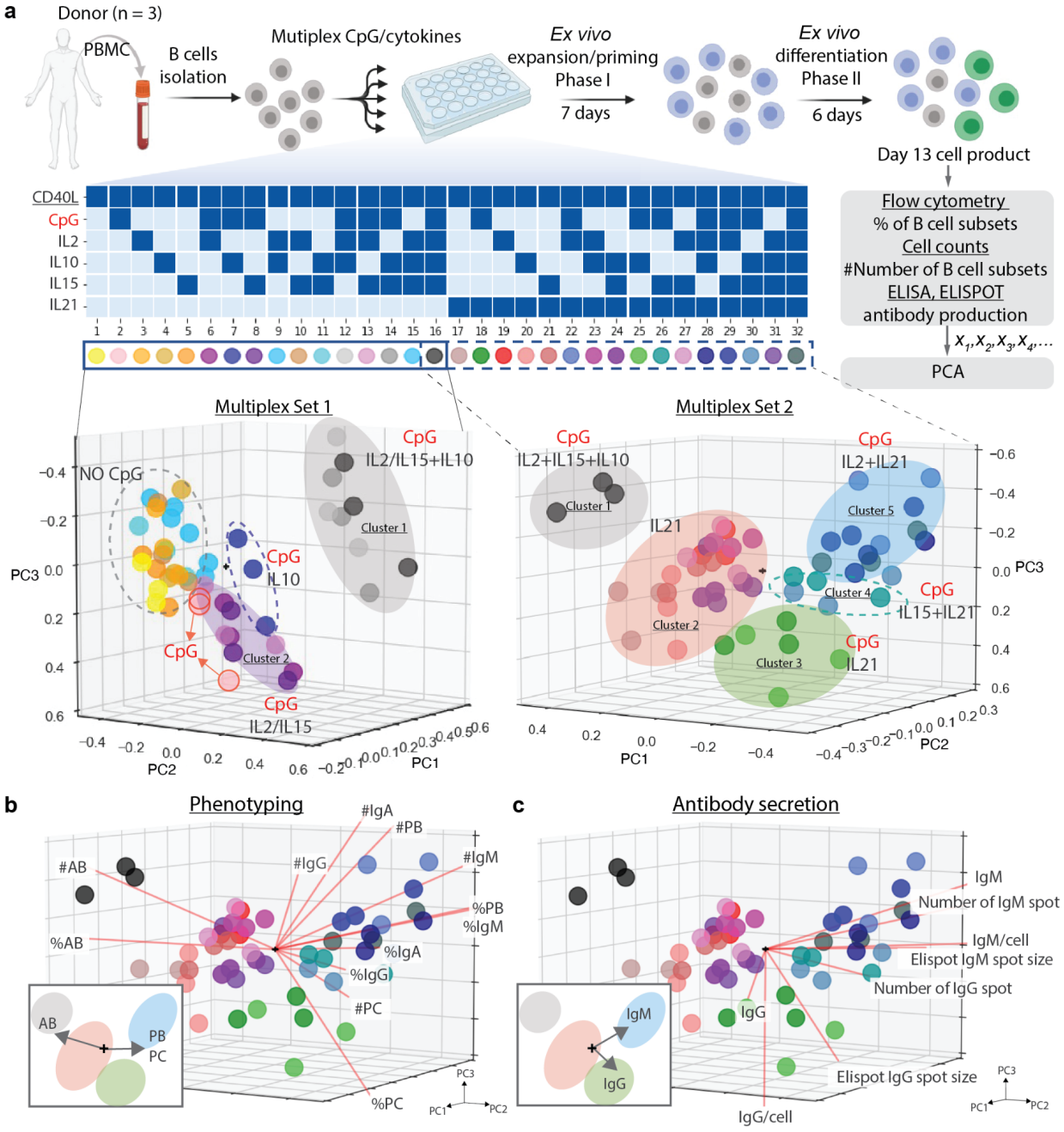

(a) Schematic cartoon of multiplex cytokines/CpG to differentiated PCs *ex vivo* (upper panel). PCA plot analyzed from measurement data matrix. Each dot corresponds to a different

condition, and each labeled cluster has common cytokines/CpG. (b-c) Loading plot overlays on the Multiplex set 2 three dimensional PCA score plot

4.3.2. *SOCS3 knockout increase the percentage of CD38+ and CD138+ cells subsets*

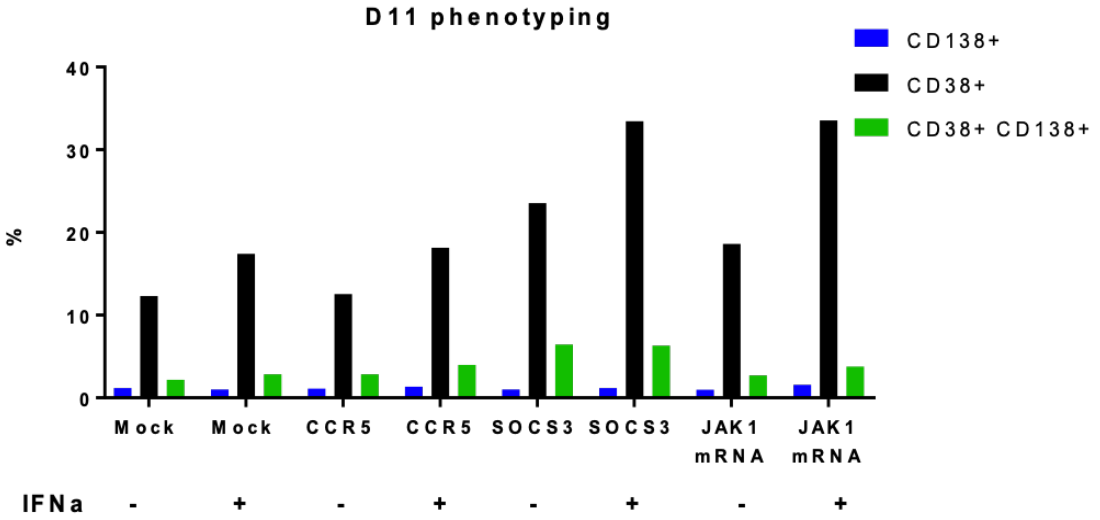

D11 post-editing (D13 from B cell isolation) phenotype quantification of *ex vivo* differentiated B cells.

VITA

Rene Cheng was born in Taiwan. After graduating from Taipei First Senior High School, she entered National Taiwan University. During 2012 to 2016, she worked in different labs in Academia Sinica and National Taiwan University, projects including biosensor, GPCR drug screening, and nanoparticles. In September 2017, she entered the graduate school at University of Washington, and expected to graduate in 2022. Now she’s a B cell engineer, plant enthusiast, pokemon collector and maybe beat saber expert.